UNIVERSITÀ DEGLI STUDI DI CATANIA

DOTTORATO DI RICERCA IN INGEGNERIA FISICA - XXIII CICLO

NADIA GAMBINO

INVESTIGATION OF LASER GENERATED PLASMAS FOR ASTROPHYSICAL APPLICATIONS

PHD THESIS

TUTOR:

PROF. FRANCO MUSUMECI

SUPERVISORS:

DR. SALVO TUDISCO

DR. DAVID MASCALI

PHD COORDINATOR:

PROF. GAETANO GIAQUINTA

ANNO ACCADEMICO 2009-2010

[...] *Tu sì la terra d'uomini di scienza,*
d'uomini d'onuri e curtisìa,
di l' Eternu fû ditti pi sintenza
terra nun cinn'è megghia di tia.
Ma la sfutruna 'ncuoddu ti carìu
quannnu vinni la droga e la lupara,
cû fidi lu priammu lu gran Diu
pi cancillari 'ssa svintura amara.
(da "Sicilia", di Francesco Giombarresi)

This study has been made in collaboration with:

Laboratori Nazionali del Sud

Istituto Nazionale di Fisica Nucleare

64, Via S.Sofia I-95123

Catania, Italy

Acknowledgements

I would like to thank my supervisor, Prof. Franco Musumeci for his scientific and human support during my Phd, helping me in the fulfillment of the stage at the DCU-Dublin City University.

I extend this gratitude to Dr. Salvo Tudisco, he was always helpful and willing to assist me in the numerous problems which I encountered during the course of this work.

I'm very grateful Dr. David Mascali, he has been a constant source of unbiased, critical advice and guidance, and most of all a good Friend able to transmit me the enthusiasm for science.

I thank my PhD coordinator, Prof. Gaetano Giaquinta. He has been am important source of human, intellectual and financial support during overall my PhD. I thank him also for the very interesting discussions about physics, philosophy and politic.

I thank also Dr. Santo Gammino, he was able to give me many precious advices necessary for a young scientist to mature in to a professional researcher.

I would like to thank Prof. John Costello for giving me the opportunity to spend six months in Dublin working in the DCU labs, and for helping me to realise with complete freedom my experiments therein. His humanity and

helpfulness together with the few pints on a Friday were much appreciated too, and made me feel like a part of the team. The members of that team were great too; Colm Fallon helping me not only with data acquisition but also to find a good place to stay carrying me around with his car; Paddy Hayden for being so patient, helpfulness in the lab and for reading my thesis; Padraig Hough, that transmitted me a lot of positivity and knowledge about colliding plasmas, especially during my firsts months in Dublin, Mossy Kelly even in the lab when I needed his help and Pat Yeates spending with me days and nights trying to set-up Langmuir Probes on colliding plasmas. I thank them together with the other guys of the team not mentioned here that made me feel at home in Ireland, make my short stay in Dublin funny. It was a very good time for me.

I moreover thank some people of the LNS-INFN of Catania: the Ion Sources group, in particular Rosalba Miracoli transmitting me her knowledge about Langmuir Probe theory, Luciano Allegra for his technical support and Giuseppe Castro helping me a lot near to the thesis deadline. I also thank Antonello Anzalone and his research team that helped on the set-up of my experiment. The members of the Biophysics group are also specially acknowledged; in particular Sara Grasso for turning off and on the Laser at DMFCI, and Lorenzo Neri, for his precious advices in using properly numerical codes. I also thank all the other people of these groups not mentioned here.

The support of mechanical, electrical and vacuum workshop of both DCU University and LNS-INFN is also sincere acknowledged.

I'd like to thank all the guys of the *Allegra Café Social Club*, working at the LNS-INFN of Catania. Thanks guys, for the really good lunch times,

full of stimulating discussions and of sincere friendly smiles.

I thank my friends: most of them were abroad during these years, but anyway close to me spiritually, especially one of them was constantly present with her virtual coffees.

Not less important, I'd like to express sincere gratitude to my family: my parents, Nunziatina and Giuseppe, my sister and brother, Patrizia and Rino, my grandmothers Grazia and Vita. All of them supported me during my PhD, giving me the force and precious advices to overcome all critical times.

I finally thank Salvo, I would never realize this work without him.

Contents

Introduction

Plasma is known as the fourth state of matter, and covers today an important role in several fields of scientific research, going from matter science to nuclear physics, to many industrial applications. Nuclear physics is one of the most promising field where plasmas can be employed. The even more increasing need to find alternative methods to produce energy, substituting carbon fuels, leaded to important development in Fusion research in the last decades, employing high density plasmas[1]. In order to obtain high density and high temperatures, plasmas must be *confined* to facilitate the ignition of fusion reactions. On this purpose controlled fusion research is today supported through two main topics involving plasmas: *MCF*-Magnetic Confinement Fusion, and *ICF*-Inertial Fusion Confinement respectively obtained by employing strong magnetic fields or high intensity lasers. Plasmas have a primary role also in modern astrophysics, since it composes the 99% of the matter in the universe and only a few percent is present on earth, (see eq. (1.2.2)). It comes out that many cosmological and astrophysical studies on

[1]The advantages of using nuclear fusion as alternative method of energy production are related to the no production of CO_2 and other greenhouse gases, and to the fact that the fusion fuel basic sources (D-Deuterium and T-Tritium, isotopes of Hydrogen) can be easily and inexpensively extracted from the ocean, so that the supply is virtually inexhaustible.

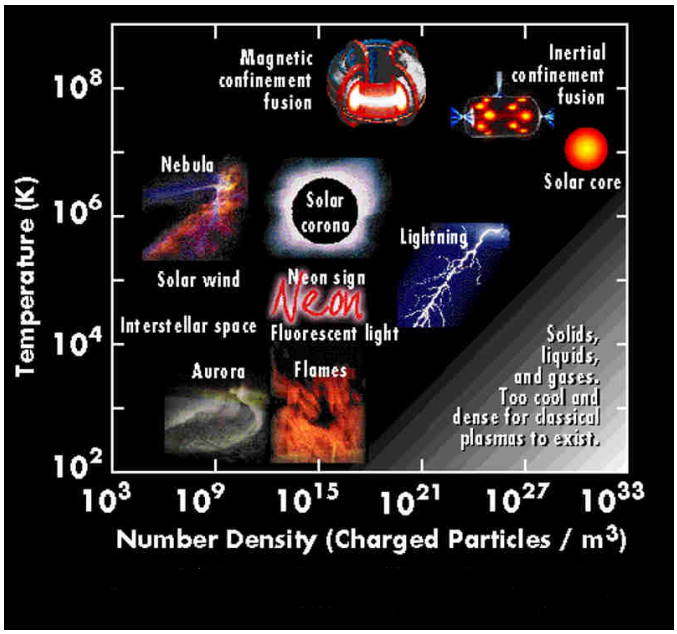

Figure 0.0.1: *Classification of Plasmas vs temperature and Density (*DOE Fusion Lab-NASA*).*

stars and galaxies are devoted to plasma investigations. Astrophysical phenomena such as plasma streams, comets, turbolences, jets, shock waves and instabilities are directly or indirectly related to fusion reactions. Therefore the investigation of the origin of stars and related phenomena dials closely with plasma physics [1]. This opened to a new field of physics interest from the late $1950's$ called *Nuclear Astrophysics*. It is a branch of astrophysics which helps the understanding of the Universe through the knowledge of the microcosm of the atomic nucleus. It is hence devoted to nuclear reaction rate measurements and theoretical estimations in order to understand the origin of the chemical elements and the energy generation in stars.

In figure 0.0.1 different type of plasmas are classified in relation to their

density and temperature. Fusion plasmas for energy purposes must have ion temperatures at least on the order of $10^8 K$ and charged particles density higher than $\rho = 10^{14} cm^{-3}$. Decreasing the temperature of one or two order of magnitude ($10^7 - 10^6 eV$) astrophysical plasmas are detected, principal constituents of Nebulas (for $\rho = 10^9 cm^{-3}$), of the Solar corona (for $\rho = 10^{15} cm^{-3}$) and of the Solar core ($\rho = 10^{30} cm^{-3}$).

It is clear now that Nuclear and Astrophysical research cannot be improved without a fully understanding of plasma physics. Although it is impossible to reproduce the extreme properties of stellar matter (keV temperature plasmas can be rather easily generated in laboratory, but with densities orders of lower magnitude than the stellar ones), by following a methodology largely employed in other fields of plasma physics, it is possible to rescale plasma parameters (e.g. temperature and density) in order to make similar to the real world our laboratory conditions. High energy lasers systems are in this sense not only employed to demonstrate fusion as an alternative method of energy, but also to investigate other interesting phenomena regarding astrophysics and nuclear physics, such as ion acceleration, shock wave and jets production and ES-Electron Screening. Plasma conditions for the verification of fusion events can be obtained without the several efforts needed for the operations of fusion reactors: the study of cross sections and the evaluation of ES can be included in this last framework.

ES is a key parameter for the proper understanding of several astrophysical processes, from stellar evolution to the most spectacular events like supernova explosions. Because of the extremely high densities of stellar plasmas and of their relatively low temperatures (few keVs), the screening has a weight in determining the fusion rates also in laboratory plasmas, especially

in a low energy domain. The target nuclei and the projectiles are usually in the form of neutral atoms or molecules and ions: in this case electron clouds surrounding the interacting nuclides act as a screening potential, hence the projectile effectively sees a reduced Coulomb barrier.

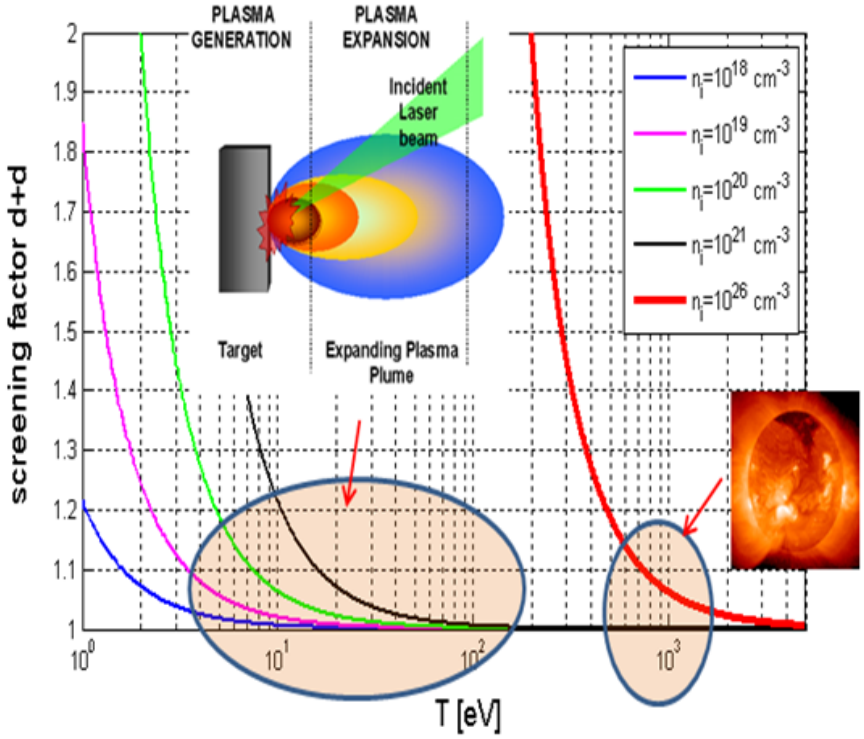

Figure 0.0.2: *Screening factor for D+D reaction as a function of electron temperature and density. On the right plane, highlighted the typical solar values. In the central region an highlighted the temperature and density obtained from the plasma induced by laser ablation [2].*

On this purpose, some calculations about the expected ES in plasmas at different densities and temperatures are reported in figure 0.0.2 [2]. At temperatures and densities that are typical of LPP-Laser Produced Plasmas,

with laser irradiances on the order of $10^{10} - 10^{12} W/cm^2$ and nanosecond pulse length, the classical Debye-Hückel screening factor becomes comparable with the one of the solar core. Although the density is very low if compared with stars and other laboratory plasmas, numerical simulations demonstrate that in this case ES may be appreciable. While ES has an explicit dependence on the ratio between the electron density and the electron temperature, the fusion reaction rate depends both on the plasma density and from the ion temperature. In the above laser irradiance domain, hydrodynamic simulations and experimental data reveal that in the early phase of the plasma expansion mean ion energy reach values of hundreds of $100 - 300 eV$, with densities of about $10^{20} cm^{-3}$. Ion temperatures are hence high enough to ensure a not negligible number of fusion events and at the same time, electron temperatures which are on the order of few eVs or tens of eVs are low enough to provide to a strong influence of ES. This discrepancy is mostly due to plasma acceleration mechanisms, partially driven by self-generated electric fields; the expansion dynamics produce an effect on the energy content of the two species (ions and electrons) that is different from the observation on magnetic confined plasmas (where the electrons reach temperatures orders of magnitude higher than the ion ones). This confers to LPP the unique peculiarity to be employed for fusion reaction rates measurements in a low energy domain that is still unexplored by nuclear physicists.

In the same regime also multiple interacting laser plasmas, i.e *Colliding Plasmas*, can be employed for the same purposes mentioned above. Plasma-Plasma collision generated from laser ablation have been employed also for other nuclear and astrophysical applications, such as ICF and supernova

remnants studies realized through the generation of collisionless shock waves. At low laser energy, two colliding plasmas generate, inside their interaction zone, a layer with highly collisional particles where the plasma stagnates for a time of about $400ns$, forming in this way a third plasma with peculiar characteristics: here the plasma collisionality can increase also of several order of magnitude. This effect, known as *stagnation*, can result useful to study the ES, since the stagnation layer is composed by cold electron populations with electron temperatures on the order of few eVs and electron density that are maintained higher in time if compared to the single expanding plasma densities.

At the $LNS-INFN$ of Catania we aim to measure the ES influence on fusion at the before mentioned temperatures and densities domains. On this purpose, in this thesis, a new experimental apparatus has been built up [3]. The apparatus was constructed in order to realize measurements with single expanding and colliding plasmas produced at low laser fluence ($10^3 J/cm^2$).

Most of the results herby reported concern the characterization, in terms of density, temperature and temporal dynamics, of a single and double expanding plasma plume. Single plasma expansion was investigated in vacuum and in a background gas: results are reported in chapter 2. The measurements on colliding plasmas were realized at the DCU-Dublin City University, in collaboration with Prof. J. Costello and are reported in chapter 3. We also investigated the collision of two LPP from thin foils of $2\mu m$ of thickness, which results are reported in chapter 4. The plume dynamics was nearby studied by a theoretical hydrodynamic model reported in chapter 5. Some preliminary numerical fusion reaction rate estimations are here reported, serving as proof-of-principle virtual experiment for possible future

measurements of fusion reactions and ES by employing our plasmas.

The experimental set-up realized at the LNS-INFN permitted us to observe, other than the classical hydrodynamic expansion of the plasma, some non linear processes driven by the formation of *Multy-layers* (since now denoted with ML). This mechanism leads to the plasma *multi-fragmentation* and complicates its temporal dynamics. Such effect has been never profoundly investigated in a low laser energy domain up to now.

By means of improvements to the simulation codes based on hydrodinamical models, we were moreover able to well reproduce the experimental observed plume expansion [4, 5, 6].

The plasma-plasma interaction, i.e the stagnation layer, was studied by time and spectral resolved imaging, and time resolved spectroscopy at the same laser fluence of that one used to produce the single expanding plumes. In case of thin foil colliding plasmas, we observed and characterized not only the interaction zone of the forward expanding plumes, but also a *backward plasmas* propagating on the rear side of the target, that at this laser fluence were never investigated in the past.

Data collected during the experimental campaign at LNS and DCU were obtained with Al targets, because they are versatile, cheap and a wide literature exists for data comparison. Measurements confirmed that at a low regime of laser intensity and with moderate fluences, plasmas exhibit proprieties which well fit with requirements of ES investigation. However for fusion reaction rate measurements, CD_2 targets must be employed, obviously because of their high content of deuterium. Since our hydrodynamic code reproduces quite well the behaviour of the plume except for the non linearity mentioned before, numerical simulations can be easly extended for

fusion reaction rates calculations by using CD_2 targets. Preliminary calculations based on the solution of hydrodynamics equations applied to the plasma expansion, predict that some hundreds of fusion events per single laser shot should be generated [7]. The suppression of plasma instabilities which generate the plasma fragmentation will be mandatory in future to avoid that any not handling mechanism affect the fusion rate.

Chapter 1

Fundamentals of Laser Produced Plasmas

In this chapter the main characteristics of a nanosecond laser generated plasma, including the several theoretical and experimental approaches used to characterize it are presented.

1.1 Overview

Laser Produced Plasmas (LPP) have a 40 years old research history. The first studies of effects of focused laser pulses on solid targets in vacuum were published in the 1963 [8] by several authors like Verber, Adelman, Lichtman, Ready, Giori, Honig and Woolston, employing millisecond lasers pulse length. One of the most employed field of lasers plasmas was initially focalized in deposition of thin films, employing LPP on a wide range of solids targets with several types of lasers (Ruby, Neodynium and Carbon Dioxide Lasers). For laser irradiance up to $10^5 W/cm^2$ the laser acts purely as a

heat source at the target surface. To generate a plasma the irradiance must be about $\geq 10^7 W/cm^2$ with a pulse duration of $0.5ms$ [8]. Nanosecond Lasers Pulses $(6-9ns)$ have been introduced with Q-switched Ruby lasers invention, in the $60's$. This immediately leads to raise the available laser irradiance to become on the order of $10^9 - 10^{13} W/cm^2$; ions emission having different charge states with energies up to some $keV's$ is then obtained [8]. The development of more powerful lasers and with very short pulse widths leads to even more complicated laser-matter interactions (nanosecond lasers can easily generate $10ps$ pulses with $10^{16} - 10^{18} W/cm^2$ of output power, introducing in this way the use of Picosecond Lasers pulses). In this case, the produced plasma is characterized by relativistic electron oscillations in the intense electromagnetic field of the laser light wave, and electronphonon interactions must be taken into account. Significant influence of the ponderomotive force is also expected [9]. Today picosecond lasers have been mostly substituted by Femtosecond Laser pulses, that reach power densities higher than $10^{18} W/cm^2$. In this regime the plasma is strongly influenced by non linear ponderomotive forces acting on the plasma; this mechanism is described by *weak* plasma oscillations. LPP by Femtosecond laser are mostly employed for ion acceleration [10].

It is clear now that the laser irradiance regime is of crucial importance for the definition of the plasma proprieties. Depending on the pulse width, on the laser energy and wavelength and on the atomic properties of the target, the laser beam energy will be absorbed in different ways by the evaporated particles, determining the creation of a plasma plume with different characteristics. In a low energy regime, the plasma evolution follows mostly the equations of state and the expansion can be considered adiabatic. In a high

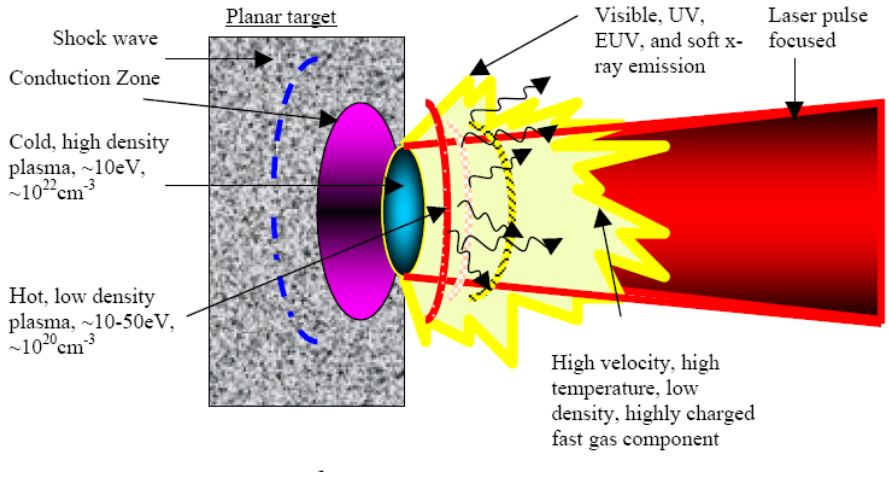

Figure 1.1.1: *General expansion dynamics scheme of a nanosecond laser generated plasmas; the plasma dynamics will be described in detail in section 1.8.1.*

energy regime ($> 1 \cdot 10^{13} W/cm^2$), the action of the ponderomotive forces lead to the creation of strong electric fields and plasma instabilities develop.

The nanosecond time scale, between $1 \cdot 10^{10} - 1 \cdot 10^{12} W/cm^2$ of laser irradiance, can be considered as a *transient regime*: the bulk plasma evolves adiabatically, but some plasma instabilities can have their influence at the early stage of the plasma formation, were fast particles can be generated (see figure 1.1.1): the rapid heating leads to a supersonic velocities expansion of the created plasma that expands adiabatically with large pressure and temperature gradients. However, plasma formation in nanosecond regime, as well as the gas-dynamics of the plume, are not yet satisfactorily explained and this is still relevant, especially for astrophysical implication.

1.2 Basic plasma parameters

Plasma physics found a big development in the XX century thanks to the work of many scientist as H. Alfvén, I. Langmuir and I. Bernstein [11, 12, 13]. A gas leads to the state of plasma by exciting the neutral molecules of the gas through an electromagnetic wave or trough an electric discharge. Free electrons acquires energy from the excitation source and collides with other neutrals molecules; when the number of free electrons equals the number of ions the gas is in the state of plasma so that the gas bulk is overall electrically neutral. The charge neutrality is expressed by the eq. 1.2.1:

$$n_e = \sum N_z \cdot \tag{1.2.1}$$

where n_e is the electron density, and N_z is the density of ions of charged state z. The presence of ionized molecules is then determined by the Saha equation 1.2.2:

$$\frac{N_z n_e}{N_{z-1}(p)} = 2\left(\frac{2\pi m_e k_B T_e}{h^2}\right)^{\frac{3}{2}} \frac{2g_z}{g_{z-1}} exp\left(-\frac{\chi_{z-1}(p)}{k_B T_e}\right) \tag{1.2.2}$$

where N_z and N_{z-1} are the ion stage populations, g_z and g_{z-1} are the statistical weights associated to the energetic levels within these ion stages, T_e is the electron temperature, $\chi_{z-1}(p)$ is the ionization potential of the ion of charge $z-1$ in the level p and is related to the energy difference between the two levels through $\Delta E = \frac{1}{2}mv^2 + \chi_{z-1}(p)$ (see section 1.11.2). Plasma charged particles interact with each other by *long range Coulomb forces* through collective phenomena [14]. The Coulomb force from any given charged particle causes an overall perturbation to nearby charges, thereby electrically polarizing the medium. The nearby charges move collectively to reduce or *shield* the electric field ϕ_t from any surrounding particle, which in

the absence of the shielding decreases as the inverse square of the distance (see figure 2.3.3). To restore the equilibrium, the resultant cloud of charge density around a particle has a determined scale length, the well know Debye Length λ_D, beyond which the electric field is collectively shielded out (to restore the quasi neutrality). λ_D is given by the formula:

$$\lambda_D = \left(\frac{\epsilon_0 k_B T_e}{n_e \cdot e^2} \right)^{0,5} \tag{1.2.3}$$

where T_e in eV is the electron temperature and n_e in m^{-3} is the electron density. λ_D is obtained by solving the Poisson equation for a charge particle

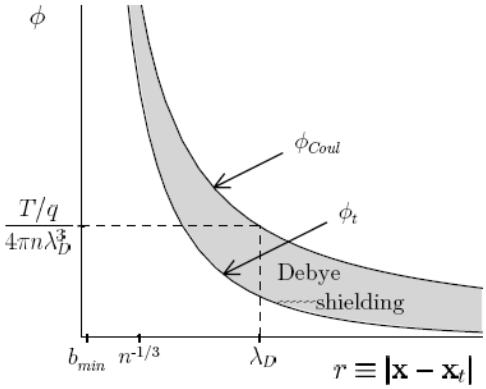

Figure 1.2.1: *Potential ϕ_t around a test particle of charge q_t in a plasma and Coulomb potential ϕ_C, both as a function of radial distance from the test particle; $b_{min} = q^2/(4\pi\epsilon_0 T)$ is the classical distance of closest approach where the approximation $e\phi/T \ll 1$ with T plasma temperature breaks down [15].*

q in a Maxwell-Boltzmann equilibrium thermodynamics system subject to an electrostatic field ϕ where the particles have an internal energy much larger then the electrostatic energy ($k_B T_e \gg e\Delta\phi$). The complete theory

can be find in [14]. A plasma is fully characterized by measuring its density and its temperature. In fig. 1.2.2 the different types of plasmas are classified in function of the electron density, the electron temperature and λ_D. The plasma state is assured when $\lambda_D \ll L$ where L is the plasma width. Such a condition can be used to distinguish between a true plasma and a highly energetic medium. Another important relation coming from a statistical treatment of the plasma is that $N_D \gg 1$, defined as the Debye sphere by the equation 1.2.4:

$$N_D = \left(\frac{4}{3}\pi\lambda_D^3\right) \tag{1.2.4}$$

1.3 Waves in plasmas

The wave propagation in plasmas is quite a complex argument, as it involves many aspects of the plasma physics with a tangled mathematical approach. Plasma waves are always associated with oscillations of charged particles, hence with time and space varying electric field, and the propagation properties of such fields are determined by the dielectric properties of the plasma, which in turns depend on the steady-state values of electric fields. The self-generated electrostatic plasma oscillations are crucial to determine the electromagnetic field propagation. These oscillations arise in a unmagnetized plasma because of the electric fields acting among the plasma particles. If a group of electrons is displaced from its original position, an electric field arises which tends to retain the electrons to their initial position. This mechanism generates oscillations which in a cold plasma approximation, i.e. $T_e = T_i$=0, do not propagate into the plasma [16].

The general wave equation for a plasma is obtained by solving the magneto-hydro-dynamics equations, the fully mathematical approach is re-

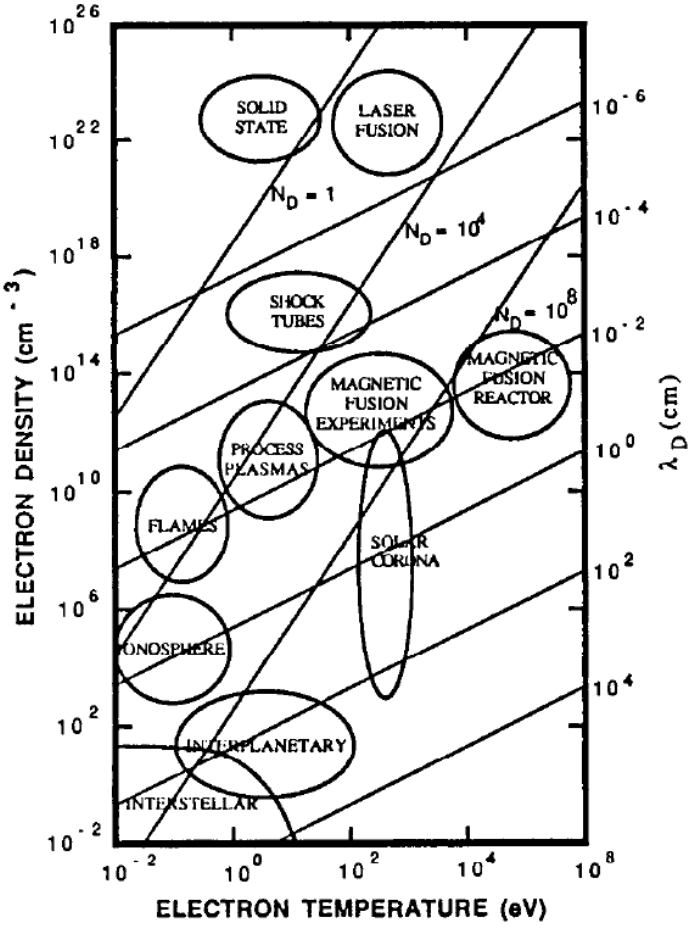

Figure 1.2.2: *Different types of plasmas vs electron density, the electron temperature and* λ_D.

ported in [14].

The wave equation for the electric field in a unmagnetized plasma consists of three homogeneous equations in the components of $\vec{E}$ and can be written as (1.3.1) [8]:

$$\vec{k} \times (\vec{k} \times \vec{E}) + \left(\frac{\omega}{c}\right) \vec{\epsilon}\vec{E} = 0 \tag{1.3.1}$$

where $\vec{\epsilon}$ is the dielectric tensor given by the equation (1.3.2):

$$\vec{\epsilon} = 1 + \frac{\vec{\sigma}}{i\omega\epsilon_0} \tag{1.3.2}$$

and σ corresponds to the conductivity, ω to the angular frequency of a electromagnetic wave and ϵ_0 to the permittivity in vacuum. A given solution for $\vec{E} \neq 0$, when the determinant of (1.3.1) is equal to zero is well know as the *dispersion equation.*

In a isotropic medium $\vec{\epsilon}$ becomes a scalar [8] and is know as the dielectric constant ϵ_T. For a given frequency ω, non dependent from $\vec{k}$, the determinant is a quadratic form of ϵ_T. This means that for each ω two different propagation modes exist (two different $\vec{k}$). To the different modes different transversal and longitudinal polarizations of the electric field $\vec{E}$ correspond. This considerations can be applied to every linear medium, and the propagation through a plasma is then obtained by finding from the state equations the expressions for σ and ϵ in function of ω. This leads to the different *dispersions relations.* Similar considerations can be done if we apply a magnetostatic field to the plasma $\vec{H}$ by adding a magnetostatic field term to the wave equation 1.3.1. In this case the plasma becomes an anisotropic medium for the electromagnetic waves propagation and the different modes must be related to the polarizations of the magnetic field. A complex set of different waves treated in detail in many books in literature [14], then

depend both on the orientation between the electric field and the magnetic field and on the orientation of the magnetic field respect to the vector $\vec{k}$.

Let us consider the case of $\vec{k} \times \vec{E} = 0$ for unmagnetized plasmas. In this case the so-called electrostatic waves are defined, classified in the well know *Langmuir waves* for the electrons [17, 12] and the *Acoustic waves* [11] for the ions. Langmuir waves are produced by the oscillations of the electrons, which behaviour is similar to that of an harmonic oscillator. The oscillation frequency is described by the the Bohm-Gross dispersion relation 1.3.3 [14] and leads to the definition of the natural frequency of electrons in a cold plasmas, called electron plasma frequency ω_p[1]:

$$\omega_p = \omega_{pi} = \left(\frac{e^2 n_e}{m_0 \epsilon_0} \right)^{\frac{1}{2}} \tag{1.3.3}$$

where n_0 is the effective mass of the electron.

Obviously, to maximize the energy transfer from an external electromagnetic wave to the plasma ω_p must be equal to the natural frequency of the external electromagnetic wave. In this case a resonance will occur (where $k \longrightarrow \infty$) and the wave is strongly absorbed by the plasma. This is also leads to the definition of the *cut-off* region (here k goes to zero) by the equation $\omega_{cut-off} = \omega_p$. Substituting to ω_p equation (1.3.3) we obtain the critical plasma density N_{cr} where the absorption of the electromagnetic wave occurs eq.1.3.4:

$$N_{cr} = 4\pi^2 \frac{m\epsilon}{e^2} f_p^2 \tag{1.3.4}$$

Considering as external electromagnetic field a light wave, i.e., a ND:Yag laser with $1064nm$ wavelength, and $6ns$ of pulse length, its frequency is $f_p =$

[1]The plasma frequency can be obtained also from MHD

$2.8195 \cdot 10^{14}$ Hz, hence the critical density is equal to $N_{cr} = 3.1096 \cdot 10^{14} m^{-3}$[2]. The dispersion relations becomes more complicated when hot plasmas are considered, leading as well to plasma instabilities. For example, when hot electrons are taken into account in the natural oscillations, a damping term must be included by means of a thermal velocity v_{th} term. The dispersion relation is then described by the Bohm-Gross relation:

$$\omega_{LM}^2 = \omega_p^2 + \frac{3}{2} k^2 v_{th}^2 \tag{1.3.5}$$

This means that wave propagation can occur in the plasma with energy exchange between the wave with phase velocity $v_{ph} \neq 0$ and particles in the plasma with velocity approximately equal to $v \simeq (v_{ph}\omega)/k$, interacting strongly with the wave. Particles having velocities slightly less of v_{ph} will be accelerated by the wave electric field to move with the wave phase velocity, while those particles with velocities slightly greater than v_{ph} will be decelerated by the wave electric field, losing energy to the wave. This is the well know *Landau Damping* effect that is a resonant phenomenon involving those particles moving with a thermal velocity near to the wave phase velocity [14]. The damping is usually explained by noting that for distribution decreasing with increasing velocity, there are more particles moving slightly slower than the wave than particles moving slightly faster. If the slower particles are accelerated by the waves, then the wave's energy will be reduced and the wave damping occurs. As the number of slower electrons is higher than the number of the faster electrons, summing over a large number of electrons, the wave damps results in a globally heating of the electrons [16][3].

[2] In magnetized plasmas transverse waves can propagate also for $n_e > n_{cr}$, this are called *overdense* plasmas, resulting from a more complex wave absorption way [14].

[3] In hot magnetized plasmas, the electrostatic waves are know under the name of *Bernstein Waves* [13], resulting undamped when propagating exactly perpendicular to $\vec{B}$ [14]

We conclude this section by introducing the **absorption coefficient** for a light wave propagating in a unmagnetized plasma, fundamental to understand the energy transfer from a laser to the plasma. For a transverse wave $\vec{k} \cdot \vec{\epsilon} = 0$, so that the $\epsilon_T = (c^2k^2)/\omega^2$, with phase velocity $v_{ph} = \omega/k$. The refractive index is the ratio of light velocity to the phase velocity and due to the dielectric losses, it can be expressed by a permittivity that is both complex and frequency dependent. Taking both aspects into consideration, a complex refraction index can be defined by the equation:

$$\mu^2 = \epsilon_T = \mu^2 + i\alpha \tag{1.3.6}$$

$$\mu = \frac{c}{\omega} Re(k) \tag{1.3.7}$$

$$\alpha = \frac{c}{\omega} Im(k) \tag{1.3.8}$$

where μ is the real refractive index and α is the absorption index. The exponential spatial attenuation of the wave in the plasma is described by the linear absorption index α_l. Considering a radiation wave of intensity I travelling into one direction, for example z, in a plasma, it's attenuation can be described by the law (1.3.9):

$$\frac{dI}{dz} = \alpha_l I \tag{1.3.9}$$

α_l is related to ϵ_T by the equation (1.3.10):

$$\alpha_l = \frac{\omega}{c} \frac{Im(\epsilon_T)}{\mu} \tag{1.3.10}$$

We will discuss again and more profoundly α_l in the next sections, when collisions will be taking into account.

1.4 Atomic Processes in plasmas

In a plasma atoms and ions undergo to transitions between their quantum states through radiative and collisional processes. Among these processes, the most important are spontaneous radiative transitions and collisional transitions induced by electron impact [18]. In LPP atomic processes depend strongly on the interaction between the laser photons and the plasma particles: excitations and de-excitation processes within the plasma particles transfer kinetic energy or emits radiation. The radiative transition probability and the collision cross-section are dependent from each other. The balance between the two processes determines, as we will see in section 1.5, the plasma thermal equilibrium. However, thermodynamic equilibrium in LPP is never reached (i.e the plasma is optically thin). Predictions about which of the processes (radiative or collisional) can prevail with respect to the other one can be done only with some initially assumptions related to different equilibrium plasma models that will be discussed in section 1.5.

1.4.1 Collisional processes

A complete classification of collisions is shown in 1.4.1 [16].

The multiple collision takes plasma when more then two particles are involved in the interaction, and are divided between Coulomb interactions (Spitzer collisions) and multiple collisions due to plasma collective phenomena [19].

We report here only the most fundamental aspects of Spitzer collisions that determine the energy exchange processes in LPP. The most important binary collisional processes will be also discussed.

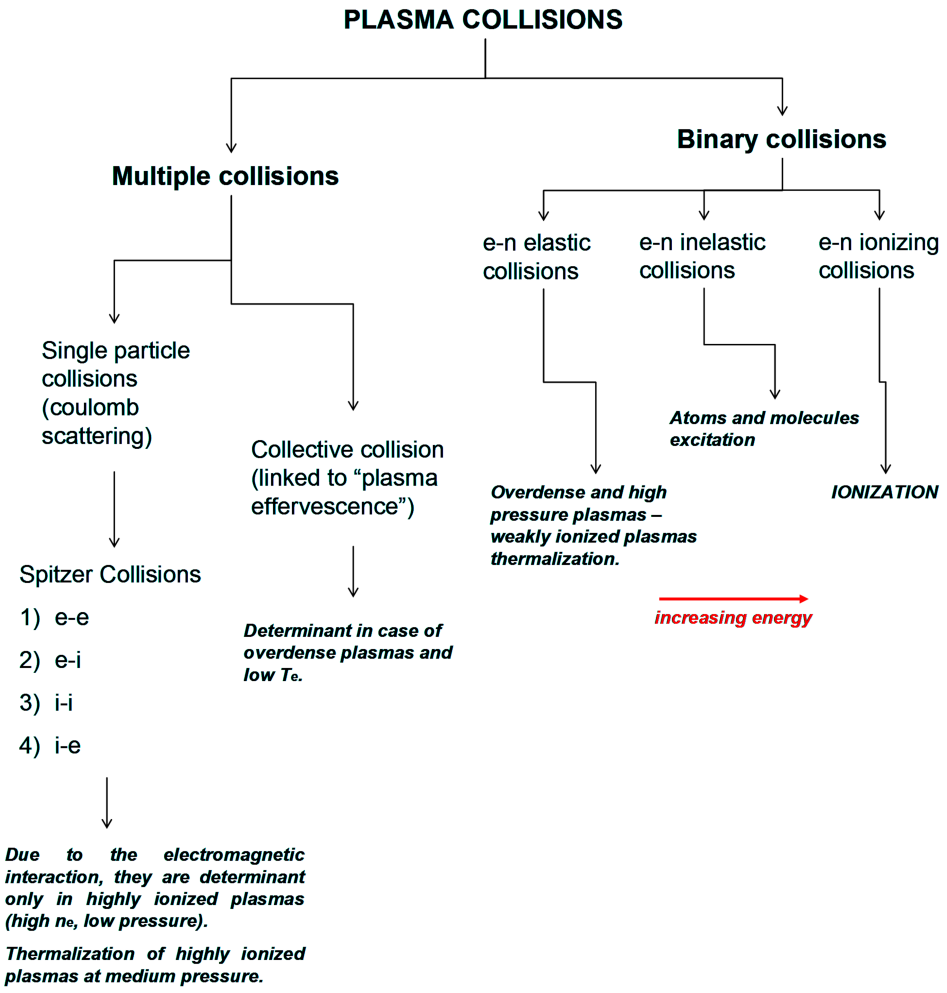

Figure 1.4.1: *A schematic overview of the main collision processes occurring in plasmas; the abbreviations e, n, i mean electrons, neutrals and ions respectively.*

- **Spitzer Collisions**

  A Spitzer collision is due to the coulomb interaction between the plasma particles. When an electron collides with an ion or another

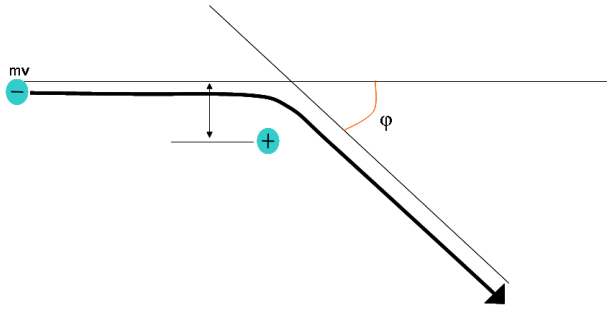

Figure 1.4.2: *Orbit of an electron making a Coulomb collision with an ion [14].*

electron, it is gradually deflected by the long range Coulomb field of the ion (see figure 1.4.2). In the absence of Coulomb forces, the electron would have a distance of closest approach of r_0 (the impact parameter), in the presence of the Coulomb attraction the electron will be deflected of an angle Φ_0 [14]. Because of the long range of the Coulomb force, small angle collisions with $\phi_0 \leq 90$ are much more frequent respect to the large angle collisions (that in case of binary collisions are represented by the Rutherford collision frequency $\nu_{ei} = n\sigma v = ne^4/(16\pi\epsilon_0^2 m^2 v^3)$); the cumulative effect of many small angle collisions turns out to be larger than the effect of a single large angle collision. The Rutherford's frequency, must be hence be corrected by a factor introduced by L. Spitzer, called Coulomb logarithm given by the formula:

$$\Lambda = \frac{\lambda_d}{r_0} = 12\pi n \lambda_D^3 \tag{1.4.1}$$

where n is the density and λ_D the Debye length. By following this approach not only ν_{90}^{ie} can be calculated for electron-ion collisions, but also the ion-ion, ion-electron and electro-electron collisions indicated

respectively with ν_{90}^{ii}, ν_{90}^{ie} and ν_{90}^{ee} can be determined, by the formulas:

$$\nu_{90}^{ee} = \frac{1}{\tau_{sp}} = 5 \cdot 10^{-6} n \frac{\ln\left(\frac{\Lambda_D}{b}\right)}{T_e^{\frac{3}{2}}} \tag{1.4.2}$$

$$\nu_{90}^{ei} = \frac{1}{\tau_{sp}} \sim 2 \cdot 10^{-6} z n \frac{\ln\left(\frac{\Lambda_D}{b}\right)}{T_e^{\frac{3}{2}}} \tag{1.4.3}$$

$$\nu_{90}^{ii} = \frac{1}{\tau_{sp}} \sim z^4 \left(\frac{m_e}{m_i}\right)^{\frac{1}{2}} \left(\frac{T_e}{T_i}\right)^{\frac{3}{2}} \nu_{90}^{ee} \tag{1.4.4}$$

where n_e is the electron density expressed in cm^{-3} and T_e the electron temperature expressed in eV. Once given the collision frequency we can easily determine the time between two successive events $\nu_{90}^{ee} \simeq \nu_{90}^{ei}$, and $\tau_{90}^{ee} \simeq \tau_{90}^{ei}$; if we consider ions colliding against electrons (i-e collisions), time between two successive events is given by the equation:

$$\tau_{90}^{ie} \simeq \left(\frac{m_i}{m_e}\right) \tau_{90}^{ei} \tag{1.4.5}$$

Spitzer collisions are fundamental to investigate the thermalization of the plasma via collisions and related energy transfer. The amount of energy transferred for particles of the same species (for example e-e or i-i) is about the half of the initial one, whereas it is equal to the $\frac{m_e}{m_i}$ fraction in case of $e-i$ or $i-e$ collisions. Then the following equations are established:

$$\tau_m^{ee} \sim \tau_{90}^{ee} \sim \tau_{90}^{ei} \tag{1.4.6}$$

$$\tau_m^{ii} \sim \tau_{90}^{ii} \sim \left(\frac{m_i}{m_e}\right)^{\frac{1}{2}} \tau_{90}^{ei} \tag{1.4.7}$$

$$\tau_m^{ei} \sim \tau_m^{ie} \sim \frac{m_i}{m_e} \tau_{90}^{ei} \tag{1.4.8}$$

Concluding the discussion on Spitzer collisions we remark that they play a primary rule in:

1. Plasma Thermalization Processes (section 1.5)
2. Charged Plasma particles detection by means of electrostatic probes (section 1.11.1)

- **Binary Collisions**

  Binary collisions in plasmas can be divided in two groups: electron-neutral collisions (elastic and inelastic) and ionizing collisions. In LPP electron-neutral collision are important for excitation and de-excitation processes of plasma particles and are related to emission of radiation. Ionization processes have a primary role in the early stage of the plasma formation, when the temperatures are very high and high charge states can be produced. Moreover, electron-ion collisions limit electron thermal conduction, which then affects the cooling rate of the plume during it's expansion. Binary collision are essentially due to two different type of atomic processes, called Bound-Bound transitions (B-B) and Free-Bound transitions (F-B). The firsts occur when an electron occupying a discrete energy level in an atom or ion, is promoted or demoted to another discrete energy level during a collision with another electron or by emission (or absorption) of a photon. Bound-Free processes occur when an ion receives enough energy to eject one of its bounded electrons into the continuum, thereby incrementing its ionization state by one, or an electron in the continuum loses energy and falls into a discrete energy level of an ion thereby reducing its ionization state by one [8, 20, 21]. This processes are hence classified in:

  1. **B-B**: Electron-impact excitation and de-excitation

2. **F-B**: Electron-impact ionisation and Recombination

- **Electron Impact Excitation and De-excitation**

  Electron Impact Excitation occurs when some or all of the kinetic energy of a free electron is transferred to a bound electron exciting it to a higher energy level. The energy gained by the bound electron is equal to the energy lost by the free electron. Conversely, Electron Impact De-excitation occurs when a free electron induces a downward transition of an excited bound electron in a nearby ion to a lower bound state, converting the excess energy into increased kinetic energy for the free electron. The balance equations for these processes is given by:

$$A + e(\epsilon_1) \Longleftrightarrow A^* + e(\epsilon_2) \tag{1.4.9}$$

  where $e(\epsilon_1)$ and $e(\epsilon_1)$ denote the free electron kinetic energies before and after the collision respectively. If equation 1.4.9 is read from the left-hand side to the right-hand side, it describes the process of electron-impact excitation, vice-versa it describes the process of electron-impact excitation for electron-impact de-excitation. Figure 1.4.3 shows schematically the atomic processes described above.

- **Electron-Impact Ionization and Recombination**

  Occurs when a high energy free electron collides with an atom (or ion): the incoming electron ionizes the atom and "kicks out" a bound electron from the atom in the continuum. The energy gained by the bound electron is equal to the energy lost by the free electron. This process is known as electron impact ionization and is described by equation:

$$A^z + e_1 \Longleftrightarrow A^{z+1} + e_1' + e_2 \tag{1.4.10}$$

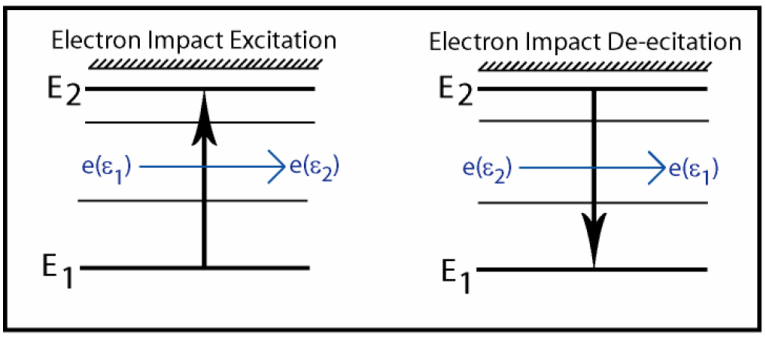

Figure 1.4.3: *Schematic diagram of the electron impact excitation (left) and electron impact de-excitation (right) atomic processes which occur in laser produced plasmas.*

e_1 and e_1' is the free electron before and after (lower energy) the collision and e_2 is the bound electron. This process is predominant in low density plasmas that are optically thin.

The inverse of this process is known as 3-body recombination and usually occurs in high density plasmas where the probability of two free electrons entering in the Debye sphere N_D (defined in equation 1.2.4) of an ion becomes relatively high. In a 3-body recombination process, one free electron is captured into an outer shell of an ion and the other free electron gains in kinetic energy the *surplus* of energy lost by the captured one. The balance equation for 3-body recombination is given by equation:

$$A^{z+1} + e_1(\epsilon_1) + e_2(\epsilon_2) \Longleftrightarrow A^z + e_1(\epsilon_1') \tag{1.4.11}$$

where A^{z+1} is an ion in charged state $z+1$, A^z is the ion of charge state z, $e_1(\epsilon_1)$ and $e_2(\epsilon_2)$ is the free electron before the interaction and $e_1(\epsilon_1')$ is a free electron with increased energy after the capture. The

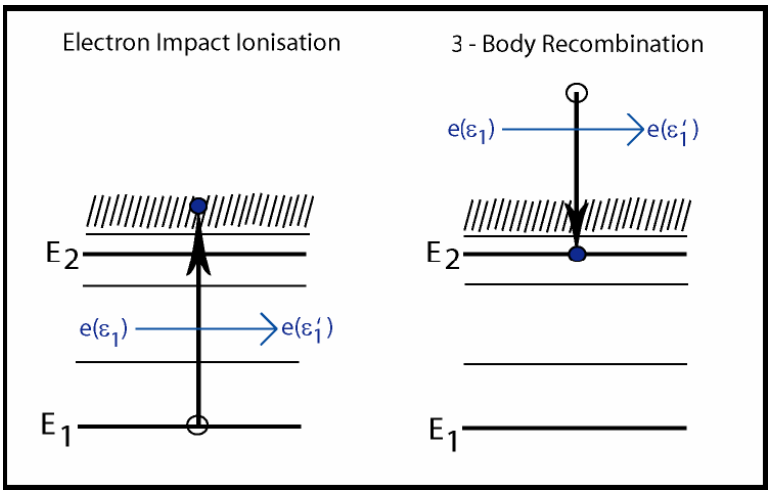

Figure 1.4.4: *Schematic diagram illustrating the electron impact ionisation (left) and 3-body recombination (right) atomic processes that occur in laser produced plasmas.*

processes is shown schematically in figure 1.4.4:

As we will see section 1.8.1, since the two electrons interact in the Debye sphere, 3-body recombinations have an important role during Double Layer formation in laser plasmas.

To conclude this section we report again the formula for α_l by taking into account an electron-ion collision terms in equation 1.3.10. Then the absorption coefficient can be defined by equation:

$$\alpha_l = \frac{\nu_{ei}}{\mu c} \frac{\omega_p^2}{(\nu_{ei}^2 + \omega)} \tag{1.4.12}$$

At frequencies well above ω_p, α_l can be approximated to the equation:

$$\alpha_l \approx \frac{\nu_{ei}}{\mu c} \frac{\omega_p^2}{\omega^2} \tag{1.4.13}$$

This means that **the linear absorption coefficient is directly propor-**

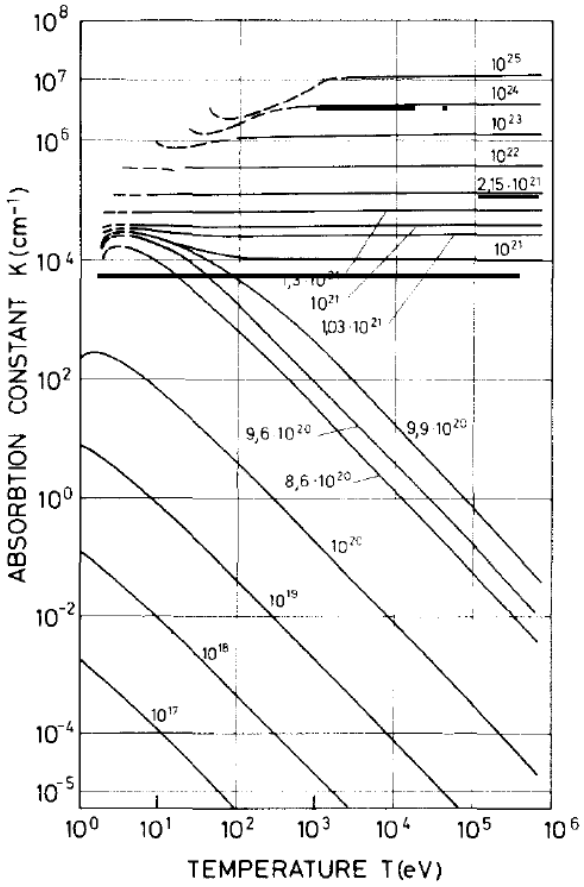

Figure 1.4.5: *Optical absorption constant K vs plasma temperature T for a ND:Yag laser with wavelength equal to* $1064\mu m$ *for different electron densities taking into account the Spitzer collisions [22]* .

tional to the collision frequency. In figure 1.4.5 the absorption coefficient for a ND:Yag laser operating at a wavelength of $1064\mu m$ vs temperature for different electron density taking into account the Spitzer Collisions. For a plasma temperature of $100eV$ and an electron density of $10^{19}m^{-3}$ the absorption coefficient is on the oder of 10^{-1}. After a collision processes, the

plasma particle can be in a excited state and can undergo in de-excitation processes through emission of light.

1.4.2 Radiative processes

In this section we will treat the main important radiation processes in plasmas, with particulary attention to those occuring in laser plasmas. Radiation processes are of fundamental importance in LPP, both for the emission of radiation (related to line emission spectra and hence to the evaluation of the plasma temperature and the plasma density) and also because the inverse process, i.e absorption of photons, includes the understanding of plasma ingnition through the interaction with the laser photons. As for collisional processes, atomic radiative processes are generated from, B-B and F-B transition including also collision between free electrons, called Free-Free transitions. The main process are classified in:

1. B-B: Spontaneous decay and Resonant photoabsorption
2. F-B: Photoionisation and Radiative recombination
3. F-F: Bremmstrahlung and Inverse Bremmstrahlung

- **Spontaneous Decay and Resonant Photoabsorption**

  Spontaneous Decay occurs when a photon is emitted stochastically in a completely spontaneous transition from an excited energy level to a lower discrete energy level. It can be described by the formula:

  $$A^* \longrightarrow A + \gamma \tag{1.4.14}$$

  where A^* denotes the atom/ion in an excited state and A represents the atom/ion in a lower energy state.

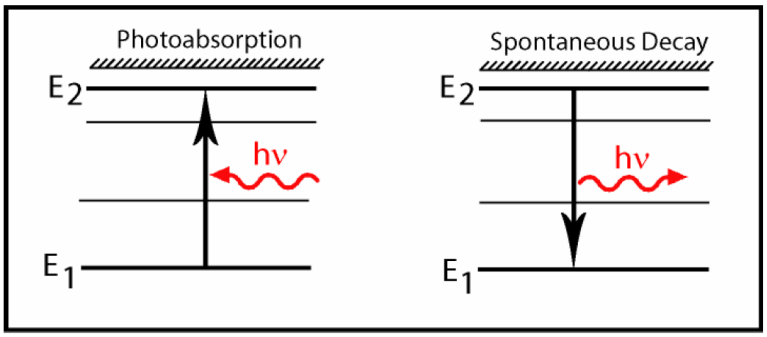

Figure 1.4.6: *Schematic illustration of the photoabsorption (left) and spontaneous decay (right) processes. E_1 and E_2 are lower and upper electron energy states of the atom/ion respectively.*

Conversely, photoabsorption occurs when a photon is absorbed by an electron in a low energy state that is consequently promoted to a state of higher energy. In this case the energy difference of the electron before and after its transition is equal to the photon absorbed energy. This process can be described by the formula:

$$A + \gamma \longrightarrow A^* \tag{1.4.15}$$

The two processes are reported in figure 1.4.6.

- **Radiative Recombination and Photoionisation**

  A free electron can be captured by an ion passing in its vicinity leading to recombination. During the process a photon is released with an energy equal to the energy difference of the electron before and after the transition. This process is called Radiative Recombination and can be described by equation:

$$A^{z+1} + e \Longleftrightarrow A^z + \gamma \tag{1.4.16}$$

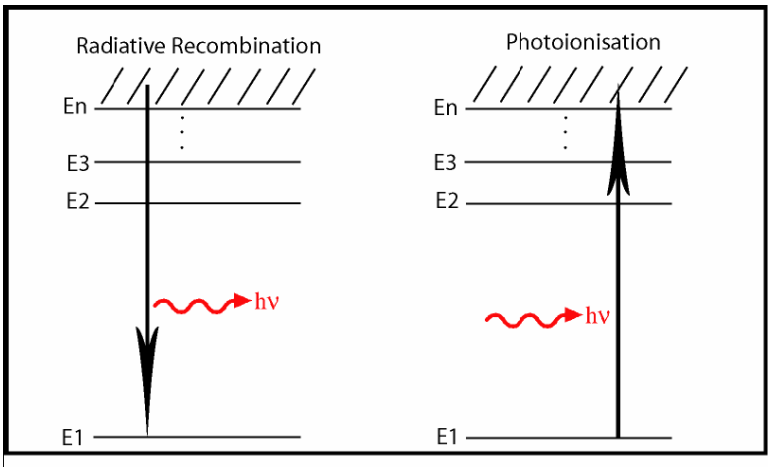

Figure 1.4.7: *Schematic illustration of the Radiative Recombination (left) and Photoionisation (right) processes.* $E_1, E_2, E_3 ... E_n$ *are the bound electronic states of the atom/ion.*

where A^{z+1} and A^z represents ions in charge state $z+1$ and z respectively [4].

Conversely, Photoionisation, i.e the well know photoelectric effect, occurs during the absorption of a photon by a bound electron resulting in the release of the electron into the continuum. It can be described the equation:

$$A^z + \gamma \Longleftrightarrow A^{z+1} + e \tag{1.4.17}$$

Both processes are shown in figure 1.4.7.

[4]There is also another type of recombination effect due to F-B transitions, called **Dielectric Recombination** occuring when an electron is captured from the continuum by an ion into an excited state. The excess energy of the electron is used to promote another bound electron into an excited state, thereby resulting in a doubly excited ion, that can either decay through autoionisation, returning to its initial state or through radiation emission.

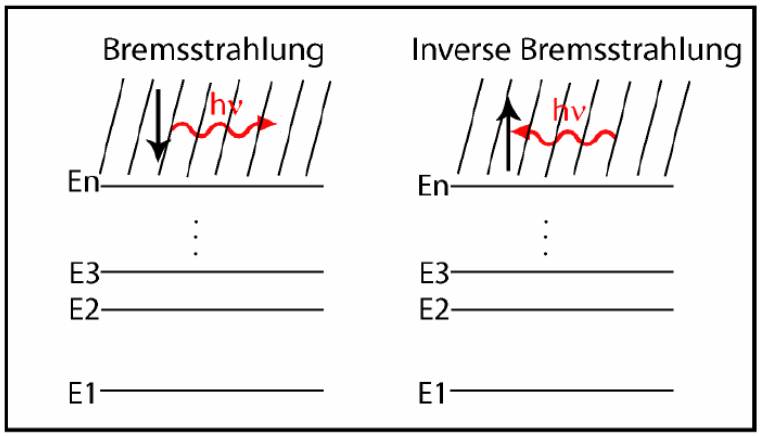

Figure 1.4.8: *Schematic diagram of the Bremsstrahlung (left) and Inverse Bremsstrahlung (right) atomic processes that occur in laser produced plasmas.*

- **F-F: Bremmstrahlung and Inverse Bremmstrahlung**

  Free-Free transitions are associated with the loss or gain of energy by an electron in the field of an ion. They are photon-electron interaction processes. F-F processes are extremely important in laser-produced plasmas, since IB-Inverse-Bremsstrahlung is the most important method of laser plasma heating in the energy regimes of this work. Bremsstrahlung emission is observed in radiation spectra of hot plasmas.

  Bremsstrahlung occurs when an electron passing through the Coulomb electric field of an ion, is accelerated and emits a photon [5]. The process

[5] Since the electrons interact with the ion Coulomb field, this process can be classified as a collisional process.

Process	**Excitation**	**De-Excitation**	**Type**
B$\Longleftrightarrow$B	Impact Excitation	Impact De-Excitation	Collisional
B$\Longleftrightarrow$B	Photoabsorption	Spontaneous Decay	Radiative
B$\Longleftrightarrow$F	Impact Ionisation	3-Body Recombination	Collisional
B$\Longleftrightarrow$F	Photoionisation	Radiative Recombination	Radiative
F$\Longleftrightarrow$F	—	Inverse Bremsstrahlung	Radiative
F$\Longleftrightarrow$F	Bremsstrahlung	—	Collisional
B$\Longleftrightarrow$F	Autoionisation	Dielectronic Recombination	Special

Figure 1.4.9: *Summary of the main atomic processes that occur in Laser Produced Plasmas.*

can be described by the relation:

$$A + e(\epsilon_1) \Longleftrightarrow A + e(\epsilon_2) + \gamma \tag{1.4.18}$$

Conversely, when a free electron is in the vicinity of a heavy ion and absorbs a photon, a strong increase of its electron kinetic energy occurs. This energy increase is equal to the absorbed energy. Due to the vicinity of the electron to the heavy ion, the ion can absorb exceeding energy and the momentum is conserved and lead to IB, described by the equation:

$$A + e(\epsilon_1) + \gamma) \Longleftrightarrow A + e(\epsilon_2) \tag{1.4.19}$$

Bremsstrahlung and IB are reported schematically in figure 1.4.8.

All atomic processes herby described, are summarized in figure 1.4.9. Taking them into account in LPP, the general expansion dynamics of a plasma plume shown in figure 1.1.1 becomes more clear: in a first stage the laser target interactions (discussed in detail in section 1.6 prevails on

surface heating mechanism that rises at the laser pulse edge, thus ionizing the vaporized plume of target material released during the laser ablation. Atomic species absorb laser photons via photo-ionization and free electrons generated at target surface, promote in IB absorption. A small fraction of electrons is instead immediately ejected from the target in the early stages of laser-matter interaction. It forms a fast negative layer that accelerates the expansion of the plasma through the self-generation of an electrostatic potential. This mechanism boosts the plume acceleration, in addition to the adiabatic expansion provided by the inner plasma collisions, that are dominant in a second stage, when Photo-ionization generates a large amounts of ionic species and free electrons, which undergo to collisions: part of the electronic component then reaches temperatures of tens or hundreds of electronvolts. The electronic component is immediately characterized by a significant decrease of its temperature because of the volume expansion, while the ions, characterized by a high collisionality, are firstly heated by the electrons (through e-i collisions), equalizing the whole plasma temperature (one-fluid state), but then transform part of the ordered translational energy in chaotic thermal energy (because of the high ion-ion collisionality), increasing their temperature. Therefore the net result is an electron population characterized by temperatures even one order of magnitude smaller than ions as mentioned in the introduction. The energy gained by electrons through IB can excite or even ionize neutral/ion species through impact collisions with other particles, this enhances ionization within the plume.

Photo-ionization dominates for irradiances below $4 \cdot 10^8 W/cm^2$, IB becomes dominant at laser irradiances up to $5 \cdot 10^8 W/cm^2$, i.e in the operating regime of this work [20].

1.5 Thermal equilibrium in plasmas

Particle collisions and radiation fields dynamics are of great importance in plasmas. The balance between them determines not only the plume characteristics in terms of ionization rate, plasma potential, electron velocity, temperature and plasma density, but also the conditions for thermal equilibrium. Thermal equilibrium in plasmas is discussed through several theoretical models.

The first assumption regards the velocity distribution: at the equilibrium it follows a Maxwellian-Boltzmann, thus a *plasma temperature* can be calculated. In order to apply a statistical approach the mean collisional free path must be much smaller then the maximum extension of the plasma; in addition, the time between subsequent collisions must be short compared to other heating mechanisms. Laser plasmas usually fulfill these conditions for electrons but not for ions, thus ion temperature calculations are usually not reliable and the obtained values are generally approximated. When radiation cannot escape from the plasma volume due to re-absorption effects (the so-called *opacity*) within its volume, the plasma is said to be **optically thick** and every atomic process occurring in the plasma is balanced by an equal and opposite process (for example the rate of collisional excitation equals the rate of collisional de-excitation). In this case the plasma is said to be in *CTE - complete thermal equilibrium*: it is an ideal case for low energy laser expanding plasmas.

The CTE can be assumed when [18]:

1. All particles obey to the Maxwell velocity distribution law;

2. The ion distribution is given by the Saha equation (1.2.2);

3. The radiation intensity distribution as a function of frequency and temperature is given by the Planck formula;

4. The population densities of bound levels within the atomic system are given by the Boltzmann formula:

$$\frac{N_{z-1}(p)}{N_{z-1}(q)} = \frac{g_{z-1}(p)}{g_{z-1}(q)} exp\left(-\frac{\chi_{z-1}(p)}{k_B T_e}\right) \tag{1.5.1}$$

   where $n(p)$, $n(q)$, $g(p)$ and $g(q)$ are respectively the populations and statistical weights of states labeled with p and q, and $\chi_{z-1}(p)$ is the energy difference between levels p and q;

5. The intensity distribution of the emitted radiation can be described by the black body radiation distribution function.

Since the laser plasma is a highly dynamical system, CTE cannot exist, as clearly evidenced by the emitted radiation and by the velocity distributions. For more practical reasons, equilibrium models have been developed to describe plasmas in different regimes with less demanding requirements respect to CTE. The three most common equilibrium models used to describe plasmas are listed below.

- **LTE - Local Thermal Equilibrium**

  The LTE model is very close to CTE and is applicable to high density and hot plasmas, such as solar interiors, and laser plasmas at the early stage of their expansion. LTE is assumed when the plasma density increases to very large values ($> 10^{15} cm^{-3}$) and the rate of collisions prevails on radiative processes. This minimizes the amount of energy losses and thus the system is locally approximated to a thermodynamic equilibrium system. A Maxwellian velocity distribution

is still valid within each ion stage. However radiation spectrum is no longer described by the blackbody laws. Due to the mass difference, the electrons have larger velocities than the ions, being more more collisional. They are therefore responsible for the bulk plasma collisional transitions, which rate is used to determine the electron temperature. The formal relationship for LTE validity is that [18]:

$$n_e \geq 1.6 \cdot 10^{12} T_e^{0.5} \chi(p,q)^3 \tag{1.5.2}$$

where n_e is the electron density expressed in cm^{-3}, T_e the electron temperature expressed in $^\circ K$ and $\chi(p,q)$ is the highest ionization energy of any atoms or ions expressed in eV. In our laser energy regime, condition 1.5.2 can be assumed to be valid in order to determine the plasma parameters through optical spectroscopy measurements. The formulas will be given in section 1.11.2. An important advantage of LTE respect to other equilibrium models is that the ionization balance can be computed without knowing any of the transition rates.

- **CE - Corona Equilibrium**

  For relative low density plasmas LTE cannot be applied, since the electron density decreases drastically. The solar corona for example, has a high temperature ($10^6 K$) but is usually at low density ($10^8 cm^{-3}$). CE can be applied if:

$$n_e \leq 10^{10} (k_B T_e) \chi^{-0.5} \tag{1.5.3}$$

  Plasmas satisfying condition 1.5.3 are called **optically thin**. In this case the radiation emitted within the plasma volume is not significantly reabsorbed and passes through its edges. Photon absorption and radiative de-excitation rates no longer equilibrate. The rate of collisional

excitation is assumed to be very low if compared to the spontaneous decay rate. Electrons in excited states decay to the ground state before the succesive excitation event. As a consequence, most ions are in their ground state and collisional excitations balance radiative decays, from the upper to all lower energy levels. "Dissipating" processes such as radiative recombination are followed by photon emission causing the plasma's cool down [23].

- **CRE - Collisional Radiative Equilibrium**

  CRE describes a middle range of density values between LTE and CE: it tends to the CE at low density and to LTE at higher plasma density. It can result useful to describe the plume propagation at later time expansion. Both collisional (only involving electrons) and radiative processes are taken into account, neglecting autoionization and dielectric recombination processes. The velocity distribution is still supposed to be Maxwellian: the electron-electron relaxation time is smaller than electron heating time. At high electron density the electron relaxation time is the smallest characteristic one. Ion populations of charge $z+1$ must not change dramatically when the quasi-steady-state population of ions of charge z has been established. Moreover in CRE the plasma is supposed optically thin. In LPP, CRE can result useful to evaluate the average ionic charge state z in function of the electron temperature T_e, described by the formula [23]:

$$z = \frac{2}{3}[AT_e]^{1/3} \tag{1.5.4}$$

  where A is the atomic number of the element under consideration. For an typical nanosecond laser plasma, produced from an Al tar-

get, with $T_e = 20eV$, $z = 5$. This equation is obtained by the CRE model mathematical formalism describing the *steadystate ionization balance* between successive ion stages [23], neglecting three body recombination[6]. Equation 1.5.4 can be used to calculate the ratio of each individual charge state population (n_z) to the total population n_T of all charge stages using the simple relationship: $n_z/n_T = n_z/\sum_{i=1}^{Z} n_i$.

Figure 1.5.1 illustrates and summarizes the range of validity of each model vs n_e and T_e. For a Nd:YAG laser plasma with electron density on the order of $1 \cdot 10^{18} cm^{-3} < n_e < 5 \cdot 10^{19} cm^{-3}$, with low charge states, on the order of $1 < z < 5$ the validity of the model is listed as follow:

1. LTE model applies for electron temperatures on the order of $10 < T_e < 100$, i.e in the early stage of the plume expansion;

2. CR model applies only for higher temperatures, up to $T_e = 30eV$;

3. CRE model applies only for very low temperatures, hence when the plasma cools down, i.e at later expansion stages, for density values between the validity range of LTE and CR.

[6] This hypothesis is valid for $Te \geq 30eV$

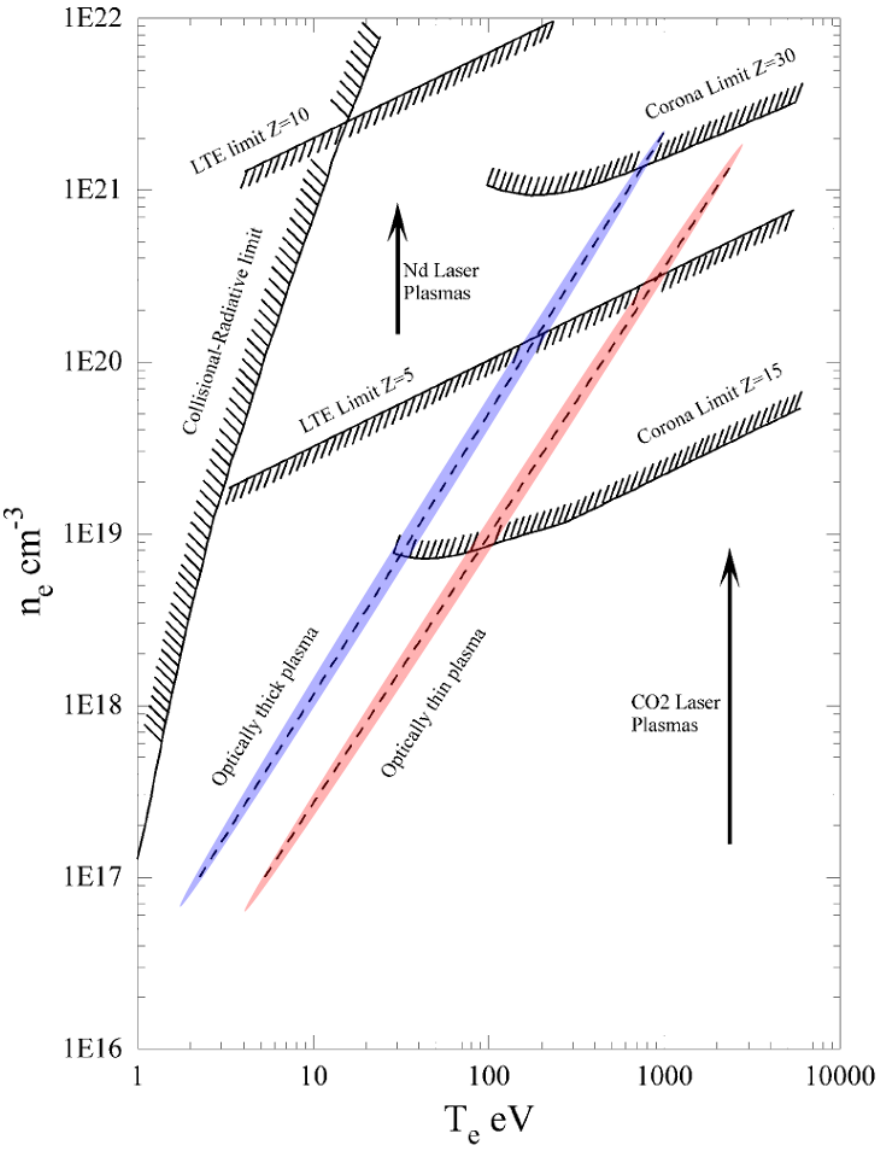

Figure 1.5.1: *Electron density and Electron temperature ranges for applicability of LTE, CE, and CR models [23].*

1.6 Laser-Target interaction

Laser target interaction causes the evaporation of the target atoms; the evaporation threshold depends on the target thermo-physical (bound energies of the target atoms) and optical properties. The number of free electron collisions in the material lattice is large and extends over a region of several λ_{mfp}, mean free path lengths. This causes the formation of a highly localized temperature gradient in the material. The intensity of the incoming radiation is drastically attenuated according to the Beers law (see equation 1.3.9). The electromagnetic radiation of intensity I_0 falls to $(1/e)I_0$ over a depth α_l^{-1}. The target temperature $T(\vec{z},t)$ increases at any depth during the laser pulse duration and its evolution is described by the *heat flow* equation [24]:

$$C_v(T)\frac{\partial T(z,t)}{\partial z} = \frac{\partial}{\partial z}\left[K(T)\frac{\partial T(z,t)}{\partial z}\right] + 1(1-R)I_s(z,t)\alpha e^{-\alpha z} \qquad (1.6.1)$$

where $\vec{z}$ is a vector perpendicular to the target surface, C_v is the specific heat capacity, $K(T)$ is the thermal heat conductivity of the material and R is the reflectivity. From equation 1.6.1, the surface temperature $T_s(eV)$ after irradiation by a laser pulse of ns duration, can be described by equation [25]:

$$T_s = \left(\frac{2I(1-R)\tau}{\pi K C_v \rho}\right)^{0.5} + T_0 e^{-\alpha z} \qquad (1.6.2)$$

In the above equation, I is the laser power density and and T_0 is the material temperature before the laser pulse.

Equation (1.6.2) assumes that the thermo-physical properties of the material and the laser beam intensity remains constant during the pulse duration. This is of course a simplification, since the interaction of the laser pulse with the pre-plume is highly complex involving many competing processes, and experimental measurements confirms that T_s is not constant

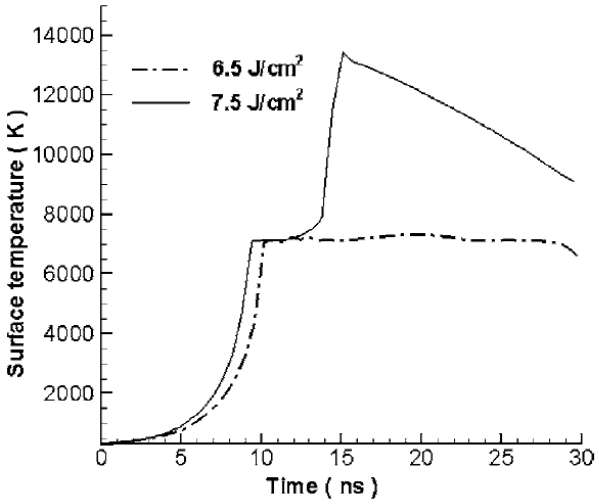

Figure 1.6.1: *Al target surface temperature vs laser pulse duration* $30ns$ *at two different laser fluences. Between the two fluences the phase explosion of the Al target occurs, calculated at* $7J/cm^2$ *[26].*

during the laser pulse duration. On this purpose in figure the target surface temperature is calculated during a pulse duration of $30ns$ for an Al target, for two different laser fluences namely $6.5J/cm^2$ and $7.5J/cm^2$ [26]. As we can observe from the figure, not only T_s is not constant during the laser pulse, but also between the two different fluences, the T_s vd *time* trends are consistently different. This occurs because between the two fluences **the evaporation (or ablation) threshold for the Al atoms is located**: by using a heat transfer model, it was calculated to be $7J/cm^2$ [26]. Let us now consider the crater depth evaluation; during the rising edge of the laser pulse, radiation is absorbed by electrons in the so called skin depth layer, raising them to higher energy states in the conduction band. These electrons then pass this energy on to the lattice during collisions, which quickly heat

and melt the surface. This results in a decreased reflectivity of the surface, thereby increasing the proportion of the laser-light that is absorbed by the target. The skin depth hence represents the length in which the laser EM field can penetrate into the solid target. It is defined by equation:

$$\delta = (\pi \nu \sigma \mu_0)^{-0.5} \tag{1.6.3}$$

where μ_0 is the permeability of free space, σ is the electrical conductivity and ν is the frequency of laser radiation. For aluminum target with $\sigma = 3.5410^7 \Omega m^{-1}$ irradiated by a Nd:YAG laser with wavelength of $1.064 \mu m$ $(2.82 \cdot 10^{14} Hz)$, $\delta \simeq 5nm$.

For nanosecond time-scale pulses a significant amount of heat is conducted from the skin depth layer into the bulk of the material, to a depth known as L_{th}, called *diffusion length* or heat penetration depth [24]:

$$L_{th} = \frac{2K\tau^{\frac{1}{2}}}{\rho C_v} = (2D_{th}\tau)^{\frac{1}{2}} \tag{1.6.4}$$

where τ is the duration, ρ the density, of the laser pulse and D_{th} is the material's thermal diffusivity. Under such conditions the energy of the laser pulse is stored inside a hole that can be approximated to a cone having the base diameter equal to the ablation spot size, and height comparable to the diffusion length. Hence L_{th} fixes the depth of the crater produced by the laser pulse interacting with the target. By adding to the diffusion length the skin depth we obtain the **total absorption depth** $Z = L_{th} + \delta$. In the nanosecond pulse regime, generally L_{th} is on the order of some μm, hence the relation $L_{th} \gg \delta$ is valid.

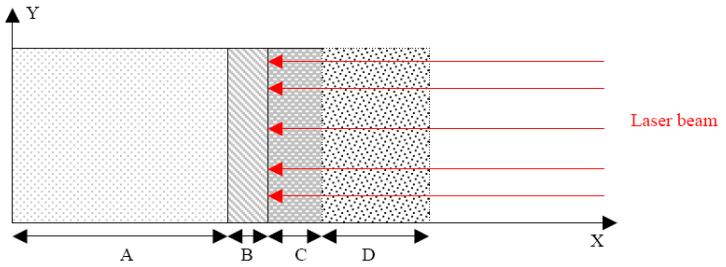

Figure 1.7.1: *Schematic diagram showing the 4 different phases in plasma expansion.*

1.7 Laser-Plasma interaction

During the vaporization stage, electrons are stripped from atoms by direct and multi-photon ionization. Free electrons absorb laser radiation and further undergo to collisions and ionization processes as describes in detail in 1.4; this leads finally to an overall increase of the ion density that allows to define the vaporized material as a plasma.

Taking into account the energy absorption mechanisms discussed in 1.4, the absorption coefficient can be re-written as:

$$\alpha = 3.69 \cdot 10^{8} \left(\frac{Z^3 n_i^2}{T^{0.5} \nu^3} \right) \left[1 - exp\left(\frac{-h\nu}{kT} \right) \right] \tag{1.7.1}$$

where Z, n_i and T are the average charge, the ion density, and the temperature of the plasma respectively.

The laser radiation is highly absorbed if the value of the product αL, where α is the absorption coefficient and L is the plume dimension in the plane perpendicular to the target surface, is large. However since α is proportional to the plasma density, the strongest absorption occurs near the target surface and the subsequent heating of the evaporated material is strongly

related to its value. It is important to emphasize that the optimum conditions for energy transfer from a electromagnetic wave to the plasma particles is that ω_p is equal to the natural frequency of the electromagnetic wave (see section 1.3). From a very dense plasma located near the target surface, the plasma expands very rapidly outwards causing the ion and electron density drop, thus making the plasma to be transparent to laser radiation. On the other hand, evaporation is still taking place and evaporated material is being added to the plasma so that there is always a thin layer of dense plasma between the bulk of the target and the plasma front edge that is absorbing laser light. The laser-target-plasma interaction region can then be divided into four sub-regions shown in figure 1.7.1 [21]:

Region A corresponds to the unaffected bulk target, region B shows the evaporated target material, region C is composed of the dense plasma absorbing laser radiation and region D corresponds to the expanding plasma which is transparent to the laser radiation. During the laser pulse a dynamics equilibrium exists between the plasma absorption coefficient and the fast transfer of energy from thermal to the kinetic content, so that a self-regulating regime is created at the target surface (region C). As the thermalization time is much smaller than the plasma expansion time, and since the plasma only occupies a small volume, radiation losses are negligible and it is legitimate to assume an isothermal and uniform regime. The isothermal regime can be described by the Sing and Narayan Model [24]. This means that a dynamics equilibrium exists between the plasma absorption coefficient and the rapid transfer of thermal energy to kinetic energy.

1.8 Plasma expansion

To describe the plasma dynamics after the end of the laser pulse, different models have been developed. Theoretically speaking, the kinetic theory is one of the best approach since it is based on the solution of the Vlasov equation. However, fluid dynamics equations have the advantage to consider only the three spatial coordinates instead of the six phase-space dimensions required by the kinetic equations. In addition, the measured plasma parameters, like density and temperature, can be compared directly with the fluid dynamics variables. Exhausting model are not available in the laser intensity regime of this work, but some approaches give predictions in reasonable agreement with the experimental data.

Plasma expansion can be better understood if we divide it in different sub-stages after the end of the laser pulse: in the first $50 - 90nsec$ of the plume expansion, quick electrons are the first vaporized particles that escape from the plume; they are then followed by accelerated ions of different charge states. In this early expansion stage, several DL-Double Layers [22] can be formed and strong electrostatic fields creating plasma instabilities can break the plasma quasi neutrality (see section 1.8.1). Then the bulk plasma expansion follows, obeying to an adiabatic expansion mechanism. Going further with time the density drops, leading to a collisionless plume that expands with constant temperature (free expansion is treated by R. Kelly et al. in [27]).

The entire ablation processes followed by the plasma expansion is summarized in figure 1.8.1.

During the Laser-Plasma interaction and on later expansion stages, there are some important effects occuring at the target surface and at longer dis-

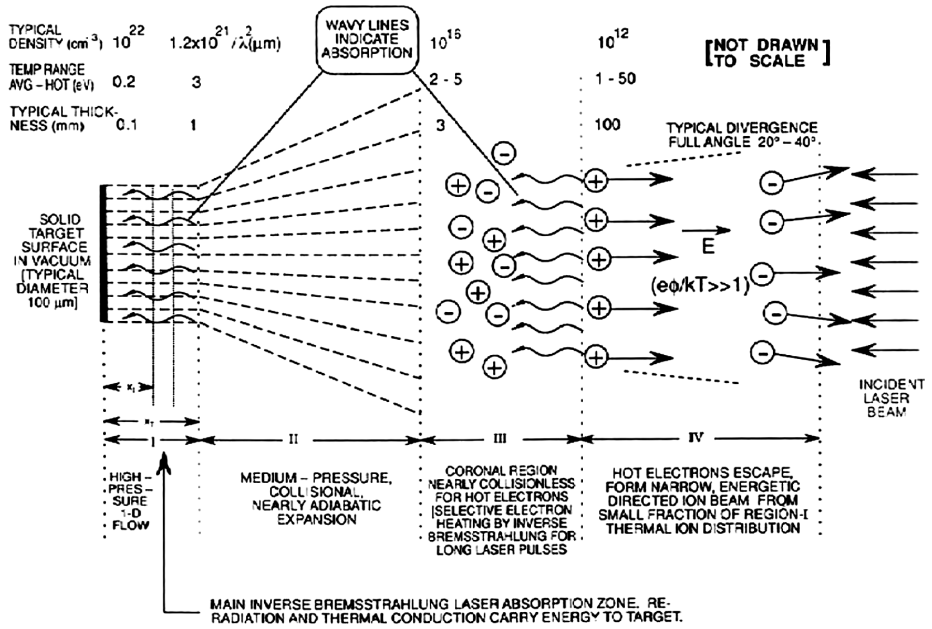

Figure 1.8.1: *General expansion dynamics scheme of a laser generated plasmas, for spot sizes on the order of* $100\mu m$ *and laser energies on the order of* $5 - 10J/cm^2$ *(from* Laser Ionization Mass Analysis, C. R. Phipps, R. W. Dreyfus, 1993 J. Wiley & Sons*).*

tances from it. They need to be discussed, before to introduce in detail the plasma expansion dynamics and helps to understand the dynamic reported in figure 1.8.1: they are the **KL-Knudsen Layer** formation and the **Shifted Maxwellian-Coulomb velocity distribution**.

The formation of KL was formulated and studied by R. Kelly in numerous papers [27]. In a high collisional regime recondensation at the target surface can occur and the strong non-equilibrium condition leads to an altered velocity distribution function which is no longer Maxwellian, that is called *full range maxwellian*, this occurs behind a KL. The full range maxwellian can be described by the formula:

$$f_K^{\pm}(\nu_2, E_1) = \left[\frac{n_k E_I^{j/(2-1)}}{(2\pi T_K/m)^{j/2}} \frac{1}{\Gamma(j/2)(kT_K)^{0.5}} \right] exp \left[-\frac{2E_I + m(\nu_z - u_K)^2}{2kT_K} \right] \tag{1.8.1}$$

where v_z is the velocity component normal to the target surface, E_1 denotes the total internal energy, n_K the number density of the KL, T_K is the Knudsen temperature, m is the particle mass, Γ is the gamma function, j the degrees of freedom and u_K is the center of mass velocity. In the region where collision occurs, i.e in the KL, the gas kinetic velocity v_z follows a Maxwell distribution. Due to the effect of collisions, plasma particles velocity distribution ahead a KL, is consequently described by the so-called *Shifted Maxwellian distribution*, composed by a two-velocity term distribution: the first one is the gas kinetic velocity v_z and the second determines the center of mass movement, giving to the plume the characteristic adiabatic expansion (section 1.8.2) and determining the forward peaked distribution. It is called the flow velocity and is indicated generally with v_γ. The flow velocity increases only within the KL, starting from the target surface until it assumes a constant value just after the layer, as the free flight in vacuum

begins (section 1.8.3). In order to consider the Coulomb effects inside the plasma, a better fit for the plasma particles velocity distribution must be applied: this is the so-called *Shifted Maxwellian-Coulomb distribution* and was instroduced by Torrisi et al. to better fit ion-energy distributions obtained with time-of-flight measurements on metal LPP. This distribution is described by the formula [28]:

$$F(v_z, v_\gamma) = A\frac{m}{2\pi k_B T}^{3/2} v_z^3 exp\left[\frac{m}{2k_B T} \times (v_z + v_\gamma + v_c)^2\right] \tag{1.8.2}$$

where A is a constant of normalization to the experimental data, T the plasma temperature, and v_c the Coulomb shift term defined by the relation:

$$v_c = \sqrt{\frac{2zeV_p}{m_i}} \tag{1.8.3}$$

where V_p is the plasma potential value, z the mean charge state, and m_i the ion mass. The plasma potential V_p is defined as the electric field established between ions and electrons separated by λ_D, this creates *space charge* separation. V_p gives an idea of how strong is the interaction between ions and electrons, due to the plasma ambipolar diffusion. Large V_p mean fluxes of fast escaping electrons, which therefore leave ahead conspicuous amounts of positive ions. V_p arises in order to equalize the positive and negative fluxes. However, in some cases, space charge separation can extend also to several λ_Ds, in this case DLs are formed in the plasma, as we will see in the next section.

1.8.1 Phase 1: Coronal plasma expansion and DL formation

As mentioned above, quick electrons moves rapidly and accelerate ions forming the plasma. The charge separation due to the flying electrons produces the electric field which causes the acceleration mechanism. This expansion

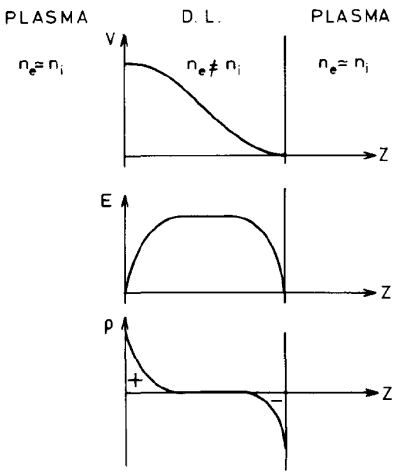

Figure 1.8.2: *Schematic description of the potential V, the electric field E and the charge density ρ in a static DL [22].*

stage is not easy to treat theoretically, especially when the laser power density increases, since many different plasma instabilities can occur. Moreover the fast particles expansion expires within the first $50-60nsec$ after the laser pulse termination (DLs manifest in LPP in the coronal part of the plasma plume). In this regime the formation of **DL-Double Layers** occurs. DLs are know as localized electrostatic potential structure created by two equal opposite space-charge layers, which are capable of sustaining high potential drops in collisionless plasmas. In DL the plasma quasi-neutrality is violated over lengths larger than λ_D (see figure 1.8.2). DLs represent highly non linear structures, and are considered as the principal activators of particle acceleration, plasmas auroras formation and solar flares [29, 30]. They are also know under the name of Debye sheaths defined in section 1.4.1 (a DL can also be defined as a positive-plus-negative Debye sheath, connecting two quasi-neutral regions of a small Debye-length λ_D plasma [31].).

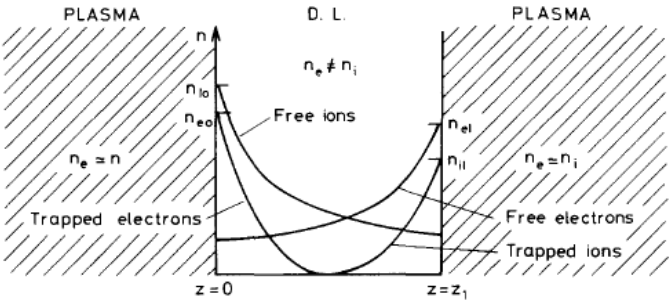

Figure 1.8.3: *DL structure following the Bohm scheme [22].*

The DL potential divides the plasma particles into four classes: free and trapped (or reflected) electrons and ions. Since the DL is located between two quasi neutral plasma regions, electrons from one of the two plasmas are reflected by the layer while the ions from the same plasma are accelerated. The roles of the charged particles in the second plasma is then reversed [22]. This structure is shown in figure 1.8.3. The DL thickness is supposed to be less than the mean free path (on the order of few Debye Length), therefore the effects of collisions are neglected. The same structure is shown in figure 1.8.4 in the phase space.

The charge separation in the DL is maintained by flux continuity of the free particles. Free particles consist in streaming electrons from $V = 0$ towards $V = V_{DL} = V_0$ and in streaming ions traveling in the opposite direction. Outside the DL, charge neutrality is maintained by trapped or reflected ions on the low potential side and trapped or reflected electrons on the high potential end [22]. Recently, a fifth group of counter-streaming electrons formed by the reflection of the accelerated electrons from the sheath was found by Lieberman et al. in [32].

The mathematical approach to describe DL is very elaborate. The elec-

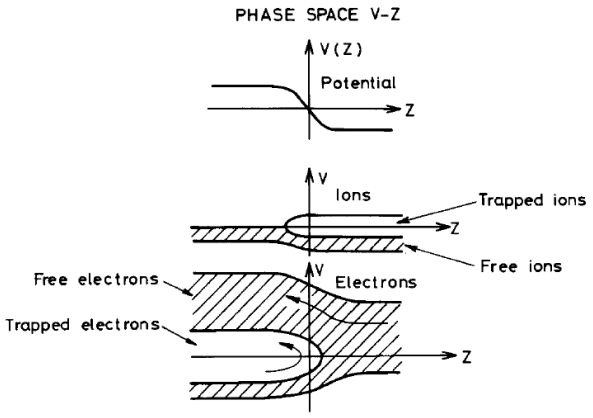

Figure 1.8.4: *Phase state description of a DL [22].*

tric field in DL is described by solving the Poisson equation that implies a self-consistent electric field even for neutral plasmas; this neutrality condition limits possible DL solutions and, in particular, the discontinuities in the plasma potential cannot be treated properly with the assumption of charge neutrality. In fact many analytical models and numerical hydrodynamic simulations for electrons and ions coupled by the Poisson equation have been performed including a violation of the space charge quasi-neutrality. Hora is one of the pioneers of theoretical treatment of DL [33] in laser plasmas, although we will report here only some aspects of the theory and remind to literature to the complete treatment ([33, 22]).

In a low power density regime ($\sim 2 - 25 J/cm^2$), a DL structure can manifest through double-peaked time-of-flight ion signals, as studied by Bulgakova et al. in [34]. Increasing the laser fluence, a transition region is observed and more than one DL can be observed, through multiple peaked TOF signals, as reported in figure 1.8.5. The different fast positive peaks can be attributed to different ion charge state groups, within several DLs

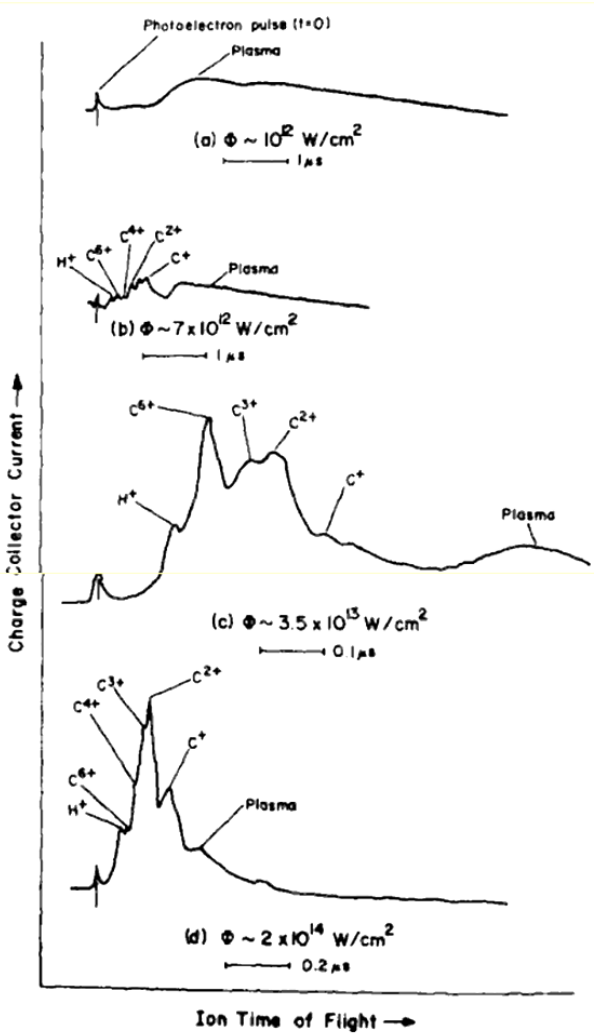

Figure 1.8.5: *TOF signals from ablation of Al and C target at different laser fluence obtained by Ehler et al. [33]*

are formed.

Increasing even more the laser power density, up to $10^{14} W/cm^2$, DLs can be formed by ponderomotive forces and strong non-linear plasma instabilities occur.

The presence of DLs in LPP can be supposed when the simultaneous existence of hot and cold electron population (which is indicated with TET-Two Electron Temperature) is detected. However also in a SET-Single Electron Population plasma DL can be formed [34].

TET presence in turn may induce **RSW-Rarefaction of Shock Waves** that is a DL. The RSW propagates with a steep front whose thickness is determined by the viscosity and thermal conductivity of the plume. RSW strongness depends on the **ratio** between the two electron population temperatures T_{hot}/T_{cold} [22].

The theoretical conditions for RSW is found by solving the equation of states, including conservation of mass, momentum and energy flux together with the Poisson equation (hydrodynamic equations), that leads to an electric field given by the formula:

$$E = -\frac{1}{en_e}\frac{\partial P}{\partial x} \tag{1.8.4}$$

where $E = -\frac{\partial \Phi}{\partial x}$ and P_e is the electron pressure. Assuming for the electrons an equation of state given by [22]:

$$P = P_e(\Phi) \tag{1.8.5}$$

and by solving the hydrodynamic equations in a adimensional form, a real solution is found only when a singularity condition is supposed [35]:

$$\frac{dP}{dV} \leq o \tag{1.8.6}$$

where $V = 1/Mn_e$, where M is the ion mass. Relation 1.8.6 can exist only in anomalous fluids. The same mathematical approach can be applied to TET-LPP that yields then to a solution by finding again condition 1.8.6. In this case the plasma behaves like an anomalous fluid with different thermodynamic properties.

In case of two electron plasma fluids expanding respectively with $\gamma_{hot} = 1$ and $\gamma_{cold} = 3$, the numerically condition for shock wave rarefaction is that $T_{hot}/T_{cold} \approx 9.9$. A more general result can then be obtained for the case of multiple electron fluids. Solving again the equation of state for a TET distribution expanding with the same $\gamma's$ values, rarefaction shock wave is obtained for $T_{hot}/T_{cold} = 5.4$.

1.8.2 Phase 2: Bulk plasma adiabatic expansion

In the early stages of the plasma formation, the density is very high so that the mean free path is very short determining a high collision rate. The plasma behaves in this stage as a continuum fluid and hence the gas dynamics equation can be applied to describe the its propagation [36]:

$$\frac{\partial \rho}{\partial t} + div(\rho \vec{v}) = 0 \quad (1.8.7)$$

$$\frac{\partial \vec{v}}{\partial t} + (\vec{v} \cdot \nabla)\vec{v} = 0 \quad (1.8.8)$$

$$\frac{\partial S}{\partial t} + (\vec{v} \cdot \nabla)S = 0 \quad (1.8.9)$$

Where ρ, p, $\vec{v}$ and S are the density, the pressure, the velocity and the entropy respectively.

The adiabatic expansion of the plume was first studied by by Sing and Narayan in [24]. A special solution of the 1.8.7 is able to describe the plume

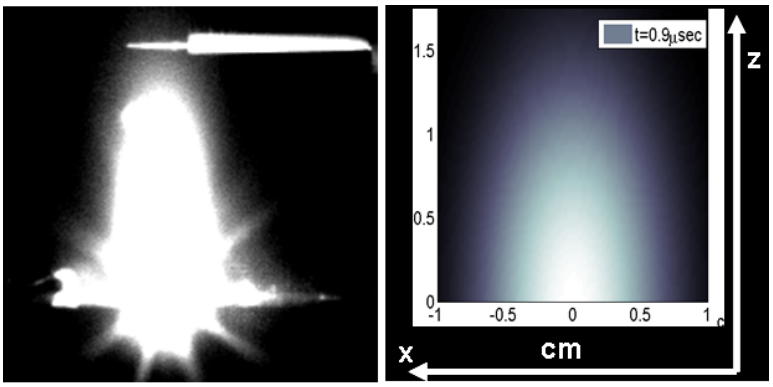

Figure 1.8.6: *Comparison of the real shape of the plume obtained with a CCD camera acquiring the plume image in a time window of* $1\mu sec$ *with a simulated plume obtained by means of the Anisimov model [5]. Above the real plasma a Langmuir Probe is located orthogonal to the plume expansion direction at* $1.5cm$ *from the target.*

propagation in terms of density and pressure gradient:

$$\rho(x,y,x,t) = \frac{N_T t}{\sqrt{2}\pi^{1.5}\tau X(t)Y(t)Z(t)} exp\left(-\frac{x^2}{2X(t)^2} - \frac{y^2}{2Y(t)^2} - \frac{z^2}{2Z(t)^2}\right)$$
$$P(x,y,x,t) = \frac{N_T t k_B T_0}{\sqrt{2}\pi^{1.5}\tau X(t)Y(t)Z(t)} exp\left(-\frac{x^2}{2X(t)^2} - \frac{y^2}{2Y(t)^2} - \frac{z^2}{2Z(t)^2}\right) \tag{1.8.10}$$

where N_T is the number of particles evaporated at the end of the laser pulse τ, and $X(t)$, $Y(t)$, $Z(t)$ are the dimensions of the expanding plasma and T_0 is the isothermal temperature of the plasma. However, as mentioned above, the Sing and Narayan model assumes an isothermal regime that doesn't describes properly the plasma expansion after the end of the laser pulse. An non isothermal regime was introduced by S. Anisimov in [36], by developing an adiabatic expansion plume dynamics. The model was used by several authors to describe the bulk plume propagation [4, 5, 37, 38],

comparing successfully the numerical data to experimental data in terms of size of the plume (see figure 1.8.6), plasma current signals, density and temperature gradients, confirming that the plume expands during this stage adiabatically and with no constant temperature. A revised version of the Anisimov model was also used in this work for the same purposes, for this reason it will be described in detail in chapter 5.

For the description of a plume expanding not in vacuum, but in an ambient gas, the Navier-Stokes equations must be used, passing from a conservative field to a dissipative regime in which viscosity terms prevails.

1.8.3 Phase 3: Free streaming expansion

The free streaming of the plasma plume starts when the plasma becomes spatially "broadened" during its last stage of expansion. The plume becomes collisionless since $L/\lambda_l \gg 1$ where L is the plasma length and λ_L is the mean free path. In this last stage the plasma expands isothermally. The begin of the free expansion can be estimated by comparing the simulated temperature (obtained with the Anisimov model), with the experimental temperature, or by studying the evolution of the different plasma velocity components. As we will see more in detail in the next chapter, the plasma velocity of the plume is composed by three different terms: the gas kinetic component, the flow velocity component and a velocity component due to the effect of the self-generated electric field inside the plasma. The flow velocity due the the adiabatic expansion of the plume, increases only within the Knudsen layer were collision occur, starting from the target surface until it assumes a constant value just after the layer. Then the plasma decays into the free flight and no longer collisions occur.

1.9 Plasma expansion in a background gas

As mentioned above, when the plume expands in a background gas, a different theoretical approach must be applied, since the collisional regime between the plasma particles and the ambient gas produces several expansion effects. However, solving the Navier-Stokes equations is not easy, so that different theoretical approaches have been developed by using drags and shock waves models. Depending on the value of the background gas pressure, free expansion, plume splitting and sharpening, hydrodynamic instabilities, stagnation or interpenetration of the plume through the background gas and possible formation of shock waves can occur [35]. A possible shock front is determined by the relaxation process that involves electrons and ions considered as two separate fluids, during the equilibration of the temperatures of both fluids. The shock front is also characterized by a rapid and sharp increase in space of the ion temperature and of the electron density and the front edge evolves spatial in time with a specific trend, which law is given in [35]. A gas heated by a strong shock wave radiates and the surface of the shock glows. The luminosity of the emission depends on the strength of the shock and the dimensions of the heated region behind the front.

Shock structures can be observed by high spatial resolved spectroscopic techniques, especially by using shadowgraphy [39].

Since deviations from the free plume expansion occur when the mass of the adjacent background gas at the plume periphery becomes comparable with the plume mass M_p, the radius of the hemispherical plume a is determined by the relation $2/3\pi\rho_g a^3 \approx M_p$, that in terms of gas pressure P gives

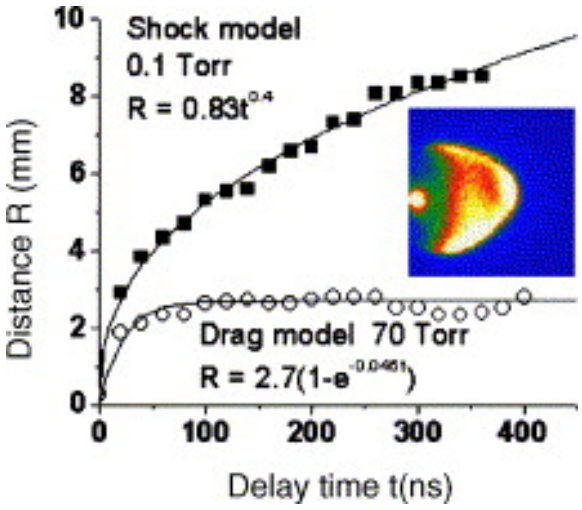

Figure 1.9.1: *Rt plot for the expanding aluminum plasma plume front in ambient nitrogen atmosphere at* 0.1 *and* $70Torr$. *Inset shows the formation of shock wave at* $0.1Torr$ *[40].*

[35]:

$$a = \sqrt[3]{\frac{3}{2\pi}\frac{M_p k_B T_g}{m_g}} P^{-1/3} \tag{1.9.1}$$

where k_B is the Boltzmann constant and ρ_g, T_g, and m_g are respectively the density, the temperature, and the atomic mass of the ambient gas. Plume propagation in a background gas with production of shock wave can be modeled with drag or shock models (see figure 1.9.1). A complete treatment can be found in [41]. However these models, which adequately describe the propagation of the slow component, don't reproduce the so called *plume splitting*. The plume splitting consist in the separation of a slow component, that is decelerated by the interaction with the ambient gas, and of a fast ion component that penetrate the background gas without significant collisions, and is statistically attenuated only with distance. Plume splitting

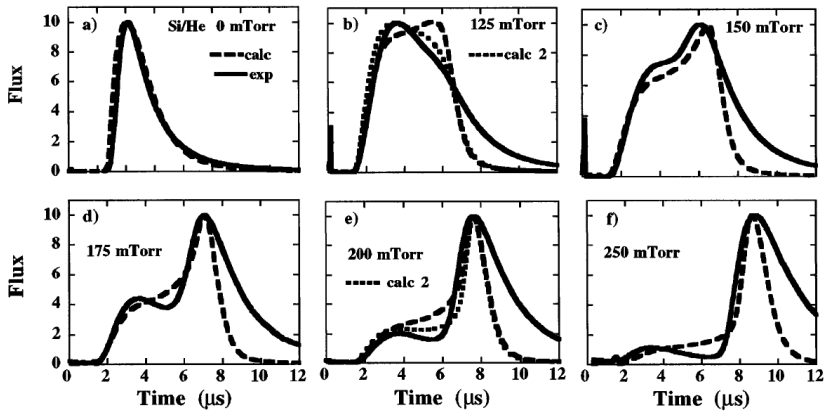

Figure 1.9.2: *Comparison of the experimental TOF signals and the theoretical TOF signal for different pressures; as we can observe from the figure, the model reproduces better the plume splitting for some specific background pressures.*

was observed by several authors, by recording time of flight signals of plumes propagating through background gases: Geohegan et al. observed in [42] an exponential loss of the ion flux that increases by increasing the background gas pressure. The same effect was observed also by Hariral et al. in [43] by means of high time resolved imaging of an *Al* plasma expanding at different background pressures. Several authors, like Wood et al. [44] attempted to model plasma plume expansion based on a combination of multiple elastic scattering and hydrodynamics formulations, providing a new solutions to the observed plume splitting. Figures 1.9.2 shows the comparison of experimental data taken by Geohegan et al. in [42] compared to the theoretical ones developed by Wood et al. We refer to literature to the complete discussion of the signals shown in figure 1.9.2.

1.10 Colliding Plasmas

The investigation of colliding plasmas was an unexplored research domain until the 1970s, when the first experiments were carried out by Rumbsy et al. in [45]. Their investigation has been devoted to a wide range of physical applications, going form ICF to LIBS, to simply study the physical interaction between the plumes. As mentioned in the introduction, colliding plasmas can reproduce in a laboratory-scale, astronomical processes as for example collisionless shock waves by employing thin targets [46, 47]. Plumes collision have also been used in indirect drive laser nuclear fusion systems: hollow hohlraums host multiple colliding plasmas as X-ray sources which then are used to drive fusion in the fuel cell located at the centre of the cavity [48]. The experiments mentioned above have been carried out with laser irradiances above $10^{14}W/cm^2$. At low power density, between $10^{11}W/cm^2 - 10^{12}W/cm^2$, experiments have been devoted to different applications, as for example, LIBS-Laser Induced Breakdown Spectroscopy [49]. In this case it has been show that heating of a preformed plasma with an intense laser pulse has the ability to increase laser absorption and it consequently enhances the emission intensity [50].

In a low laser energy regime, colliding plasmas can be created by splitting the laser pulse in two beams, then focused on several targets configurations[7]. This creates two plumes (called seeds) separated by a fixed distance generally between $1 < D < 10mm$, that as we will see in chapter 3, depends on the used optical geometries.

The seeds freely expand in vacuum until they start to collide when they

[7] on this purpose different targets configuration have been employed: orthogonal, V-shaped [21], parallel [51], etc.

overlap (see figure 1.10.1). Under these conditions, a third layer of plasma is formed at the collision front, called *stagnation layer*. At higher laser power densities, colliding plasmas can interpenetrate, i.e the plasmas pass through each other without any evidence of stagnation.

Which mechanism prevails, interpenetration or stagnation, depends on different physical parameters. During interpenetration the plasmas stream through each other and the main interactions consist in binary collisions (i.e, a low collision rate regime that facilitate interpenetration). In case of stagnation, the seeds rapidly accumulates in the collision region; this leads to the formation of a dense layer between the two seeds and to a high collisional regime is established. Rambo et al. [52] introduced the so called collisionality parameter ξ, to determine whether stagnation or interpenetration dominates during interaction. Note that in general the collisionality refers to the ratio of a plasma scale length L (its size for example) on the ion-ion mean free path λ_{ii}. If $\xi = L/\lambda_{ii}$ is much larger than unity the plasma is considered collisional, viceversa, the plasma is considered collisionless.

In case of colliding plasmas, L refers to the initial distance between the two interacting plumes (generally indicated with D): if $\xi = D/\lambda_{ii} \gg 1$ stagnation prevails on interpenetration, viceversa, for $\xi \ll 1$ interpenetration dominates on stagnation. ξ is described by the formula:

$$\xi = \frac{D}{\lambda_{ii}} \tag{1.10.1}$$

where λ_{ii} is the Spizter mean free path, given by the formula 1.10.2:

$$\lambda_{ii} = \frac{m_i^2 \nu_{12}^4}{4\pi e^4 Z^4 n_i ln\Lambda_{12}} \tag{1.10.2}$$

where ν_{12} is the relative velocity of the ions coming from the two plumes, Z is the average charge state of the plasma, n_i is the average plasma ion

density and $ln\Lambda_{12}$ is the Coulomb logarithm defined by equation 1.4.1. From equation 1.10.2 one can see that ξ strongly depends on ν and on n_e. Therefore, it can be varied by changing either (i) the separation between the two seed plasmas (D), or (ii) the on-target laser irradiance and hence the expansion velocity of the seed plasmas (v). In this way the level of plume interpenetration can be controlled. Inserting in the 1.10.1 the typical values of metal ablated plasmas with ND:Yag nanosecond laser pulse length (and irradiances on the order of $10^{10}W/cm^2 - 10^{12}W/cm^2$), i.e $n_i = 10^{18}cm^{-3}$, $< Z >= 2$, $n_{12} = 4 \cdot 10^6 cms^{-1}$, gives for $D \sim 1mm$, $\xi = 270$, that is much more higher than unity, hence stagnation prevails on interpenetration.

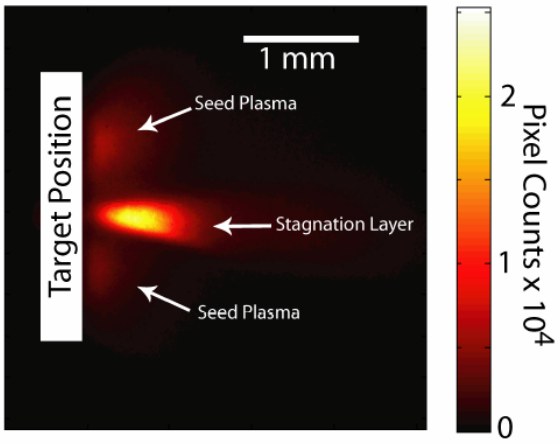

Figure 1.10.1: *Image of colliding laser produced aluminium plasmas and stagnation layer captured* $50ns$ *after creation of the seed plasmas with a flat target configuration. Each seed was created with a laser beam of energy of* $300mJ$*, wavelength of* $1064nm$ *and pulse-width of* $6ns$*, focused on two spots of diameter* $100mm$ *separated by a distance of* $1.3mm$ *[39].*

Some interesting studies put in evidence that electrons and ions stagnate

with different temporal dynamics: Hough et al. demonstrated that by employing a Nd:Yag laser at laser fluences on the order of $1.6 \cdot 10^3 J/cm^2$, for a flat target configuration shown in figure 1.10.1 electrons stagnate $10ns$ earlier respect to ions. The first electron collision front is observed at $\sim 30ns$, followed $10ns$ later single ionized Al ions. These measures put in evidence a peak of electron density exceeding $10^{19} cm^{-3}$ whose layer remained well defined over several hundred of nanoseconds. The delay between electron and ion stagnation was attributed to space charge separation effects in both seeds[8] supposing also a significant *screening* effect induced from the stagnation of the electrons at the mid-plane collision front [53]. Some correlations with ES were also found by numerical simulations in [2, 54] using the ZEUSMP2 code to simulate the interaction of two colliding plasmas; numerical results demonstrate that colliding plasmas can result usefuel to study ES, as we will see in chapters 3 and 4.

The effect of this screening has been further investigated also in the present work, by performing similar measurements on colliding plasmas at the Nation Centre for Plasma Science an Technology in Dublin.

1.11 Plasma Diagnostics

The investigation of LPP requires high time and spatial resolved diagnostic tools, in order to deduce information about its dynamics evolution, and to measure the main plasma parameters, like the electron density and the electron temperature, velocity distributions, charge stage distributions etc. Complete characterization of LPP is extremely difficult due to the number of physical processes involved in their expansion and to the number of pa-

[8] for seed we intend the single colliding plasma plume

rameters that have the ability to influence the plume properties (i.e the laser fluence regime, the target material etc.). For this reason there is no a unique diagnostics tool that can measure all the plasma parameters. Most of the techniques are only applicable over a specific range of plasma parameters, where specific theoretical assumptions are valid.

Many diagnostic tools have been developed with the aim to measure the electron density and electron temperature.

The different diagnostic methods are generally based on the direct detection of plasma charged particles (hence of plasma current), or on the detection of photons, i.e of plasma radiation. If the collisional processes discussed in section 1.4.1 prevails, detection of charged particles can result more useful; conversely, when radiation processes discussed in 1.4.2 dominate, spectroscopic techniques are more appropriate. Detection of charged particles is obtained through electrostatic probes, such as LP-Langmuir Probes and FC-Faraday Cups (called also IC-Ion Collectors).

One of the main advantages of using electrostatic probes, is that they can be located very close to the target surface so that bulk plasma can be characterized in terms of both electrons and ions dynamics. However, probes have the disadvantage to perturb the plume dynamics. This inconvenient can be overcome by placing the probe not to close to the target surface or by using appropriate experimental set-ups (see in chapter 2).

FC instead are mainly used to investigate the ion component. If a FC is couplet to an IEA-Ion Energy Analyzer, it is able to provide information on kinetic dynamics of each charge state composing the total plasma signal. However, data collected with ion collectors are generally acquired in the plasma free-flight region, i.e., away from the target surface. As an example,

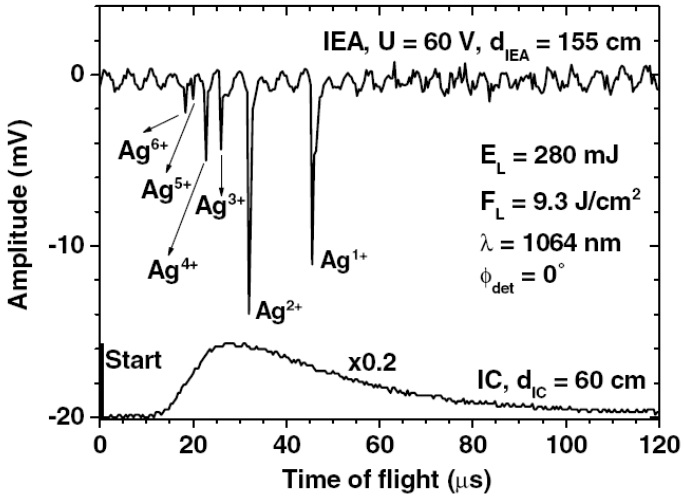

Figure 1.11.1: *Typical IEA-TOF spectrum (top) and simultaneous IC-TOF spectrum [55].*

in figure 1.11.1, a typical IEA spectra is shown together with the IC signal [55]. The IC signal is a convolution of all charge state signal of the plume. Only by knowing the exact amount of ion particle of each charge state the signal can be de-convoluted in the TOF signals for each charge state [4]. This information can be obtained only by employing IEA-Ion Energy Analyzers [55] or Re-Tof detectors [56].

Emission of radiation is measured by Spectrographs and Induced Charge Coupled Devices-ICCDs. Measurements based on radiation detection, such as optical spectroscopy and imaging have the advantage to be no-invasive for the plasma expansion.

The UV to near IR spectral range results very versatile to investigate single expanding plumes and also colliding plasmas in the laser energy regime of this work, since it requires easly available optics and CCD cameras with

ns time resolution and μm of spatial resolution can be employed in this spectral range. In the visible range however, only the coronal plasma can be investigated: to characterize the core plasma, detectors measuring radiation in extreme EUV [57] or Soft-X range [58] must be employed. However, in this case more complicated experimental set-ups are required, non even easy to realize in laboratory.

1.11.1 Electrostatic Probes

By biasing a LP or a FC at powers of about $-30V$ and by placing the detector at a certain distance (at least some few cms) from the target surface, a TOF - Time of Flight Signal can be obtained. The signal can be acquired in vacuum or in a low background gas ambient and read out with a electric circuit coupled to an oscilloscope. In this case a typical TOF signal is obtained like that shown in figure 1.11.1, recorded with the IC. From a TOF signal, information about the kinetic energy of the plume's center of mass, the mean energy of the collected ions and the total ion energy distribution function can be extracted.

Langmuir introduced in the 1923 the Langmuir Probe technique to measure the plasma density and the temperature, but also to measure the EEDF-Electron Energy Distribution Function [59]. LP are typically employed for arch discharge plasmas and magnetic confined plasmas, but recently it was employed also for LPP characterization. The operating principle of a LP is very simple, but the interpretation of the results is often arduous.

A LP is generally composed by a cylindrical or planar metallic tip with a high fusion point (tungsten, molybdenum), of few mm thickness or less (smaller than the typical plasma scale length), biased at different positive

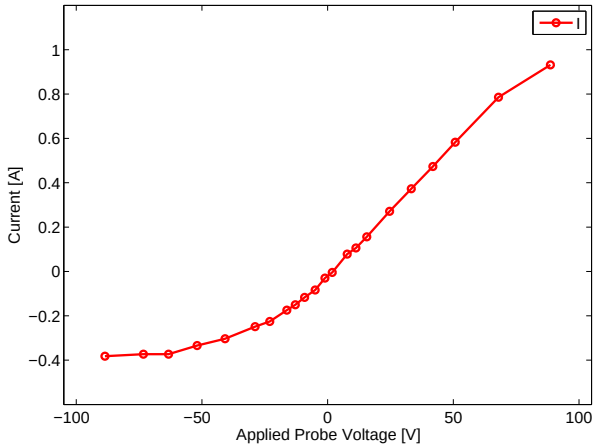

Figure 1.11.2: *Typical I-V curve obtained in this work during the study of the single plume dynamics (see chapter 2).*

or negative voltages (for example from $-60V$ to $+60V$ with volt steps of 5 or $10V$). The probe is then immersed in the plasma and collects the charged particles. Current (I) vs applied voltages (V) are then obtained. The curve is called characteristic $I-V$ curve and essentially measures the plasma resistivity. Since plasmas are not ohmic materials, the $I-V$ curves differs from a straight line: the trend of a typical LPP $I-V$ curve is shown in figure 1.11.2.

From an accurate analysis of the I-V curve, the plasma parameters can be obtained. Theory of Langmuir probe was presented initially for a steady and collisionless plasmas, with a Maxwellian electron velocity distribution by Mott and Langmuir in [60]. Then it was reviewed by Allen et. al in [61]. LP behaviour drastically changes from a collisionless to a collisional regime[9]

[9]To evaluate if collisions are ignorable the mean free path of the plasma particles must be compared to the probe size.

[62]. The first LP theory for flowing plasmas was developed Koopman in the 1971 in [63] with the aim to employ the Langmuir Probe technique also on LPP. When the probe is immersed in the plasma the potential drop between the plasma and the probe is mostly confined in a region whose length scale is comparable to few Debye lengths [62]. In the sheath, charge neutrality is violated and a strong electric field is generated. The sheath has the same physical meaning of a Double layer (section 1.8.1): when the probe is negatively biased, electrons are repelled and a sheath is formed with a thickness s_0 given by equation [64]:

$$s_0 = \left(\frac{2\epsilon_0 V_0}{e n_0} \right)^{0.5} \tag{1.11.1}$$

Once knowing the sheath thickness the I-V curve can be analyzed. In figure 1.11.3 a typical I-V curve is reported by including its analysis regions [59]:

As we can observe from 1.11.3 the I-V curve can be divided essentially in three regions; the first is the Ion Saturation Current region (as we will see in chapter 2 also in laser ablated plasma plume the ion current saturate jet at probe potentials $> 20V$ but only at the later stages of the plasma expansion). The Ion saturation current can be calculated by the formula 1.11.3 supposing that a sufficiently negative voltage is applied to the probe to prevent to high thermal energy electrons to reach the probe [62]:

$$I_i^S = e(v_i + v_{th}) n_i A_p \tag{1.11.2}$$

where v_i is the ion flow velocity due to the adiabatic expansion that determines the forward peaked distribution of the plume current signal (in some cases indicated with v_γ), n_i the ion density and A_p the surface of the probe

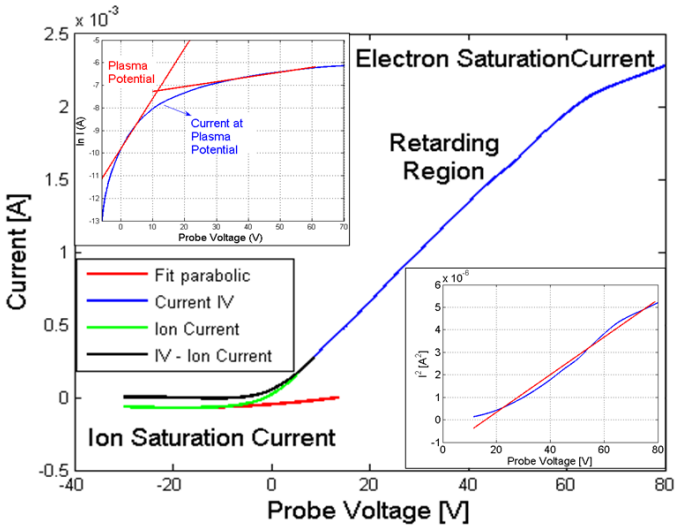

Figure 1.11.3: *Typical I-V curve of a LP reporting in different way the LP current vs voltage [59].*

immersed in the plasma. v_{th} is the Bohm or thermal velocity given by the equation:

$$v_{th} = \sqrt{\frac{k_B T_e + k_B T_i}{m_i}} \tag{1.11.3}$$

where T_e is the electron temperature, T_i is the ion temperature and m_i the ion mass. Equation 1.11.3 was then corrected by Koopmann introducing the contribution of the different charge states and a term due to secondary emission [63]:

$$I_i^S = (1 + \epsilon) e (v_i + v_{th}) \sum_{i=1}^{n} z_i n_i A_p \tag{1.11.4}$$

where ϵ is the secondary emission coefficient, n the number of charge states in the plasma plume and z the related charges, with its respective densities n_i. This formula can be further improved by including in the expansion

velocity a drift velocity term [5, 4]:

$$I_i^S = (1+\epsilon)e(v_{drift} + v_{th}) \sum_{i=1}^{n} z_i n_i A_p \tag{1.11.5}$$

where $v_{drift} = v_c + v_i$, i.e the sum of the Coulomb velocity v_c term indicated by equation 1.8.3 and of the flow velocity v_i.

Increasing the probe potential, at a certain value V_f called *floating potential*[10], $I(V_f) = 0$, that for laser generated plasma is usually close to zero. Then the retarding region, were the *knee* or *meniscus* of the I-V curve is located, is detected.

Assuming that the plasma electron component follows a Maxwell-Boltzmann thermal distribution, the current collected by the probe over the region where $V < Vp$ can be written, according to the Langmuir theory [60], by the equation:

$$I_e^S = n_e e A_p \left(\frac{k_B T_e}{2\pi m_e}\right)^{1/2} \tag{1.11.6}$$

where $v_e = \sqrt{\frac{k_B T_e}{2\pi m_e}}$ is the thermal electron velocity and n_e the electron density. If $V < Vp$ the electrons feel a negative repelling potential $(V_p - V)$ and only the ones whose energy is higher that the applied tip voltage can reach the probe. Then this part of the $I - V$ curve gives information about the EEDF- Electron Energy Distribution Function. It works like an energy selector, reconstructing the EEDF. The plasma potential can be evaluated in two ways: by calculating the first derivative of the $I - V$ curve or by the intersection of the two fitting lines shown in the upper subfigure of 1.11.3, by plotting the lnV vs. V. The electron temperature will be obtained from

[10] If a negatively biased probe would be electrically insulated from other parts of the plasma, hence it will be floating and it would rapidly charge up until net electrical current brought by electrons or ions go to zero.

the the slope of the natural logarithm of the $I - V$. From equation 1.11.6, once known T_e the electron density is evaluated.

The square of the current versus the voltage (see down subfigure of 1.11.3) permits to determine the density in an alternative way, i.e by means of the OML-Orbital Motion Limited theory that applies when $\lambda_D > r_p$, where r_p is the probe radius (Eq. 1.11.6 refers to plasmas where $\lambda_D \simeq r_p$):

$$I_e^S = \frac{2}{\sqrt{\pi}} n_e e A_p \left(\frac{k_B T_e}{2\pi m_e}\right)^{1/2} \left(\frac{eV}{k_B T_e} + 1\right)^{1/2} \tag{1.11.7}$$

According to 1.11.7 it is possible to determine the electron density the temperature, thus reducing additional sources of errors [65].

Not only the charge collection depends on the probe sizes and shape, but also on the direction in which the probe is located with respect to the plasma flow direction [64]. We will discuss this in detail in chapter 2.

1.11.2 Time and Spatial resolved spectroscopy

The atomic theories and physical parameters used to relate emission of radiation in the electromagnetic spectrum, rely all on the exact knowledge of the atomic transitions causing a certain line emission. Plasma spectra can be studied in terms of line broadening. Therefore we need to define the Einstein Coefficient; considering an atom which transits from an energy level E_1 to another of one of lower energy E_2, the emitted radiation can have different wavelengths of well defined energy and line shape. The transition probability is is shown schematically in figure 1.11.4 [18, 66]: In figure 1.11.4, A_{ba} is the Einstein coefficient for spontaneous emission, B_{ba} denotes the coefficient for stimulated emission and B_{ba} is the absorption coefficient [21]. The Einstein coefficients can be determined assuming that the atoms

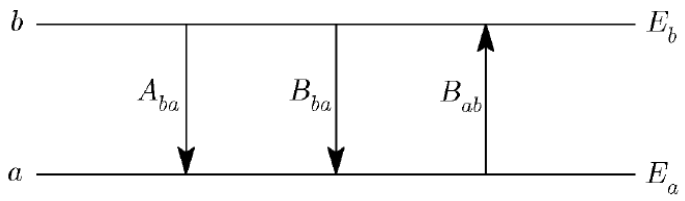

Figure 1.11.4: *Transition Probability through Einstein coefficients.*

are in CTE, hence a Boltzmann distribution of the number of atoms can be supposed. The value of A_{ba} is given by the formula [18, 66]:

$$A_{ba} = \frac{2\pi e^2 \nu^2}{mc^3 \epsilon_0} \frac{g_b}{g_a} f_{b,a} \tag{1.11.8}$$

where ν is the photon frequency, g_b and g_a are the statistical weight of the two energetic level involved in the transition (or state degeneracies), and $f_{b,a}$ is the *oscillator strength* representing a measure of the ability of the atom in a state a to undergo in a state b by absorbing a photon $h\nu$ [18]. B_{ba} and B_{ba} are related to 1.11.8 through the formula:

$$\begin{aligned} B_{b,a} &= \left(\frac{\hbar \omega_{b,a}^3}{\pi^2 c^3} \right)^{-1} A_{b,a} \\ g_a B_{ab} &= g_b B_{ba} \end{aligned} \tag{1.11.9}$$

When the transition occurs, the line shape is related to the lifetime of the upper state of the transition but it is also influenced by **external perturbations** that in turn influences the velocity distribution of the emitting species. Hence the difference between the energy levels never respects the theoretical formula given by:

$$\omega_{12} = \frac{\Delta E_{12}}{\hbar} \tag{1.11.10}$$

Equation 1.11.10 would lead to an *infinite sharp spectrum* but obviously this never occurs since the Heisenberg principle would not be respected.

Hence different line broadening, i.e Natural, Pressure and Doppler, Stark broadening (due to the electric fields) and Zeeman effect (due to magnetic fields), affects the spectral lines. To evaluate the plasma parameters, like density and temperature, the underlying line broadening must be known. Moreover, the broadening due to the apparatus itself must be taken into account [67].

We describe briefly the principal line broadenings:

- **Natural Broadening**

  From the Heisenberg uncertainty principle, $E = \frac{\hbar}{t}$, therefore there is a finite probability that photons will be emitted with energies in an interval centered in ΔE_{12} of width $(\hbar/\tau_1 + \hbar/\tau_2)$ where τ_1 and τ_2 are the lifetimes of the states 1 and 2. Broadening due to the lifetimes is called natural broadening and leads to a Lorentzian intensity distribution function given by equation [8]:

  $$\Delta_L(\omega) = \frac{\frac{\Gamma^2}{4\hbar^4}}{(\omega - \omega_{21})^2 + \frac{\Gamma^2}{4\hbar^4}} \tag{1.11.11}$$

  where $\Gamma = \hbar/\tau$. This is the minimum possible broadening that can be observed, and it is extremely difficult to be distinguished since it is mixed with other broadening mechanism. Generally the natural width of the lines is beyond the resolution of most if the typical laboratory spectrometers [21]. Such broadening is negligible for visible and infrared lines, but may be significant in the EUV range [20].

- **Pressure Broadening**

  Pressure Broadening is due to the interaction between photon emitters and the surrounding particles. It is divided in three categories: **Resonance**, **Van der Waals** and **Stark Broadening**. Stark effects, the

main cause of pressure broadening in our laser regime, is caused by the electric fields produced by nearby ions and electrons, or by collective fields associated with plasma waves [66].

The Stark effects leads to a broadening of line intensity with a FHWM given by equation [66]:

$$\Delta\lambda_{FWMH} = 2w\left(\frac{n_e}{10^{16}}\right) + 3.5A_i\left(\frac{n_e}{10^{16}}\right)^{0.25}\left[1 - 1.2N_D^{-\frac{1}{3}}\right]w\frac{n_e}{10^{16}} \tag{1.11.12}$$

where n_e is the electron density, w is the electron-broadening parameter, A_i the ion-broadening parameter that can be found in literature for different elements [68] and N_D is the Debye sphere. It is important to remark that in a hot dense plasma, Stark broadened lines can also be shifted of a distance d with respect to the line emission wavelength λ_0, due to electric fields of the nearby particles that perturb the energy level of the emitter. The shift can be calculated from by formula:

$$\Delta\lambda_{shift} = d\left(\frac{n_e}{10^{16}}\right) + 2A_i\left(\frac{n_e}{10^{16}}\right)^{0.25} \times \left[1 - 1.2N_D^{-\frac{1}{3}}\right]\omega\frac{n_e}{10^{16}} \tag{1.11.13}$$

Equation 1.11.12 and 1.11.13 can be applied for $N_D > 2$ and $A_i\left(\frac{n_e}{10^{16}}\right) < 0.5$. Stark broadening of lines in low ionized species is dominated by electron collisions. This permit to omit A_i in many cases and for low energy laser plasmas, so that the formula 1.11.12 becomes equal to:

$$\Delta\lambda_{FWMH} = 2w\left(\frac{n_e}{10^{16}}\right) \tag{1.11.14}$$

Equation 1.11.14 can be applied at the early stage of the plasma evolution, where the electron density is relatively high. The main difficulty when using Stark broadening is the deconvolution of the Lorentzian

profile from the experimental line shape, since the experimental profile can also be affected by Doppler and instrument broadening[11].

- **Doppler Broadening**

  Doppler broadening dominates when the electron density is relatively low and the temperature high; it is interpreted in terms of atom or ion thermal motions within the plume. Assuming a Maxwellian velocity distribution with temperature T, Doppler broadening leads to a a Gaussian line profile of full width half maximum (FWHM):

$$\Delta\lambda_{12} = 7.16 \cdot 10^{-10}\lambda_0\sqrt{\frac{T}{M_A}} \tag{1.11.15}$$

  where M_A is the atomic mass, λ_0 is the center wavelength in nanometers and T is the temperature in K. Doppler broadening contributes more to width of spectral lines at high temperatures and in low-z elements where the velocities of the photon emitters are usually larger.

Given a certain plasma line emission profile, Stark broadening leads to a *Lorentzian shape* and Doppler broadening leads to a *Gaussian profile*. These are the most influent broadening in LPP. An emitted line is hence composed by both shapes that can be fitted with the so-called Voigt Profile, representing the convolution of the Lorenztian and the Gaussian shape. This profile is generally used to fit experimental line profiles thus finally permitting to evaluate the electron plasma density. Voigt profiles are approximately Gaussian around the central frequency λ_0 and Lorentzian on the edge of the line shape.

[11] instrument broadening is determined by the effect of the optical system on the line width; its influence on the gaussian width can be determined experimentally

The Voigt function can hence be expressed by equation:

$$\mathcal{V} = \mathcal{L}(\omega_l - \omega) \otimes \mathcal{G}(\omega_0 - \omega) \tag{1.11.16}$$

In figure 1.11.5, the Gaussian and Lorentzian profiles are shown. In the

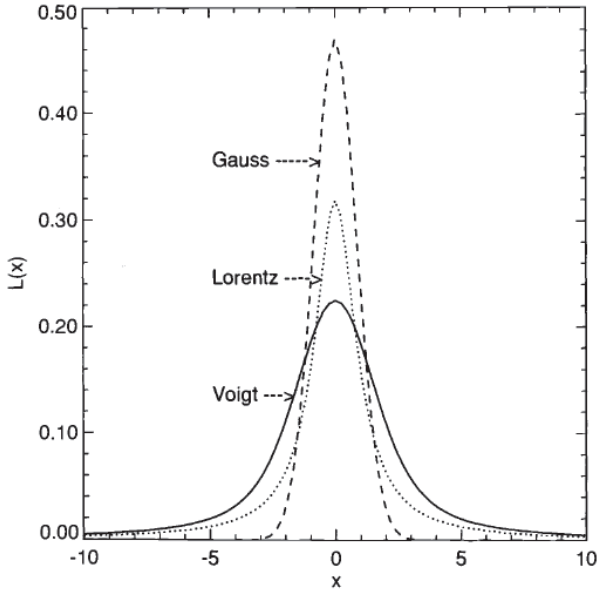

Figure 1.11.5: *Normalized Gauss and Lorentz profiles of equal half widths (FWHM width = 2 in x-units) and the Voigt profile resulting from the convolution of these two profiles [66].*

same figure their convolution is reported: i.e the Voigt profile.

In order to evaluate from emission spectroscopy the electron temperature, in LPP a common used method is Line Ratio. The three most used techniques are: line-to-line from the same or different ionization stage or line-to-continuum ratio.

- **Line to Line from the same ionization state**

In this case the two emitted lines I_1 and I_2 centered at wavelength respectively of ω_1 and ω_2 are referred to two excited state populations, with the same ground state level. The temperature can be extracted from the formula [66]:

$$\frac{I_2}{I_1} = \frac{\omega_2 A_2 g_{b2}}{\omega_1 A_1 g_{b1}} exp\left(\frac{E_{b2} - E_{b1}}{k_B T}\right) \tag{1.11.17}$$

where A_1 and A_2 are the oscillator strengths of the two excited states and g_{1b} and g_{2b} the statistical weight. The obtained electron temperatures are affected by an error, at least, of the 10%. The accuracy of this method can be improved by measuring line ratios along some spectral series. The logarithm of the intensity ratio, versus the excitation energies of the upper levels, should produce a straight line. The reciprocal of the slope of this line will yield a more accurate value of $k_B T$ (the so called Boltzmann plot). Consistent deviations from a straight line plot are a significative of a possible no LTE. Errors on the evaluation of T_e can be due by underlying continuum emission in the spectrum [21]. To accuracy of the temperature evaluation can be improved by using Line-to-Line Ratio from successive charge states.

- **Line-to-Line ratios from successive charge states**

  In this case an additional energy gap E_∞, that represent the ionization energy, usually leads to an energy separation of the levels larger than $k_B T$. Instead of relating the integrated intensity ratios using the Boltzmann plot, the intensities are related by the Saha equation. The temperature can be obtained in this case, by the formula [66]:

$$\frac{I'}{I} = \frac{\omega' A' g'}{\sqrt{\pi}\omega A g} \frac{1}{4\pi a_0^3 n_e} \left(\frac{k_B T}{E_H}\right)^{3/2} exp\left(-\frac{E' + E_\infty - E - \Delta E_\infty}{k_B T}\right) \tag{1.11.18}$$

where n_e is the electron density, E_H the Rydberg Energy, E' and E are the excitation energies of the transitions of interest in the successive ion stages, E_∞ is the ionization energy of the lower of the two ion stages and ΔE_∞ is a correction factor for high density plasmas causes that lowers the ionization energy due to the presence of strong electric fields.

- **Line-to-Continuum**

  At the early stage of the plasma expansion the emission spectra may be affected by continuum emission. In this case the line ratios equations 1.11.17 and 1.11.18 cannot be used. If the intensity of the continuum and the line emission are comparable, a third formula can be used to evaluate the density given by equation 1.11.19

$$\begin{aligned} \frac{\epsilon_l}{\epsilon_c}(\lambda) &= C_r \frac{A_{21}}{U_i}\frac{\lambda_c^2}{\lambda_l T_e} exp\left(\frac{E_\infty - E_2 - \Delta E_\infty}{k_B T}\right) \\ &\times \left[\xi\left(1 - exp\left(\frac{-hc}{\lambda k_B T_e}\right)\right) + G\left(exp\frac{-hc}{\lambda k_B T_e}\right)\right]^{-1} \end{aligned} \tag{1.11.19}$$

  where $C_r = 2.005 \cdot 10^{-5}(sK)$, ϵ_C is the continuum emission coefficient and ϵ_l is the integrated emission coefficient over the line profile. λ_C and λ_l are respectively the continuum centre wavelength and the centre wavelength of the line, E_2 is the upper level energy, U_i is a partition function, G is the free-free Gaunt factor and ξ is the free-bound continuum correction factor [66]. The relative line-to-continuum technique only yields accurate results when the intensity of the continuum and the line emission are comparable. The technique is reliable from approximately $30 - 100ns$ of the plasma expansion time.

1.12 Conclusions

In this chapter the theoretical treatment of a nanosecond laser generated plasmas have been discussed. The main characteristic of a LPP can be summarized as follows.

When the laser intensity is high enough, the target material undergoes either normal vaporization, explosive vaporization, or boiling. The subsequent interaction of the dense vapor with the laser beam, in proximity of the sample surface, leads to strong heating and ionization of the vapor, i.e. to plasma formation. Although some species can be directly vaporized as ionized fragments, plasma formation can be mainly ascribed to a number of processes taking place in the second step. Amongst the various processes, for metal targets, three are particularly effective in promoting the plasma formation. Firstly, the free conduction-band electrons gain kinetic energy from the laser radiation field via inverse bremsstrahlung in the lattice field. This causes further ionization, thus leading to an avalanche process. Secondly, ionization is also produced by collisions of energetic ions with excited atomic and molecular species. Finally, at sufficiently high laser intensities, multiphoton ionization of ground-state neutral species as well as photoionization of excited atoms and molecules occurs. The minimum fluence needed to detect charged species in the vaporized material is defined as the ablation threshold, (e.g. $7 J/cm^2$ for Al target). Successively the vaporized material expands in vacuum at supersonic velocities. When the desorption yields are relatively high the particles go through a typical sequence forming a Knudsen layer (the near-surface region where the particles come to equilibrium each other), successively undergoing to an unsteady adiabatic expansion, and finally entering into the free flight region. The expansion dynamics of

the plasma cloud in vacuum can be described by simple analytical models which are qualitatively able to reproduce the experimental results. Increasing the fluence over the ablation threshold, the saturation of the produced plasma density allows the increase of the ions and electrons temperatures. In this regime, some authors experimentally observed the appearance of a new mechanisms leading to the formation of non-neutral plasma regions which induce a large potential drop, causing very strong electric fields (DL - double layers formation) [6]. Due to the complicate laser-matter interaction and subsequent plume expansion, theory models and diagnostic tools discussed in this chapter must be employed not only according to the laser energy regime, but also accurately selected for the different expansion stages.

Chapter 2

Characterization of a single Aluminum plasma expanding in vacuum and in a background gas

In this chapter the experimental results regarding the characterization of an Aluminum single plasma plume expanding in vacuum and at different background pressures will be presented.

2.1 Introduction

The experimental tools used in this work were very versatile in order to investigate both single and colliding plasmas expanding in vacuum and at different background pressures. The first measurements were carried out on a single Al plasma. The dynamics of the plume are mainly studied by

means of time of flight measurements. The experimental set-up and the high fluence regime permitted us to detect a very peculiar plume expansion, pointing out a *transitional regime* between the classical adiabatic expansion and non linearities generating fast particles.

2.2 The Experimental set-up

We describe hereby the new experimental apparatus. All experimental components were constructed and homemade at the LNS-INFN of Catania. The apparatus was then installed at the DMFCI of Catania. The main measurements were realized by means of electrostatic probes (see section 1.11.1), which was placed very close to the target surface. A gateable CCD camera permitted us to obtain the plasma imaging in the early stages of the plume formation.

2.2.1 The vacuum chamber

The core of the experimental set-up consists of a stainless steel cylindrical vacuum chamber with $250mm$ of diameter and $240mm$ of height. Several types of flanges have been assembled with the chamber; four $DN40$ flanges are located at 90 degrees with respect to the chamber axis, while additional $DN25$ and $DN16$ flanges form angles going from 15° to 45° with respect to the chamber axis [3].

The vacuum chamber was then fixed on a rectangular stainless steel plate of lateral dimensions of $600mm$. The plate hosts four small rectangular supports located ad each angle, where mirrors and beamsplitters will be placed in the next future allow to operate in "plume collision" configuration. Lines of drilled threaded holes located at 15° from each other, and irradiating from

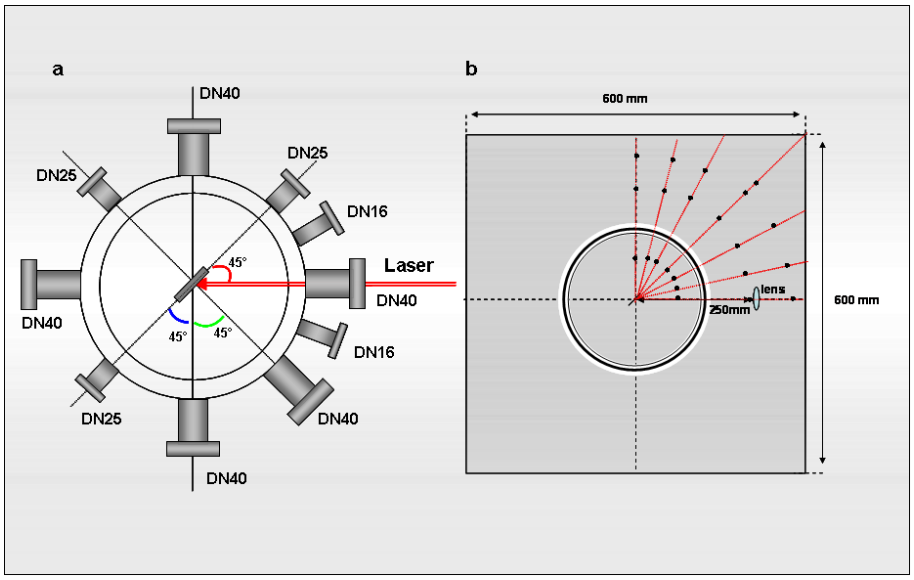

Figure 2.2.1: *Scheme of the vacuum chamber (a), and the optical plate (b).*

the plate centre, served to host optical devices at fixed positions. Supports for optical devices (lenses, mirrors etc), part of diagnostics tools (like the Faraday Cup for the time of flight measurements) and other devices were designed and homemade at LNS. A scheme of the vacuum chamber with the optical plate is reported in figure 2.2.1.

The target holder was mounted on the top of the plasma chamber through a $DN40$ flange. A linear stage permitted us to move with millimetric steps the target surface, so that all measurements where done with fresh target at each laser shot.

The vacuum system was composed by a Pfeiffer Rotative Pump and a Varian turbo molecular pump. The minimum operating pressure obtained in vacuum was $1 \cdot 10^{-6} mbar$. Measurements in background gas were performed by increasing the pressure; the air flux was controlled by means of

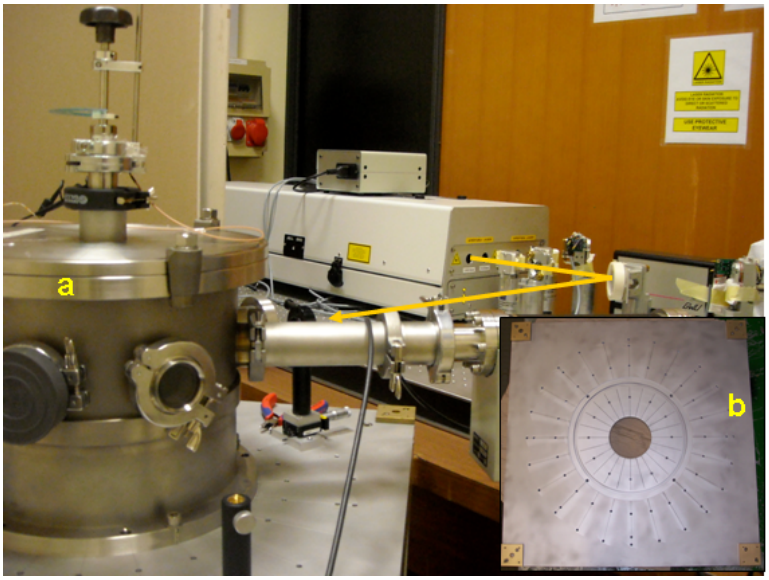

Figure 2.2.2: *Picture of the vacuum chamber (a), the optical plate (b) and the laser line (orange arrow).*

an Unilever valve.

2.2.2 The Quanta Laser system

The laser used for the experiment is a Quanta System GIANT ND:Yag. Emission is in pulsed mode with a maximum energy per pulse of $600mJ$ in Q-switch mode for the oscillator and up to $2J/pulse$ by using additional amplifiers. The fundamental wavelength is $1064nm$; it operates also at the $2th$, $3th$ and $4th$ harmonic. The maximum rate per pulse is of $30Hz$. The laser beam diameter is of $7-9mm$ with a divergence of $0.5mrad$. The duration of the pulse is of $6ns$. The laser system has a power supply system with a *control unit* provided of a $RS232$ port to remote control the system by PC; four BNC connectors, 2 output and 2 input, respectively for two

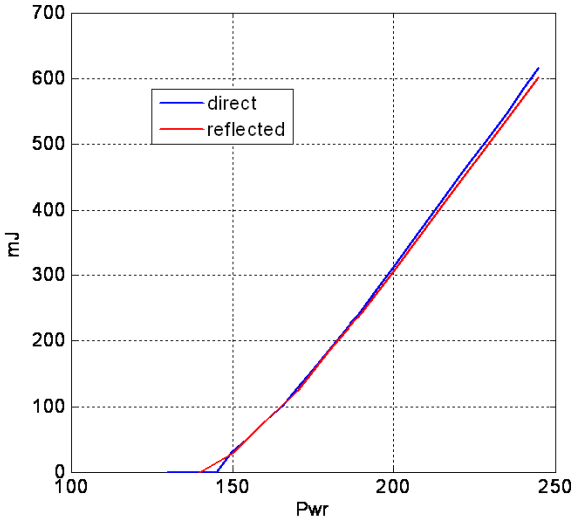

Figure 2.2.3: *Real laser energy vs Nominal Power Laser (PWR) before (blue line) and after accrossing the mirror (red line).*

Q-switch oscillator flash lamps and for the trigger system (Q-switch trigger and external trigger) are also employed. The power supply has also a main line breaker and a capacitor charger with a water cooling unit. The laser beam was launched towards the target surface by a 45° laser line mirror with a reflectivity of the 99% for the fundamental wavelength and focalized on the target with a $25mm$ focal length plano convex lens (see figure 2.2.2). We obtained spot sizes on the order of $100\mu m$. The laser nominal power (the one visualized on the screen of the power unit) was calibrated by means of a power meter to test the performances of the laser and to measure the reflectivity of the mirror. The calibration is shown in figure 2.2.3. As we can observe from the figure, an energy of $600mJ$ corresponds effectively to a maximum nominal power of $245pwr$, that was our operating value during all the measurements performed in this work.

2.2.3 The Langmuir Probe

The Langmuir Probe is an ESPion Advanced LP. A motor moves the probe with a total range of $300mm$ and with a minimum step of $0.5mm$. The core of the probe consists of $5mm$ long cylindrical tungsten thin tip, with a diameter of $0.15mm$, connected to a rigid $300mm$ long coaxial cable, having a thickness of $3mm$. The tip protrudes from an alumina sheath which covers the coaxial cable. The LP is shown in figure 2.2.4. It was powered with a HP power supply of $100V$ maximum voltage and $3A$ of full scale current; the signal was read out with a BNC feedthrough. By placing the probe so close to the target surface currents on the order of several of hundred of mA were recorded. We hence realized the electric circuit shown in figure 2.2.5 in order to read out the probe signal.

This circuit configuration permitted us to know exactly the current value (on the order of several of hundred mA) flowing through the Probe. The current was determined by the equation:

$$I = \frac{V_p}{R_{eq}} \tag{2.2.1}$$

and the related equivalent resistor R_{eq} was obtained by the formula:

$$R_{eq} = \frac{R_o}{R_o + R_2} \cdot \left(\frac{1}{R_1} + \frac{1}{R_o + R_2} \right)^{-1} \tag{2.2.2}$$

where $R_o = R_{scope} \parallel R_3 = 25\Omega$. The value of R_2 varies between 100Ω and 500Ω depending on the divider needed to fit the LP signal on the scope screen.

The absolute value of I is crucial, if one wants to estimate the correct electron plasma density (see section 1.11.1). In this sense many of the LP measurements reported in literature on LPP, show LP current signals on the

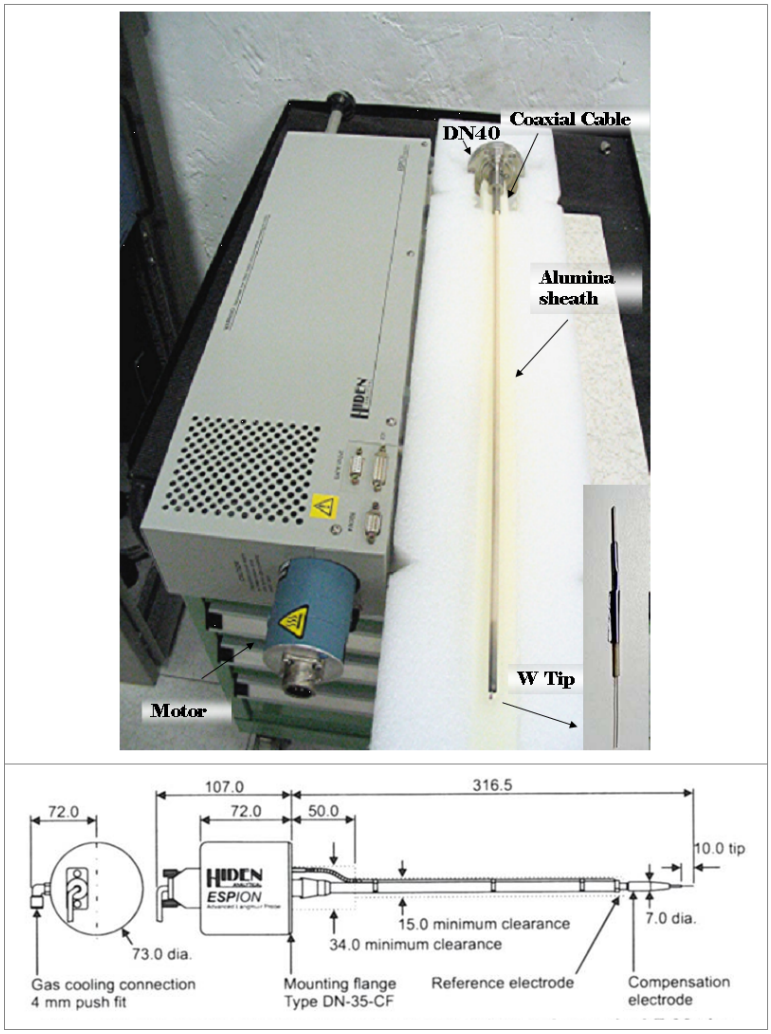

Figure 2.2.4: *Langmuir Probe and W Tip (left), technical draft of the LP (right).*

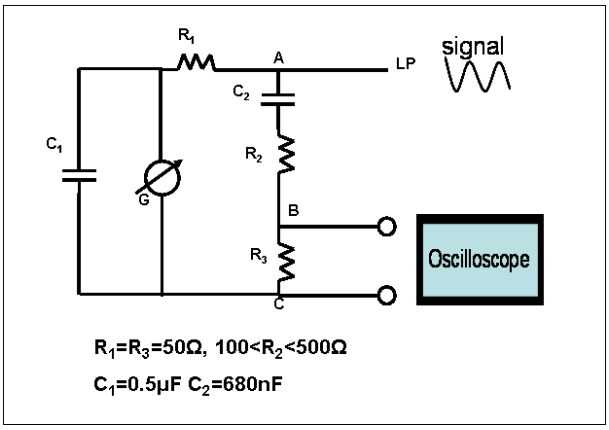

Figure 2.2.5: *Electric Circuit used to read out the LP signal.*

order of few mA, even at high laser fluence and even if the probe is located at few cm from the target. This occurs because the LP signal is frequently read out with simple RC circuit, without inserting a second resistor of smaller value, that in our circuit configuration 2.2.5 is indicated as R_1. By including R_1, the current coming from the LP divides in mesh A in two parts: one flows through R_1, and the other one flows through R_2C_2. In this way the absolute current value flowing through the probe can be exactly know. By inserting R_1, the real voltage biasing the probe must be corrected with the nominal value of the power V_N used for biasing the probe, by using the formula:

$$V_{lp}(t) = V_N + V_{AB}(t) \tag{2.2.3}$$

where V_{AB} is equal to:

$$V_{AB}(t) = I(t)_{pr} R_{eq} \tag{2.2.4}$$

where $I(t)_{pr}$ is the corrected voltage signal read out from the probe, and

$R_{eq} = (R_o + R_2)/(R_o)$.

2.2.4 The Faraday Cup

. The FC-Faraday cup consists of a $10mm$ length Cu cover with an external diameter of $22mm$ and a internal diameter of $18mm$. Inside the Cu cylinder a graphite disk with diameter of $18mm$ and $5mm$ of thickness was placed, followed alternatively by two disks of metal and two disks of insulator both of $1mm$ thickness and $18mm$ of diameter. The cup was covered by a $12mm$ length PCV cylinder, having a $24mm$ external diameter and a $22mm$ internal diameter, and placed finally in high vacuum conical flange so that the active area of the cup was $346mm^2$. The cup was placed at 120 from the target surface with a $100mm$ long $DN40$ flange and the signal was collected with a BNC feedthrough. The collector was powered with a HP power supply of $30V$ maximum voltage and $1A$ of full scale current and the signal was read out with a BNC feedthrough. Since the Cup was placed so far from the target surface, currents were on the order of few mA so that no electrical circuit was need to read out the signals.

2.2.5 The Imaging system

The CCD camera used for the plasma imaging is a diagonal $8mm$ interline with a squarepixel array and $1.45M$ of effective pixels. The maximum frame rate is $1/30sec$ and the minimum time acquisition window is of $2.3\mu sec$. It is equipped with an electronic shutter with variable charge-storage. High sensitivity and low dark current are achieved through a Hole-Accumulation-Diode. A image of the plume obtained with the camera is shown in figure 2.2.6. Also the LP is visible in the picture; here it was located orthogonal

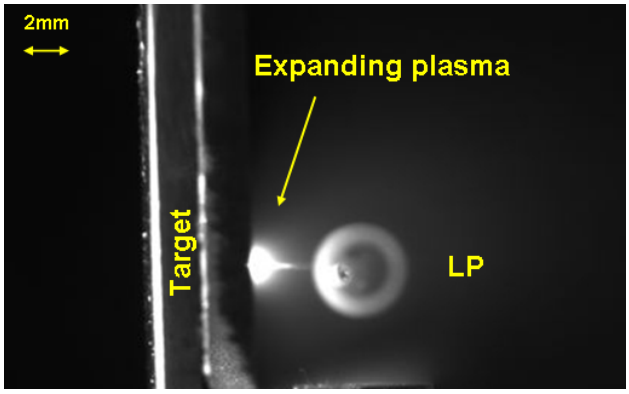

Figure 2.2.6: *Picture of the expanding plume obtained by means of the gatable CCD camera, when the LP was located orthogonal to the plume expansion direction.*

to the plume expansion direction at $0.5mm$ from the target.

2.2.6 The Signal acquisition system

Both time of flight signals, coming from the FC and the LP, were collected by means of a Textronik Oscilloscope. The timing of the system was obtained

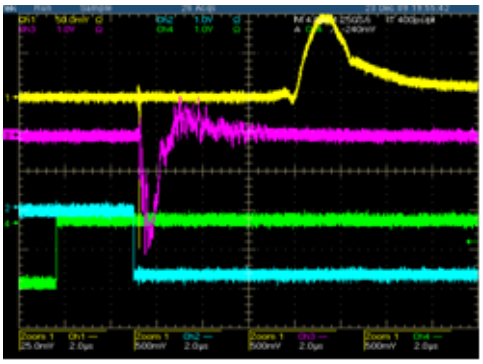

Figure 2.2.7: *Timing: Laser-blue signal, CCD-green signal, Faraday-Cup-yellow signal, Langmuir Probe-violet signal.*

through CAEN delay generators and LeCroy signal generators. In fig. 2.2.7 the synchronized signals are shown. The CCD camera was triggered $2.2\mu sec$ before the laser signal so that the acquisition window of the camera was of $100nsec$. The FC and the LP were also triggered with the laser through its external trigger switch, having a delay of $150nsec$ with respect to the laser pulse. However this delay was not influent since the photopeaks of the TOF signals[1], were used as the starter of the entire timing. The jitter of the photopeak was of $1nsec$ [3]. A final picture including the timing

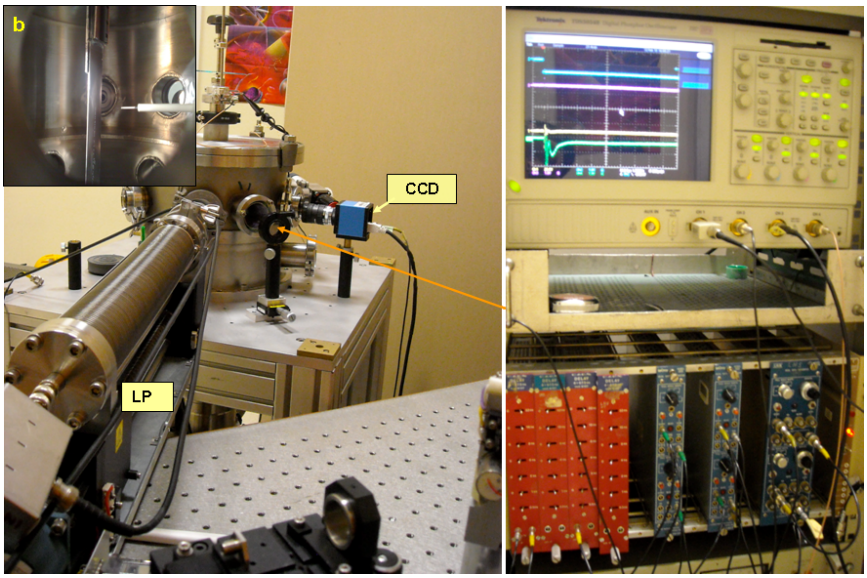

Figure 2.2.8: *The Experimental set-up (left) and the Timing System (right), with the diagnostic tools when the LP was located parallel to the target surface. Figure (b) shows the LP inside the plasma chamber when it was located* $4.5cm$ *far away from the target.*

[1]that corresponds to photoemission from the detector caused by EUV emission from the plasma under formation

system and the complete experimental set-up is shown in figure 2.2.8. The picture shows also the LP located parallel to the plume expansion direction at $4.5mm$ from the target. The box at the end of the LP contains the electric circuit described above.

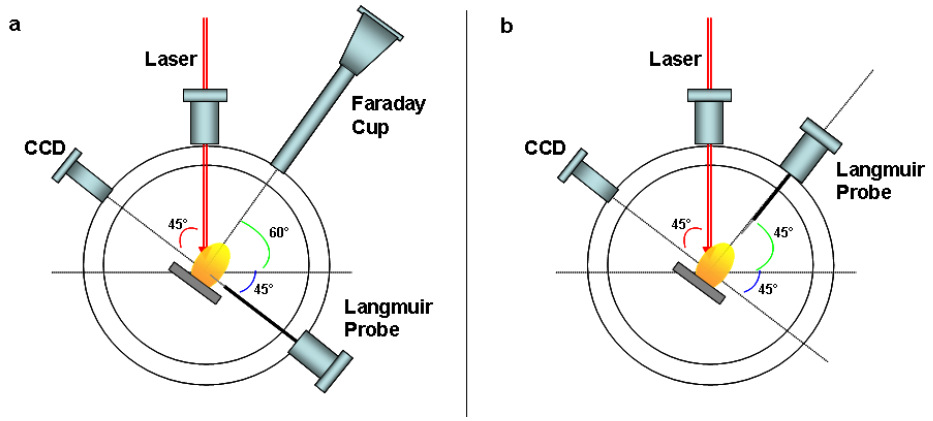

Figure 2.3.1: *Scheme of the two experimental set-ups.*

2.3 Experimental Results

Two different experimental configurations were arranged in order to study the evolution of the plume (they are reported in figure 2.3.1). In configuration (a) the LP was located orthogonally to the plasma expansion direction, and the FC was placed parallel, at 15°, from the plume expansion direction. The FC voltage was constant of $-30V$ and its signal was acquired for each laser shot and used as a *control* signal, since its voltage and its position was fixed for each laser shot. In configuration (b), the LP was placed parallelly to the plume expansion direction and the FC was removed.

In both experimental set-ups, the LP was biased from $-100V$ to $+100V$ with steps of $5-10V$ at each laser shot, in order to reconstruct off-line the $I-V$ curves (current vs applied voltage) in function of time.

In configuration (a) the probe was placed at $d_{LT}=15mm$ on axis and at $d_{LT}=33.7mm$ from the target off axis [2]. In configuration (b) the probe

[2]This position was chosen to make a further comparison with the results obtained in [65] on Tantalum targets

was placed at $d_{LT} = 15mm$ and at $d_{LT} = 4.5mm$ both on axis. Position $d_{LT} = 15mm$ was chosen for both configurations for a further comparison of the experimental results; an exact evaluation of the probe-target distance obtained by means of pixel-mm calibration from CCD images gave us the exact d_{LT}s: $d_{LT} = 15.3mm$ for the experimental set-up (a) and $d_{LT} = 14.5mm$ for the experimental set-up (b). TOF signals vs probe position where also acquired in this configuration, with no biased probe. Configuration (b) was also the experimental set-up used to perform the measurements in background gas.

Signals were also acquired from the grounded target: on this purpose a Scope-Probe was connected to the target holder by means of an electric contact. As an example, in figure 2.3.2 the target signal (TG), together with the LP current signal is reported. Below, the FC control signal is also showed. The target and the LP shapes are quiet similar, but shifted temporally of $\sim 200ns$; except from the first part of the signal, this trend is expected and looks like the FC one. The target acts in fact like a detector with a larger area, so that the signal is proportional to the total number of ions or electrons removed from the target after the laser ablation. A similar effect was also observed by other authors [69]. The LP signal reported in the figure was obtained with unbiased probe ($V = 0$). When $V = 0$ the probe collects either electrons than ions: they hit the probe attracted by a potential which is given by $V - V_p = -V_p$, where V_p is the plasma potential. The electrons are partially repelled whereas the ions are attracted. The LP signal can hence as follows interpreted: if $J_i > J_e$, the number of collected ions is larger than the electrons one, otherwise the probe shows a negative signal. Usually the ions dominates at such repelling voltages (V_p is typically

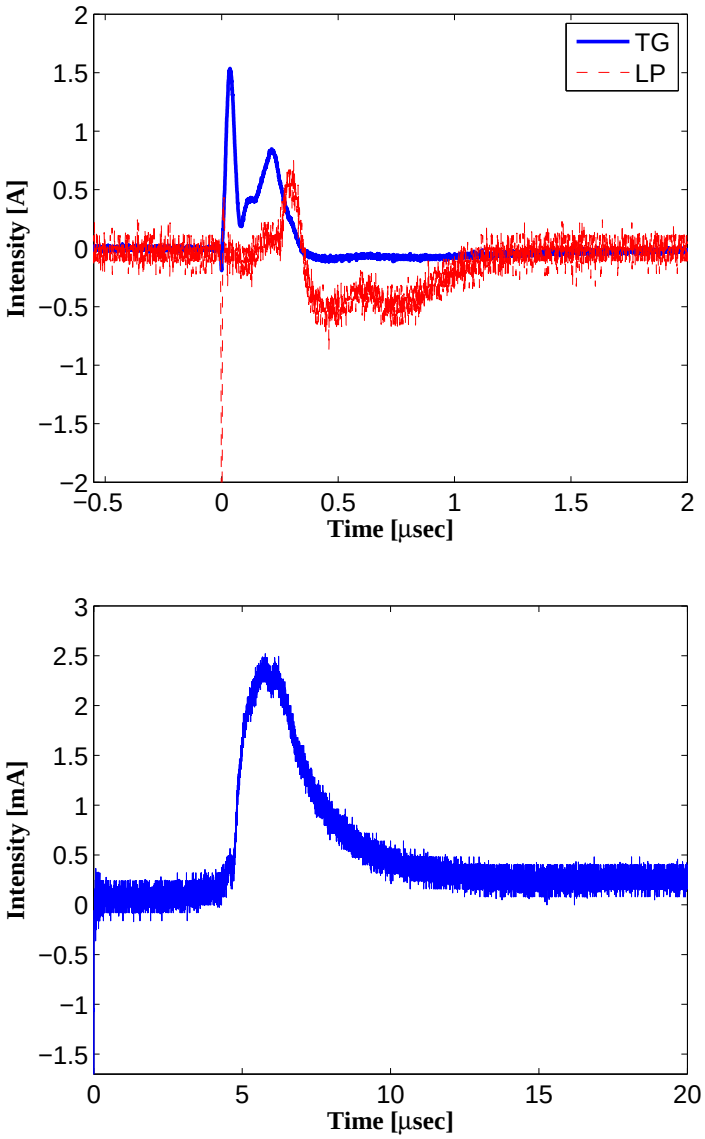

Figure 2.3.2: *Current signal obtained from the target (the signal was rescaled of* $\times 30$*)) compared with the LP signal for* $d_{LP} = 4.5mm$ *and* $V_p = 0$*, and FC control signal obtained by biasing ion collector with* $V_{IC} = -30V$*.*

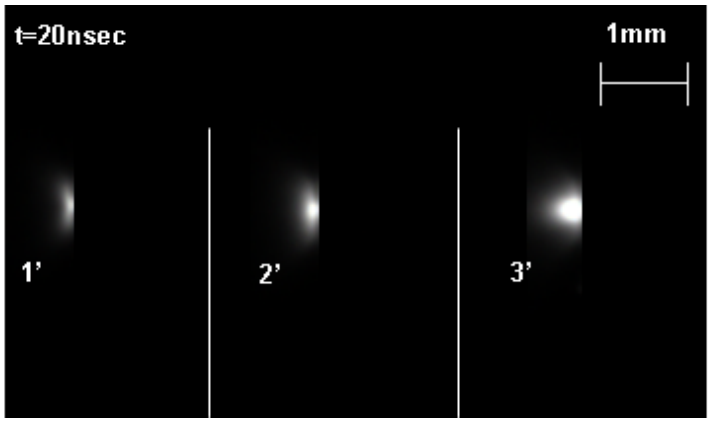

Figure 2.3.3: *CCD Images obtained with three consecutive shots, obtained at* $100ns$.

around $30 - 80V$, this means that electrons are repelled by a large negative potential).

The FC signal indicates the velocity of the ions at very large distances: they are on the order of $2 \cdot 10^5 m/s$, indicating a strong forward peaked ion distribution that evolves, rather than with the expected mean plume adiabatic velocities (on the order of $2 \cdot 10^4 m/s$ for metallic targets), more quicker. This is due to the high laser fluence regime and contemporary to the expansion of fast ions of different charge state, that with the FC cannot be discriminated: self generated electric field boots the ions velocity.

This dynamics will be investigated in detail in the next section and in chapter 5, where the plasma expansion will be simulated with the explicit assumption of a coulombian accelerating force. Another difference between the LP and the FC signals consists in the small structure which are visible with the LP and not with the FC. These fast positive peaks (a negative peak is also detected) will play a crucial role in the following analysis.

Table 2.1: *Target Composition*

Al	Si	Fe	Cu	Mg	Mn	Zn
99%	0.25%	0.05%	0.05%	0.05%	0.05%	0.07%

The CCD was triggered with the laser as explained in section 2.2.6, permitting us to obtain the imaging of the plume at the early stage of its expansion. On this purpose, in figure 2.3.3, three images of the plume are shown for three consecutive laser shots. The CCD gate was of $20ns$ (time exposure from the end of the laser pulse). As we can observe from the figure, the plume seems to be bigger for the $3th$ shot. This probably occurs because the laser is getting more focalized on the target surface after removing some μm of target material with the first two shots. On this purpose, we also performed some measurements firing the laser on the same target surface for 50 times, to observe the evolution of the crater depth: this data analysis is in progress.

Raman and $Pixel-\alpha$ analysis were finally used to reveal the exact target composition reported in table 2.1.

2.3.1 On the detection of the Multi-Layer structure

The time of flight signals obtained by placing the probe very close to the target surface (in our case from $d_{LT} = 2.5mm$ to $d_{LT} = 49.5mm$ with steps of $1mm$ or $2mm$) without biasing the tungsten tip resulted very useful to study the plume dynamics in the earlier stages. On this purpose, the TOF signals are reported in figure 2.3.4. As we can observe from the figures, for $d_{LT} = 2.5mm$, we revealed at $t = 0$ the small photopeak, followed by a second negative signal. We interpreted this signal as a first layer of quick

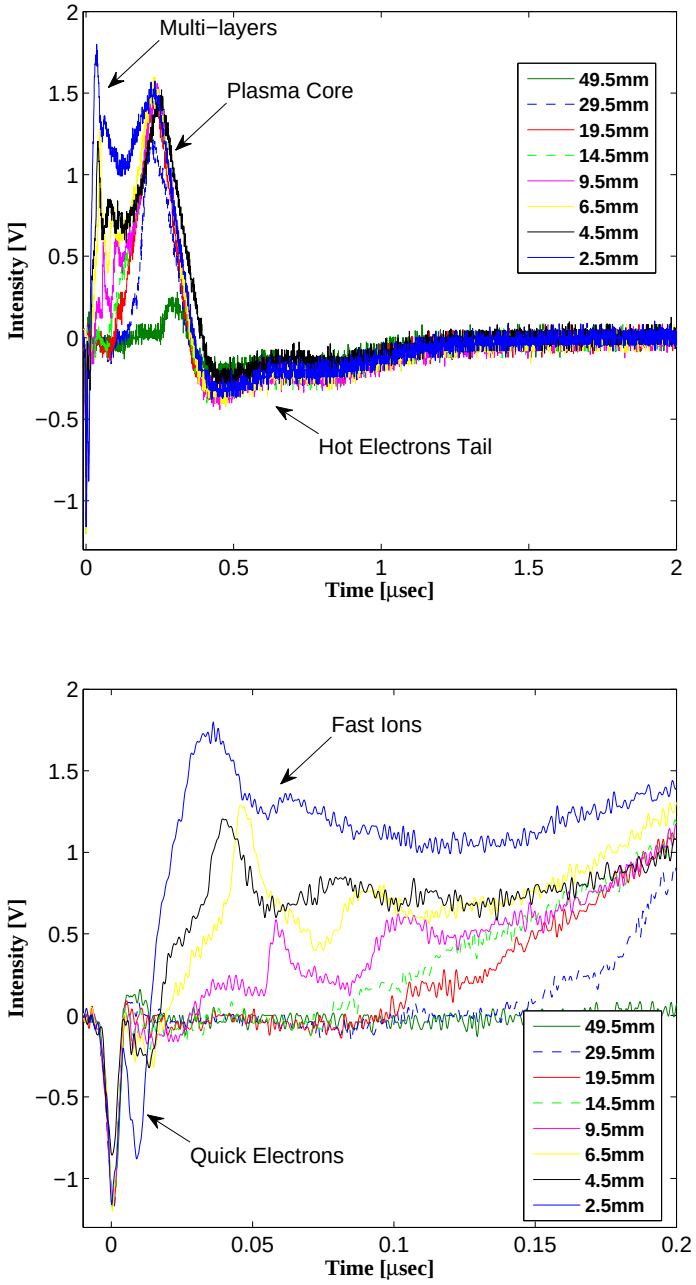

Figure 2.3.4: *Time of flight signals vs probe position for* $V_p = 0V$.

electrons, i.e, the first particles that escape from the target after laser-target interaction. The fast electron peak is then followed by some fine structures in the current signal which can be interpreted as several positive peaks. The absolute negative electron peak is observed only at $10ns$. The positive signals associated to the several peaks do not preclude that between two ion excess, a layer of slower electron might be located. After $150ns$, the bulk plasma expansion follows, with the expected dropping density decrease. At $400ns$, a hot electron tail, that expands later on, impacts on the probe. This dynamics is favoured also by the high three body recombination rate (see section 1.4.1), permitting to the hot electron to survive in the plasma at longer expansion times. The multi-peak are also detected for $d_{LT} = 4.5mm$ and $d_{LT} = 6.5mm$. At $d_{LT} = 14.5mm$ these layers disappears. This may be a consequence of the peculiar proprieties of the layers: if they are characterized by some excess of charges, they would be collected by the probe as a function of its geometrical cross-section, which in turn depends on the exposed solid angle (i.e on the distance). This means that at larger distances the transverse area of the probe would be too small to "see" the flighting particles and also explains why the fine structure of the TOF spectra are invisible with the FC.

The TOF signal trends were interpreted by taking into account that at the early stage of the plume formation, charge separation, i.e., formation of DL-Double Layers can occur (see section 1.8.1). We know that a single DL forms between a layer of electron excess and another layer characterized by an ion excess; here, self generated strong electric fields of several order of magnitude can develop. The intensity of these electric fields can be more than one order of magnitude higher than the Coulomb electric field

developed in the bulk plasma (up to $10^6 V/m$) as we will see in section 2.3.3.

The first $100ns$ of the plume expansion is therefore characterized by a multiplicity of ion bunches which were called *ML-Multi-Layers*, that compose the coronal part of the plume, reaching for first the probe. A similar effect was also observed, at lower laser fluence, by other authors that interpreted such dynamics in a similar way [34, 70]. Bulgakova et al., at fluences two order of magnitude lower, observed a partial fragmentation of the plume, which was ascribed to the DL formation. Therefore, according with the data and with the results reported in literature, this phenomena is particulary linked to the amount of energy deposited into the plasma. In the laser regime of this work it begins to assume some characteristics which are more typical of plasma generated by high laser intensity, where any hydrodynamical approach fails, and only the microscopic kinetics are valid.

In order to confirm that the detected multishells represented effectively quick electrons and fast ions and not maybe electric oscillations of the probe circuit, the same measurements were performed by biasing the probe with different voltages (this permitted in addition to reconstruct the $I-V$ curves). Figure 2.3.5 features the TOF signals versus the probe voltage from $-60V$ to $+50V$. The probe was located at $4.5mm$ from the target, where the tungsten tip is still sensitive to the multilayer structure. Looking to the trends of the same signals reported in a shorter time axis (down figure), one reveals that each fast peak is sensitive to the probe voltage, since the fast negative peak gradually decrease, as expected, by applying voltages from $+50V$ to $+2$ with steps of $10V$, $5V$ or $2V$ and the fast ion peaks decrease when the voltage is increased from $-60V$ to $-2V$ with the same voltage steps. The

signals hence definitively confirm that effectively fast electrons and ions are observed. The structures of figure 2.3.5, are similar to the ones shown in chapter 1 (figure 1.8.5). Although we could not perform measurements able to distinguish among the different charge states, we can reasonably conclude that the peaks observed in fig. 2.3.5 are similarly composed by ions with different charges. In this regime, the dynamics is strongly non-linear and the quasi neutrality of the plume can be violated (see section 1.8.1). The high laser fluence is then the principal *activator* of the ML structure.

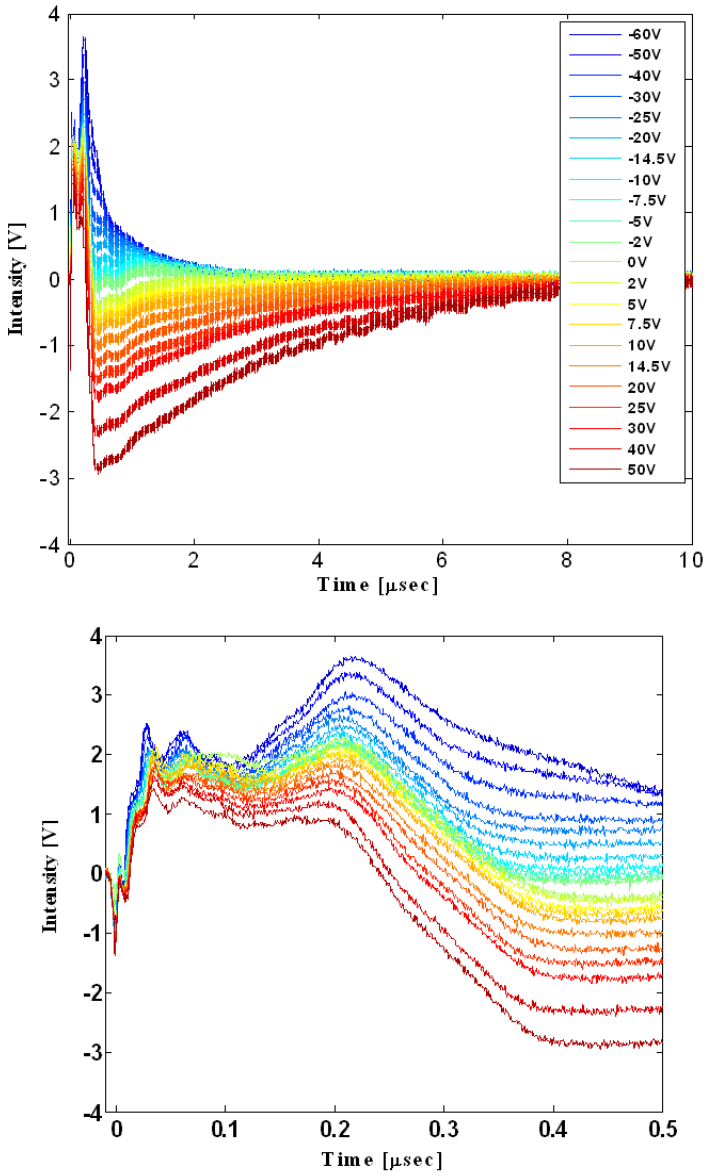

Figure 2.3.5: *Time of flight signals acquired for the different probe voltage when the LP was located @ 4.5mm from the target; in a larger time scale (up) and in a smaller time scale (down)*

2.3.2 Time resolved plume characterization in terms of electron density and electron temperature

Reporting the TOF signals 2.3.4 in terms of current values determined by the formula (2.2.1) at fixed time, and plotting the different $I(t)$ vs V (probe potential), we obtain the characteristic $I-V$ curves, shown in figure 2.3.6. By means of a Matlab® code developed on the purpose to analyze the current curves [65], we obtained the electron density, the electron temperature and the plasma potential by applying the Langmuir Probe theory described in section 1.11.1. Looking at figure 2.3.6, a first important consideration

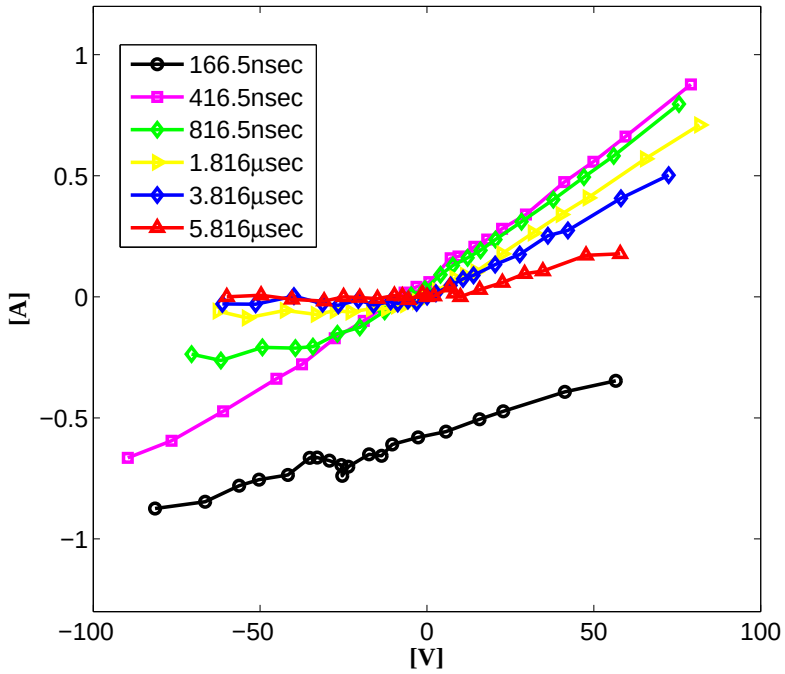

Figure 2.3.6: *I-V curves obtained when the probe was located @ 4.5mm from the target.*

must be done about the $I-V$ curve trends at the early stage of the plume formation: the current signal at $t = 166.5ns$ has a no expected trend, if compared to the curve reported in figure 1.11.2. This suggests a different plasma behaviour. Similarly, the curve at $t = 416.5ns$ looks like an ohmic curve following the law: $IR = V$. These trend suggests that in this region the plasma behaves like a usual conductor and the quasi-neutrality of the plume may be violated over lengths larger than λ_D. These trends can be related to the DLs formation discussed in the previous section[3]. In these cases the Langmuir theory no longer applies, and the curve cannot be analyzed, since the ion and the electron current doesn't show any saturation region or meniscus. At later time expansions (upon $500ns$), the $I-V$ curves becomes becomes analyzable. We obtained the electron density versus time reported in figure 2.3.7 for $d_{LT} = 4.5mm$ and for $d_{LT} = 14.5mm$. The electron density n_e was here determined by applying the OML-Orbital Motion Theory and using equation (1.11.7). As we can observe from the figure, we obtained densities on the order of $n_e = 1.5 \cdot 10^{18} m^{-3}$ in the first instants of the plasma core expansion, then decreasing of one order of magnitude after $t = 5\mu sec$, with the classical decreasing expansion trend [71]. However, the electron density also shows a not significant decrease the probe was moved from $d_{LT} = 4.5mm$ to $d_{LT} = 14.5mm$. Although the distance was almost triplicated, the density remained almost unchanged. This results contradict the well know decreasing trend of the plasma density predicted by the theoretical models [36] (see chapter 5). On this purpose we evaluated the

[3] the same trends were observed also when the probe was located at $14.5mm$ from the target, for which we don't report the I-V trends; this effect was not observed when the probe was located orthogonally to the plume expansion direction; we will discuss this aspect in section 2.3.4.

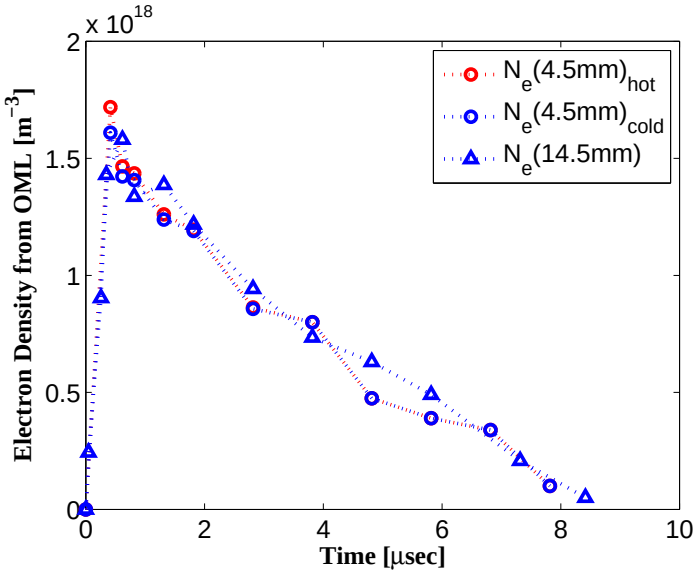

Figure 2.3.7: *Electron Densities vs time for* $d_{LT} = 4.5mm$ *and for* $d_{LT} = 14.5mm$.

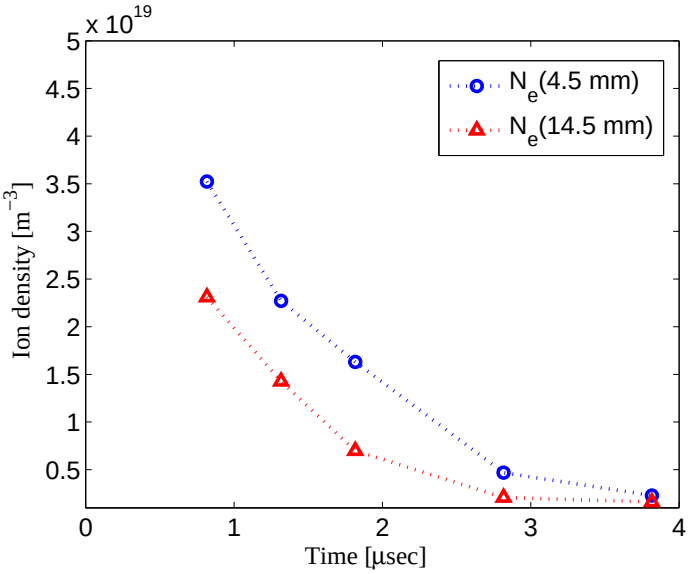

Figure 2.3.8: *Ion Density vs time for* $d_{LT} = 4.5mm$ *and for* $d_{LT} = 14.5mm$.

ion density from the ion saturation current, by using equation 1.11.5. The density values are reported in figure 2.3.8. I_i^S was evaluated at the different expansion times from the $I-V$ curves reported in 2.3.6. As we can observe from the figure, the ion current shows a more significant decrease of the density when the probe was moved from from $4.5mm$ to $14.5mm$. This could indicate that the electron density evaluated by the OML theory is less reliable than the values extracted from ion saturation current. This is not new in LP measurements; a large number of experimental results demonstrate that the electronic part of the $I-V$ curve is affected by problems related to the electron collection: it may be influenced by inner plasma magnetic field, high collisionality, plasma wave etc. However the no decrease of the electron density could also depend on the probe orientation as we will see in section 2.3.4.

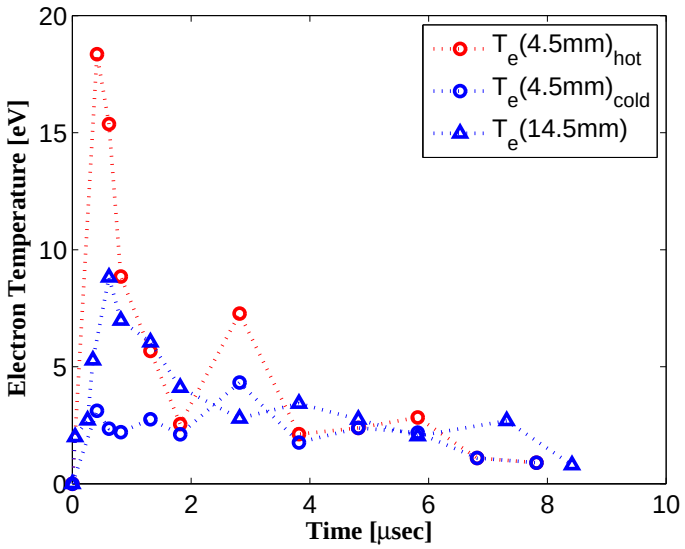

Figure 2.3.9: *Electron Temperatures vs time for* $d_{LT} = 4.5mm$ *and for* $d_{LT} = 14.5mm$.

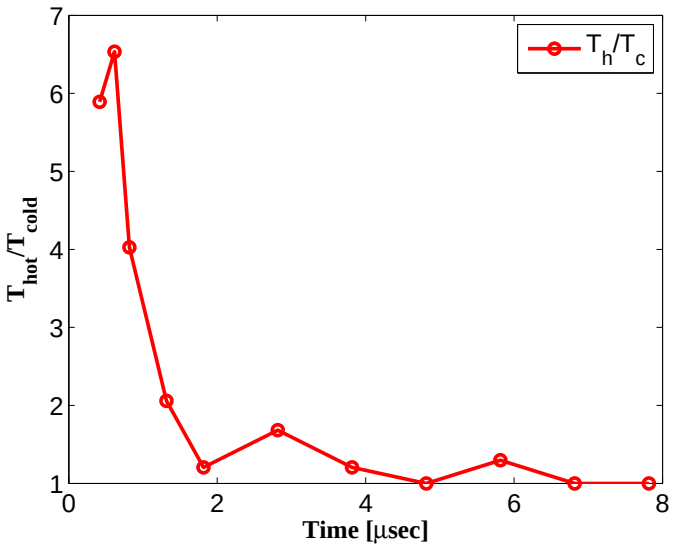

Figure 2.3.10: *Electron Temperatures Ratio vs time for* $d_{LT} = 4.5mm$.

In figure 2.3.9 the corresponding temperature trends are reported: A two plasma temperature, i.e a TET plasma was here revealed[4] for $d_{LT} = 4.5mm$ and a SET plasma for $d_{LT} = 14.5mm$ (for SET and TET plasmas definition see section 1.8.1). The TET plasma is due to the simultaneous presence of a hot (T_{hot}) and a cold electron plasma population (T_{cold}), that evolve separately, starting with a temperature difference of $\Delta T = 10eV$ in the first part of the LP acquisition, then decreasing to few eVs up to $4\mu s$. T_{hot} and T_{cold} become then comparable, because of the thermalization between the hot and the cold electrons component. Looking again at the TOF signals reported in figure 2.3.4 we observe that the Multi-Layer structure disappears for $d_{LT} = 14.5mm$, i.e when also the TET plasma disappears. This indicates that TET plasma is related to the DL formation, as confirmed in section

[4]in terms of $I - V$ curve analysis two different $I(V)$'s slopes are detected.

1.8.1, by the theoretical models. In this case we know that rarefaction of shock waves, that represents a DL, can occur. On this purpose, in figure 2.3.10 the ratio between the hot electron temperature and the cold electron temperature is reported. T_{hot}/T_{cold} assumes values between 5.8 and 6.5 in the first instants of the bulk plasma propagation, respectively at $t = 416ns$ and at $t = 616ns$, then decreasing to values between $2 < T_{hot}/T_{cold} < 4$ at $816ns < t < 1.316\mu sec$. At later expansion times $T_{hot}/T_{cold} \cong 1$. If a **multiple electron fluid** is supposed, rarefaction of shock wave is obtained for $T_{hot}/T_{cold} = 5.4$ [22]. This value is very close to the experimental one determined at $t = 416ns$, and it may explain also the Multy-Layer structure observed in figure 2.3.4.

Measurements put in evidence that TET plasma survives for long times if compared with the laser pulse duration (i.e. with the typical times of plasma formation). This can be favoured by the high recombination rate, that can occur during the bulk plasma propagation. On this purpose, in figure 2.3.11 the $T_e^{-9/2}$ and the $T_e^{-1/2}$ trends are reported, representing respectively the threebody recombination and the photo recombination rate. As we can observe from the figure, R_{ph} and R_{3b} becomes significant at later expansion times. This means that in case of R_{3b} the hot electrons can take part in threebody recombination as third particle so that they get additional energy and they can survive in the plasma for more time. The hot electrons tail is also visible in figure 2.3.4: it appears at $0.5\mu sec$ and determines also the trend of the electron signals of figure 2.3.5 that are much more broadened respect to the first ones because the probe voltage differs from zero.

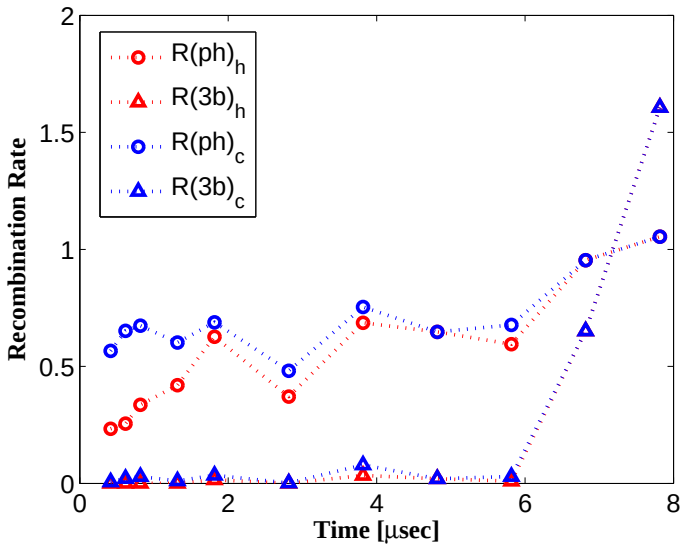

Figure 2.3.11: *Recombination Rate vs time for* $d_{LT} = 4.5mm$.

2.3.3 Evaluation of the self-generated plasma electric field

As mentioned before, from the $I-V$ curve analysis also the plasma potential versus time $V(t)_p$ can be calculated. As discussed in section 2.3.1, it is not strictly the plasma potential like in case of stationary plasmas, but more an ambipolar potential which arises to equalize the flows of ions and electrons into vacuum during the plasma expansion. By dividing $V(t)_p$ by the Debye length $\lambda(t)_D$ calculated from the measured n_e and T_e reported in previous sectio by means of equation 1.2.3, the electric field of the bulk plasma vs time is obtained. The plasma potential and the Debye length (on the order of $10^{-6}m$ during the overall plume propagation), are reported in figure 2.3.12 calculated both at $d_{LT} = 4.5mm$. The plasma potential of the hot electrons component is, at the early stage of the bulk plasma propagation, very high; then it decreases, approaching to the cold electron plasma potential values

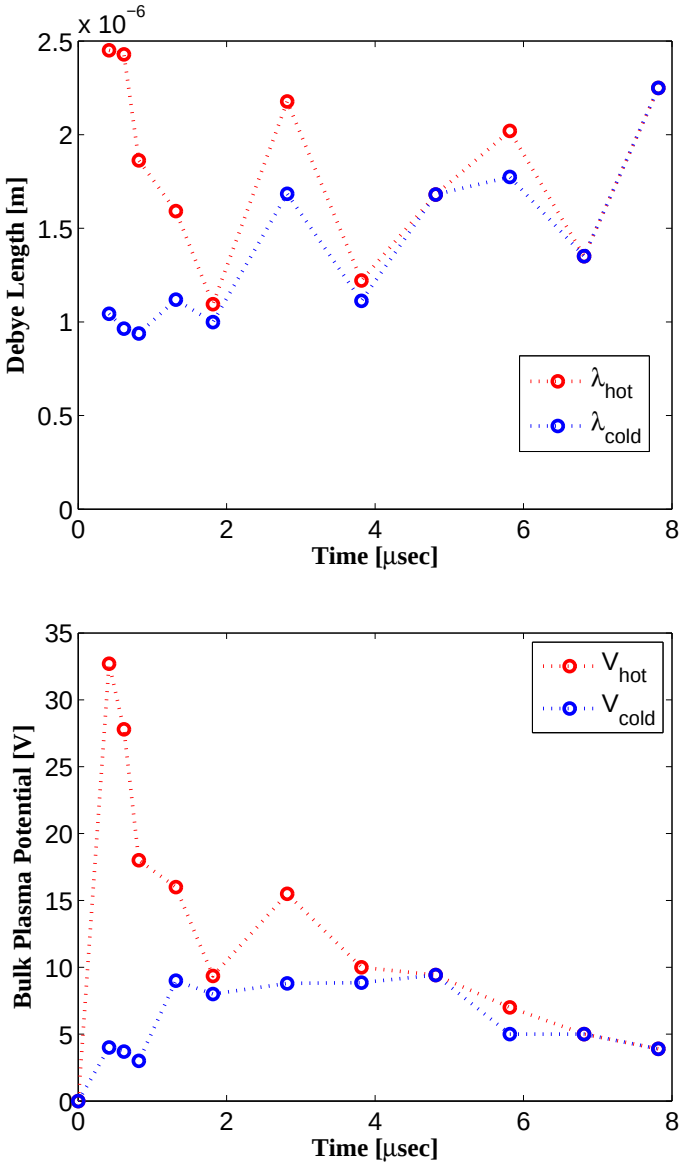

Figure 2.3.12: *Debye Length and Plasma Potential vs time for* $d_{LT} = 4.5mm$.

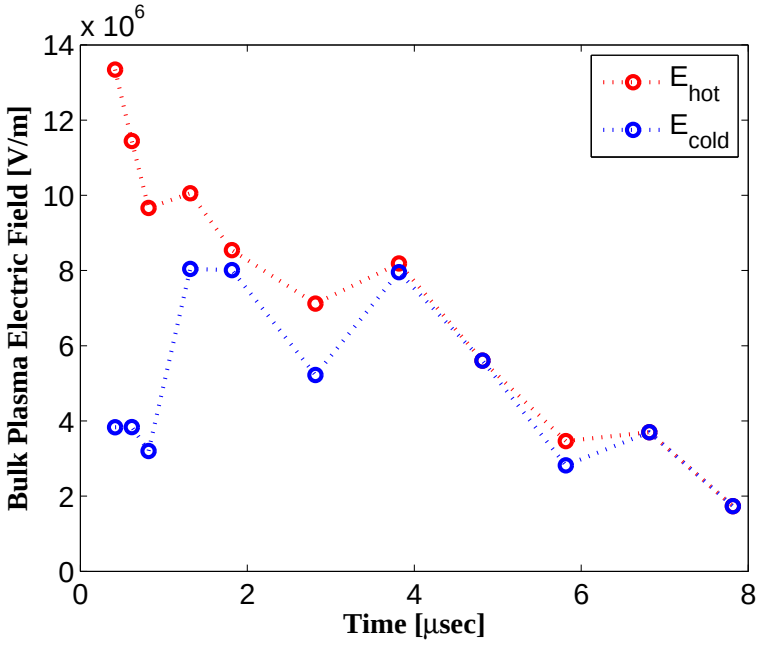

Figure 2.3.13: *Electric Field vs time for* $d_{LT} = 4.5mm$.

V_{cold} at $4\mu s$. The high plasma potential values over the debye length values at corresponding times, determines the electric field reported in figure 2.3.13. As we can observe from the figure, the electric field assumes values on the order of $1.4 \cdot 10^7 V/m$ for the hot electrons and of $4 \cdot 10^6 V/m$ for the cold electrons at the early stages of the LP acquisition (at $t = 416ns$), then decreasing both to $2 \cdot 10^6 V/m$ at $t = 6\mu sec$.

The electric field E_{DL} developing during the multi-layers evolution was evaluated numerically in collaboration with Mascali et al. in [72], with a numerical model that is under development. This model is based on the hypothesis that ion and electron bunches can be treated like adimensional slabs carrying a charge respectively of Q_1, Q_2 and q of total charge then moving like a mass spring damper (see figure 2.3.14).

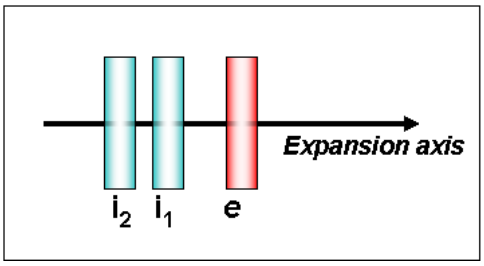

Figure 2.3.14: *Sketch showing the electron slab and the two ion slabs simulated with the theoretical model.*

The electron and ion bunches can be described with the following equations:

$$\begin{aligned}
\frac{dv_{i1}}{dt} &= \frac{Q_1}{M_1}\frac{q}{4\pi\epsilon_0}\frac{1}{\mid x_e - x_{i1} \mid^2} - \frac{Q_1 Q_2}{M_1}\frac{1}{4\pi\epsilon_0}\frac{1}{\mid x_{i2} - x_{i1} \mid^2} \\
\frac{dv_{i2}}{dt} &= \frac{Q_2}{M_2}\frac{q}{4\pi\epsilon_0}\frac{1}{\mid x_e - x_{i2} \mid^2} + \frac{Q_1 Q_2}{M_2}\frac{1}{4\pi\epsilon_0}\frac{1}{\mid x_{i2} - x_{i1} \mid^2} \\
\frac{dv_e}{dt} &= \frac{q}{m}\frac{Q_1}{4\pi\epsilon_0}\frac{1}{\mid x_{i1} - x_e \mid^2} + \frac{qQ_2}{m}\frac{1}{4\pi\epsilon_0}\frac{1}{\mid x_{i2} - x_e \mid^2}
\end{aligned} \tag{2.3.1}$$

where v_1, v_2 and v_e are the velocities of the first and the second ion bunch and of the electrons respectively, x_1, x_2 and x_e denote the time-variable positions of each layer and finally M_1, M_2, m are their respective masses. Equations 2.3.1 where then solved numerically with a 4° and 5° order Runge-Kutta Nystrm method in Matlab®. We obtained the evolution of the energy for the first and the second positive peaks which was then compared with the experimental data. Results are reported in figure 2.3.15. It is important to underline that although the oversemplification of the model, the order of magnitude of the first peak energy after the end of the acceleration was approximately reproduced. However, in order to find this high value of energy without any appreciable deceleration of the escaping electrons, we had to assume in the code that the first peak was accelerated by the second

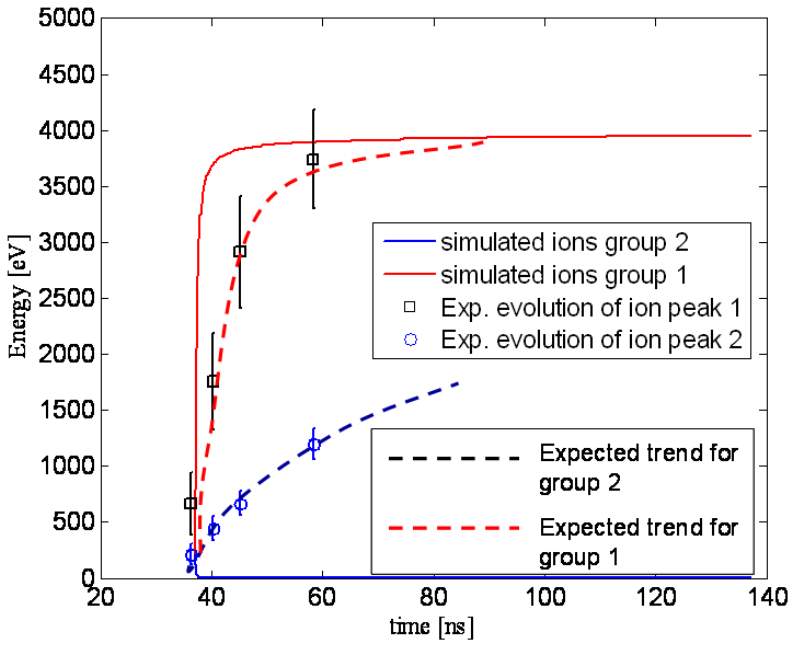

Figure 2.3.15: *Theoretical calculation of the equivalent field acting on the accelerated ion bunch*

one (therefore coulomb repulsion among the positive bunches), rather than dragged by the escaping negative layer made of electrons. In fact, it can be seen in the figure that the energy of the second peak drops and becomes almost zero. This is where the model fails: the simulation results demonstrate that there are more than two positive peaks and that some negative layers must appear between them, forming a sort of *sandwich structure*. This additional layers should be able to partially screen the repulsive force (thus decreasing the velocity gain gain of the first peak that is much larger than the experimental one), and to accelerate the second positive peak. The calculated electric field which govern the acceleration versus time is reported in

figure 2.3.16. First numerical calculations shows that the electric field has

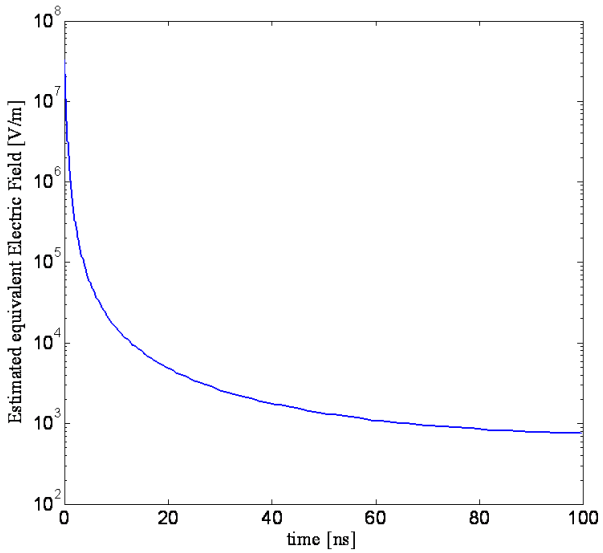

Figure 2.3.16: *Theoretical calculation of the equivalent field acting on the accelerated ion bunch.*

a maximum value on the order of $3 \cdot 10^7 V/m$, i.e double of the ambipolar potential associated to the hot electrons in the bulk plasma. The electric field evaluation helped us to better understand the early stage plume dynamics: the plasma potential developing in the DLs produces in the plasma core an accelerating field which accelerate the ions and splits the different charge states. The splitting produces bunches separated by $\sim 10\lambda_D$ [22] and the electrons diffuse in the inter-bunches space accelerating also the lower charge state bunches. Therefore a plurality of charged layers is formed, that approach to each other during the propagation of the bulk plasma. Further investigations are needed on the purpose to fully understand the total evolution of the plasma.

2.3.4 Charge collection dynamics on the probe surface

By comparing the plasma parameters obtained in the two experimental configurations we can deduce some important aspects of the plume dynamics in terms of charge collection on the probe surface. As mentioned before, in the experimental configuration (a) the LP measurements were performed at $d_{LT} = 15.3mm$ on axis and at $d_{LT} = 33.7mm$ off axis. The $I - V$ curves obtained for $d_{LT} = 15.3mm$ are reported in figure 2.3.17. As we can observe from the figure, the curves have a more similar trend to the expected $I - V$ curve reported in figure 1.11.2, especially at the early stage of the plume expansion, compared to the current curves obtained in the parallel configuration. The corresponding electron density and temperature values vs time for both positions, are reported in figure 2.3.18 (obtained with the same method described in section 2.3.2). We observe that at $d_{LT} = 33.7mm$, n_e decreases more than half with respect to the n_e values obtained at $d_{LT} = 15.3mm$. A similar trend is also observed for the temperatures[5]. At expansion times up to $3\mu s$, the two temperatures become comparable. This occurs probably because the plume decays into free streaming (see section 1.8.3) and the core plasma temperature becomes comparable to the edge plasma temperature. We also observe that the n_e values obtained at $d_{LT} = 15.3mm$ are quite comparable to the n_e values obtained at $d_{LT} = 14.5mm$, when the probe was located parallel to the expansion direction. This is expected because the two probe position are also comparable and are both on axis. On this purpose let us return to those density values: as we reported in section 2.3.2, we didn't observed a significant decrease of n_e by moving the probe from

[5] a hot component at the early stage of the plasma signal acquisition for $d_{LT} = 15.3mm$ is also detected that however disappears quite soon, because of the large d_{LT}.

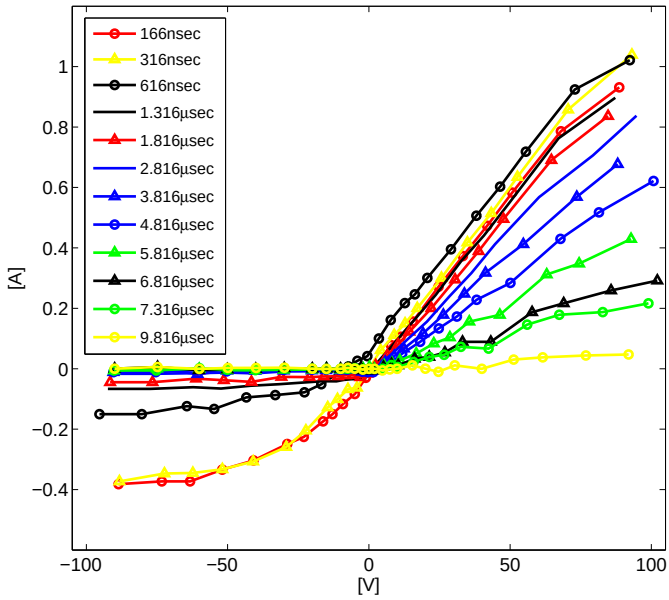

Figure 2.3.17: *$I-V$ curves obtained when the probe was located orthogonally to the plume expansion direction at* $15mm$ *from the target.*

$d_{LT}(\|) = 4.5mm$ to $d_{LT}(\|) = 14.5mm$. This comes out because the electric signal has a no significant decrease, in terms of intensity, by moving the probe at larger d_{LT}s. In figure 2.3.19, the TOF signals obtained when the probe was biased at $+20V$ vs $d_{LT}(\|)$ are reported. As we can observe from the figure, the electric signal begins to decrease only for $d_{LT}(\|) = 49.5mm$[6]. On the contrary, when the probe is placed orthogonally to the plume expansion direction, a consistent decrease of the TOF signals from the on axis position to the off axis position was observed, determining the density trends reported in figure 2.3.18. The physical reasons of such trends can

[6]the same trend are also observed for the TOF signals obtained with positive biased and unbiased probe.

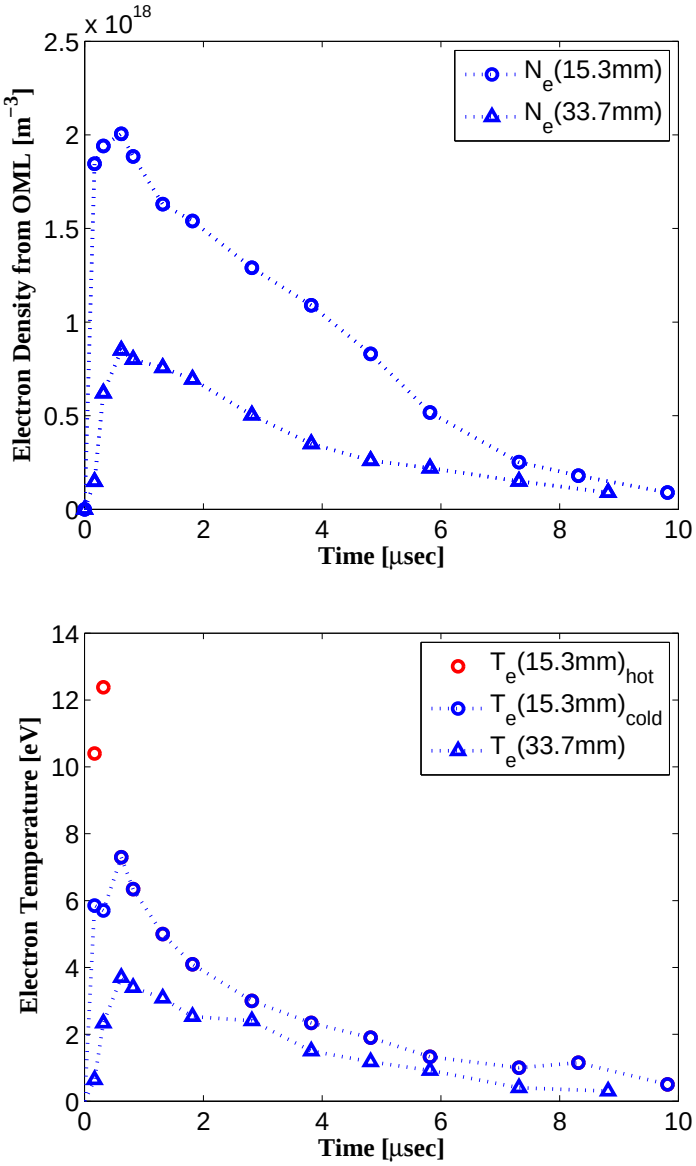

Figure 2.3.18: *Electron Densities and Electron Temperature vs time @ 4.5mm and 45mm from the target.*

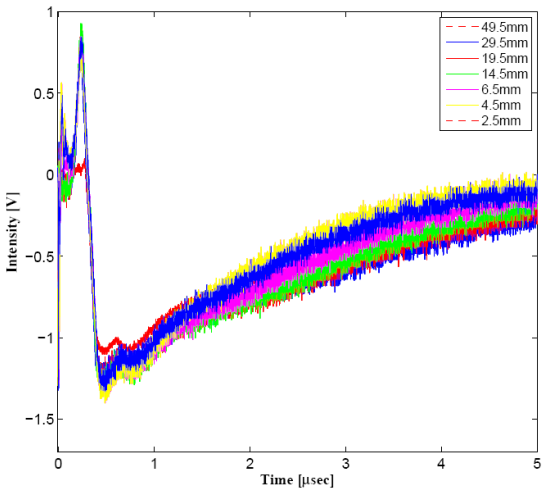

Figure 2.3.19: *TOF signal vs probe position for* $V_{pr} = 20V$*. To observe the begin of the decrease of the electron signal we need to move the probe up to* $d(\|) = 49.5mm$ *from the target.*

be different; first of all, by moving the probe from $d_{LT}(\perp) = 15.4mm$ to $d_{LT}(\perp) = 33.7mm$ a variation of n_e is expected, since in the first case n_e is determined on axis and in the second case it is calculated off-axis, i.e. in the periphery region of the plume, were the density is much lower. On the other hand, the no density decrease can be due to the strong forward peaked distribution of the plume: as we will see in chapter 5, numerical simulations demonstrate that the forward on axis plasma density distribution decreases more slowly respect to that one evolving with the lateral expansion of the plume. The probe hence needs to be moved at high enough distance from the target, in order to detect the periphery region of the plume, where the density decreases consistently as seen in figure 2.3.18. The same effect was observed also in [65], on a Ta plasma, where the time resolved n_e and T_e

trends obtained by placing the probe orthogonally to the plume expansion direction for $d_{LT} = 15mm$ on axis and for $d_{LT} = 30mm$ off axis decreases consistently by evaluating the density from the on axis to the off-axis position. The non consistent decrease of density when moving the away the probe "on-axis" cannot be exhaustively explained so far. Other authors gave a plausible explanation by considering the different way of charge collection on the probe; by placing the probe parallel to the target surface the ion signal did no saturate [73] pointing out that the when the probe is located parallel to the plasma flow the charge collection on its surface evolves in a complicated manner. Anyway the same conclusions cannot be apply to explain the results at different positions. More experimental investigations are needed to fully understand which of the effects described above prevails. The same measurements realized in 2.3.1 must be repeated in the orthogonal configuration, to verify if also in this case the probe signal decreases only after a certain distance from the target surface. If this occurs the hypothesis of a forward peaked density distribution is confirmed. If, instead, a consistent decrease of the current signal will be observed, a different way of charge collection on the probe surface depending on the probe orientation respect to the plume expansion direction is probably the physical explanation to the signals reported in figure 2.3.19.

2.3.5 Investigation of the plasma structure at different background pressures

The same measurements realized in 2.3.1, were performed at different background pressures, namely $10^{-3}mbar$, $10^{-2}mbar$, $10^{-1}mbar$, $1mbar$, $63mbar$. We also reconstructed the $I-V$ curves by placing the probe at $4.5mm$ from

the target for an operating pressure of $10^{-3}mbar$. The obtained plasma parameters were then compared with those ones obtained in vacuum. In figure 2.3.20 the TOF signals at different background pressures are reported, when the probe was located at $4.5mm$ from the target. As we can observe from the figure, three different pressure regimes are detected. A vacuum like regime corresponding to the signal revealed at $10^{-5}mbar$, the regime between $10^{-3} - 10^{-2}mbar$, where the ion component of TOF signals increase in intensity significantly, and finally the regime $10^{-1} - 1mbar$ where the signal strongly decreases. Three pressure regime where detected also by

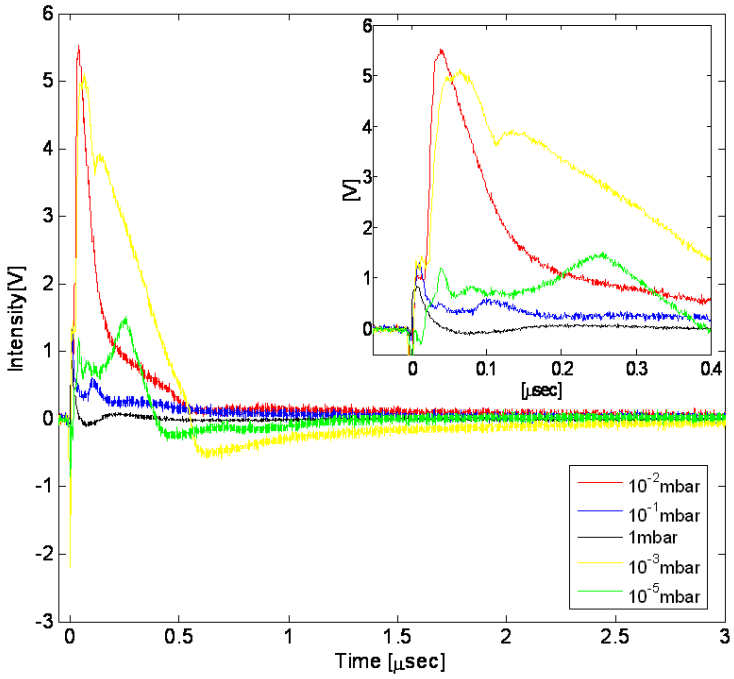

Figure 2.3.20: *TOF signals vs time at different background pressure for* $d_{LT} = 4.5mm$.

Amoruso et al. in [74]; they detected a vacuum like regime until $10^{-2}mbar$, observing the plume splitting (see section 1.9) at 10^{-1mbar} and finally an exponentially decrease of the signal for higher pressures. In their experimental set-up the probe was placed at $75mm$ from the target and biased at $-10V$ and the laser fluence was of $2.5J/cm^2$, much lower with respect to our one (on the order of $2000J/cm^2$). Similar trends to those reported in figure 2.3.20 were observed even by placing the probe at $d = 50mm$ from the target, i.e, the signals at $10^{-2} - 10^{-3}mbar$ where more intense with respect to the signal observed in the vacuum like regime. This can be attributed to several physical reasons: large TOF signals intensities suggest a plume compression, caused from the background gas, i.e., the plasma is confined and higher densities are reached for distances closer to the target surface. However, this dynamics has been not observed for the electrons, that show the same signals intensity of the vacuum like regime also at $10^{-3} - 10^{-2}mbar$. The second reason can be attributed to a shock wave which generates close to the contact surface between the plasma and the background gas (see section 1.9). On this purpose further investigations are needed. The third reasons is attributed to the fact that TOF signals recorded in background gas are influenced by the coupling between the fast layers, detected in vacuum. On this purpose let us look at the signal reported in figures 2.3.21 where the TOF trends at $10^{-3}mbar$ and at $10^{-2}mbar$ vs probe position are shown. When a background gas acts on the plasma expansion the multy-layers gets spatially closer to each other. The viscous force acting on the expanding fast electrons and the fast positive peaks causes an increase of the self-generated electric field. Under this condition, some of the bunches can be fused and some *clusterization* of the bunches occurs. This generate clustering within

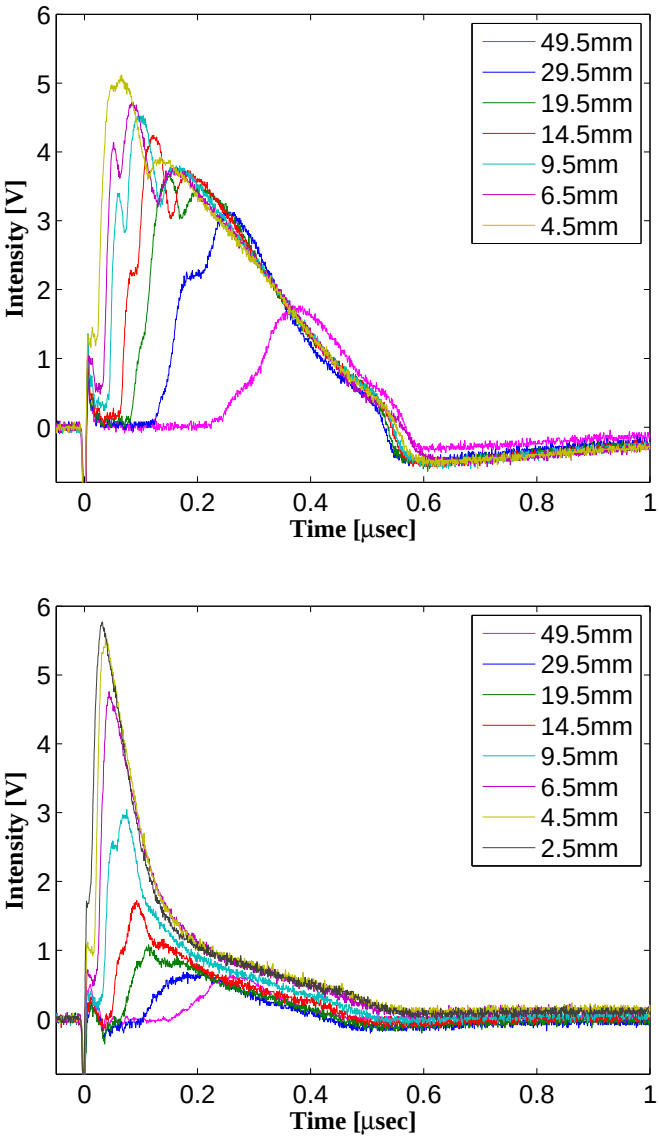

Figure 2.3.21: *TOF signal at* 10^{-3}*mbar (left) and at* 10^{-2}*mbar (right) vs probe position for* $V = 0$.

the different ion charge state groups that hence evolves like a unique group for pressure on the order of $10^{-2}mbar$ or in two different group for pressures of $10^{-3}mbar$. Despite the fact that the signal are not attenuated, they have also a very fast temporal evolution. This probably occurs because the fast component is statistically attenuated only with distance, since it penetrate the background gas with no significant collisions. We observe at $10^{-3}mbar$ three different positive peaks that disappear with distance, suggesting the plume splitting in a fast and a slower ion component. At $10^{-2}mbar$, only one peak is detected, probably because plasma particles undergo to more collisions, so that the different ion groups thermalize faster. At $10^{-3}mbar$ also the $I - V$ curves were obtained; in figure 2.3.22 the comparison between n_e and T_e obtained at $10^{-3}mbar$ and n_e and T_e obtained in vacuum, when $d_{LT} = 4.5mm$, are shown. As we can see from the figure, the electron density in vacuum is $20 - 30\%$ lower than n_e measured in the background gas. This occurs again because the gas acts as a viscous medium which partially decrease the expansion velocity, thus generating a sort of stagnation and plasma compression. The temperature trends finally show that, at $10^{-3}mbar$, the hot component and the cold component have quite similar temperatures overall the plume expansion. This occurs because the collisional regime between the plasma particles and the background gas causes a rapid thermalization between T_{hot} and T_{cold}.

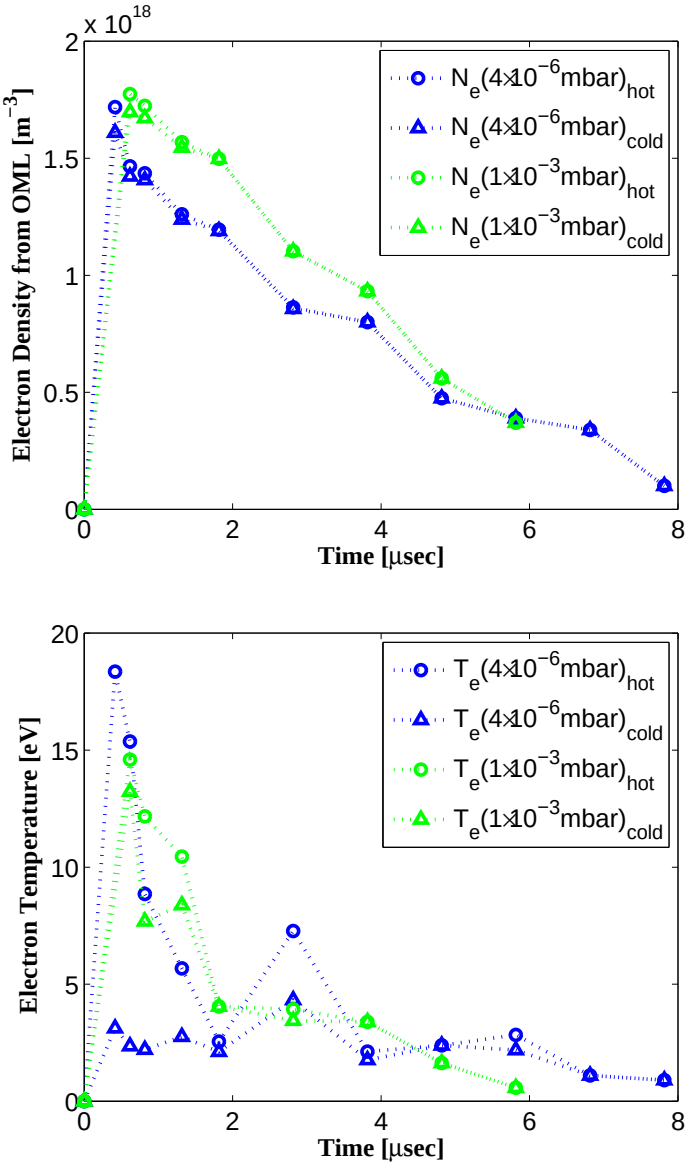

Figure 2.3.22: *Electron Densities and Electron Temperatures vs time @* $4 \cdot 10^{-6} mb$ *and @* $1 \cdot 10^{-3} mb$ *@* $4.5 mm$ *from the target.*

2.4 Conclusions

The investigation of the plasma structure, by means of the LP TOF signals, permitted us to understand more in detail the plume expansion mechanism. Our experimental set-ups permitted us to locate the LP very close to the target surface. We hence detected the Multi-Layers which appear quite interesting to be further studied at this fluence regime.

A final draft of the plume dynamics is reported in figure 2.4.1, that can be explained as follows:

1. After the laser pulse ends, the fast electrons are the first charged particles that escape from the target.

2. The ion blow-off occurs; the fast electrons split the initial positively charged ion bunch into different, but still positive, sub-bunches (higher charge states move more rapidly). Because of the charge repulsion, the first bunches are strongly accelerated forward by the less rapid ones.

3. When the splitting produces bunches separated by $10 \simeq \lambda_D$, electrons diffuse in the inter-bunches space accelerating also the lower charge state bunches. Therefore a plurality of charged layers is formed.

4. The evolution of the bulk plasma follows after $100ns$ of fast particles propagation.

The electron and ion bunches evolves in a uncoupled manner with respect to the plasma core.

The ratio T_{hot}/T_{cold} indicates the that rarefaction of shock wave can be generated. In any case, simulation on bunches dynamics reveal that the peaks could be accelerated by repulsive among positive peaks, more than

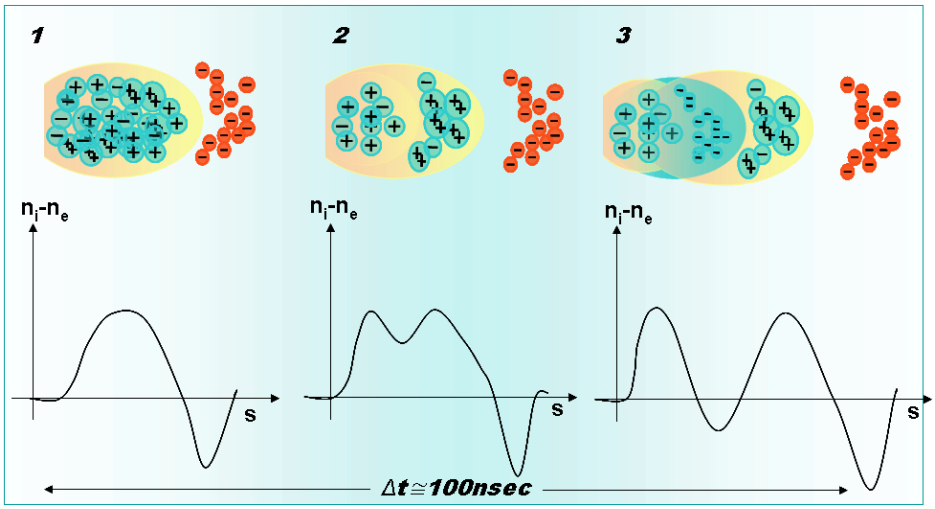

Figure 2.4.1: *Temporal Scheme of Plasma Plume Dynamics*

by attraction caused by the escaping electrons. Maybe DL plays a role only at the beginning, when electrons and positive layers split each other. Both E_{DL} and E_{bulk} were calculated and they are of the same order of magnitude at the early stages of both Multy-Layer and plasma core expansion, i.e. $E_{DL} = 3 \cdot 10^7 V/m$ and $E_{bulk} = 1.4 \cdot 10^7 V/m$ as maximum values. The numerical model used to calculated E_{DL} permitted us to simulate also the energies of the first electron bunches and of the two following ion bunches.

Chapter 3

Investigation of Colliding laser produced plasmas

In this chapter the measurements realized with colliding plasmas will be presented.

3.1 Introduction

In section 1.10 of chapter 1, we reported aims and experimental tools used for colliding plasmas characterization. In this chapter experimental results are presented, which were obtained by combining time and spatially resolved spectroscopy and Langmuir Probe measurements, from Al colliding plumes generated with a Nd:Yag laser with similar characteristics and comparable irradiances[1] to those used in chapter 2. At these laser energies colliding plasmas tends to *stagnate*, and they do not show a significant interpenetration, since $\xi \gg 1$ (see section 1.10). The experiments described here were

[1] $3.2 \cdot 10^{11} W/cm^2$, or in terms of laser fluence: $1.9 \cdot 10^3 J/cm^2$

Figure 3.2.1: *Picture of the DCU-Laboratory* .

performed at DCU-Dublin City University, in collaboration with Prof. J. Costello, of the School of Physical Sciences and the NCPST (National Centre of Plasma Science and Technology). The data were acquired during a period of six months from March 2010 to September 2010. For this reason much of the analysis is still in progress and, as such, only the preliminary experimental results will be presented in this thesis.

3.2 Experimental set-up

The experimental apparatus used in this work was recently implemented by P. Hough et al.; a detailed discussion of the experimental set-up is given in [39]. The target set-up used to obtain the plume collision was a *flat configuration* (see figure 1.10.1). This set-up was chosen due to the simple arrangement, which avoids the alignment challenges encountered when, for example, angled targets are used. Moreover fresh target material for ablation can easily be obtained via a 2-dimension stage vacuum compati-

ble motors. All measurements were obtained by employing 99.99% pure Al targets. With the same experimental set-up measurements on thin Al foils were also recorded, and will be discussed separately in chapter 4. The DCU laboratory used for this work is shown in figure 3.2.1.

3.2.1 The vacuum chamber

The vacuum chamber used was design and commissioning is reported in [39]. It consists of a stainless steel cylindrical chamber ($40cm$ of diameter and $30mm$ of high). Several different type of flanges encompass the chamber coupled at different angles. The chamber is mounted on thigh tensile strength aluminium profiles and aligned to an optical table, where the laser and optical components are located (see figure 3.2.1). The vacuum system

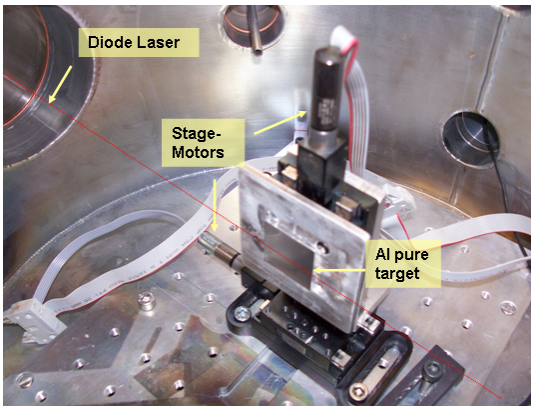

Figure 3.2.2: *Motorized target holder for the Al target, aligned by means of a red diode Laser.*

consists of a Leybold Turbovac turbo-molecular pump, backed an oil sealed rotary pump. All measurements were performed in vacuum, with an operating pressure of $1 \cdot 10^{-6} mbar$. Located inside the chamber is a motorized tar-

get holder, consisting of two Thorlabs vacuum compatible translation stage motors, each giving a minimum linear movement of $100\mu m$, and maximum linear movement of $25mm$ in both the horizontal and vertical directions. A custom designed flange, with wire feedthroughs, allows control of the motors movement under vacuum conditions. The target system is positioned at the centre of the chamber, defined by an alignment laser, as shown in figure 3.2.2.

3.2.2 The Surelite Laser System

The laser used for the experiment is a Surelite III-10 Laser system. It operates at its fundamental wavelength of $1064nm$ and emission is in pulsed mode with a maximum energy per pulse of $800mJ$ with a FWHM of $6ns$. The maximum repetition rate is $10Hz$. The laser beam is Gaussian (measured by fast diode traces) with a diameter of $7-9mm$ and a divergence of $0.6mrad$. A schematic picture of the laser is shown in figure 3.2.3. The laser was operated in external trigger mode to allow precise synchronisation, (the timing will be discussed in detail in section 3.2.5). The plasma was focal-

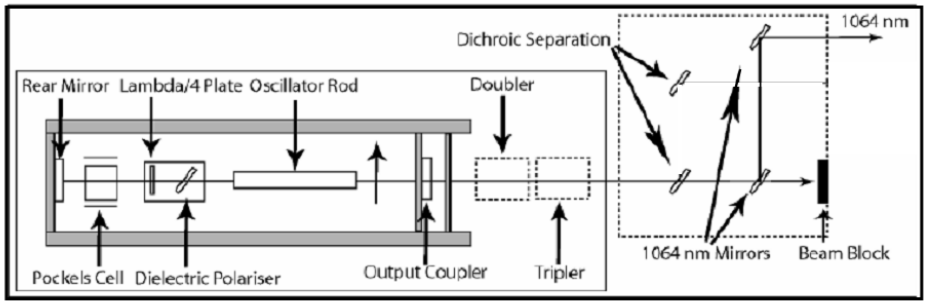

Figure 3.2.3: *Schematic Diagram of the Laser Surelite system.*

ized on the target through an anti-reflection coated plano-convex lens with a focal length of $f = 300mm$ and a diameter of $25.4mm$, obtaining focussed spot sizes at the target surface on the order of $100\mu m$.

The double plume configuration was obtained by using an acute $\gamma = 1^{\circ}$ wedge prism, which splits the laser beam into two separate beams, subsequently focused on the target by means of the lens described above. The distance between the focal spots was $D = 2.6mm$ and can be determined by:

$$D = f\gamma(n-1) \tag{3.2.1}$$

where $n = 1.5$ is the refractive index of lens. Each separate beam after the wedge contained $300mJ$ of laser pulse energy (the wedge prism bisected equally the path of the initial $600mJ$ laser beam). Using a power meter, it was verified that the wedge divided the laser energy equally for both the beams impinging on the target and producing the seed plasmas. However, slight energy differences between the seeds are possible within the experimental errors (on the order of of about the 5%). The optical scheme to produce both laser pulses for the seed plasmas is shown in figure 3.2.4.

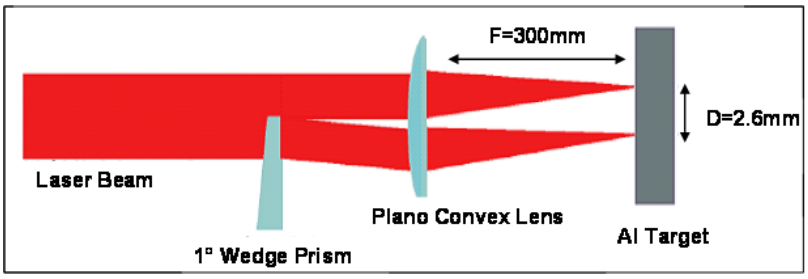

Figure 3.2.4: *Schematic diagram of the laser beam splitting by means of a wedge prism.* .

3.2.3 The Imaging system

Fast imaging was implemented in order to follow the plasma dynamics along the forward expansion axis.

In this work, the imaging system was spatially, spectrally and temporally resolved, achieved by employing a gatable Andor Intensified Charge Coupled Device (ICCD), model $DH534$. The camera consists of a 1024×1024 pixel array with a corresponding individual pixel area of $13mm \times 13mm$, yielding to an active area of $12.3mm \times 12.3mm$.

ICCD's have a high temporal response, on the order of few ns and consist of three principal components: a Photocatode, a MCP-Micro Channel Plate and a Phosphor Screen. An incoming photon strikes the photocathode and releases an electron, which is then drawn to the MCP across a small path ($\sim 0.15mm$) by a $150 - 200V$ electric potential. This photoelectron is further accelerated by a larger potential of about $500 - 1000V$. While traversing the MCP channel the electron collides with the walls of the capillary and creates secondary electrons, which subsequently release more electrons during subsequent collisions with the walls[2]. The resulting electron avalanche determines an amplification of the electric signal up to 10^4. At the MCP exit, the avalanche is swept across another small gap ($\sim 0.5mm$) by a large potential ($\sim 6000V$), which keeps the electron bunch tightly packed together and adds energy to the cloud, before it strikes the phosphor screen and creates an image.

The resulting image on the phosphor screen is directly coupled to the

[2]Varying the voltage across the MCP provides control over the number of secondary electrons that are released from the walls of the capillary and hence the gain of the system. This enables the camera to operate at very low light levels.

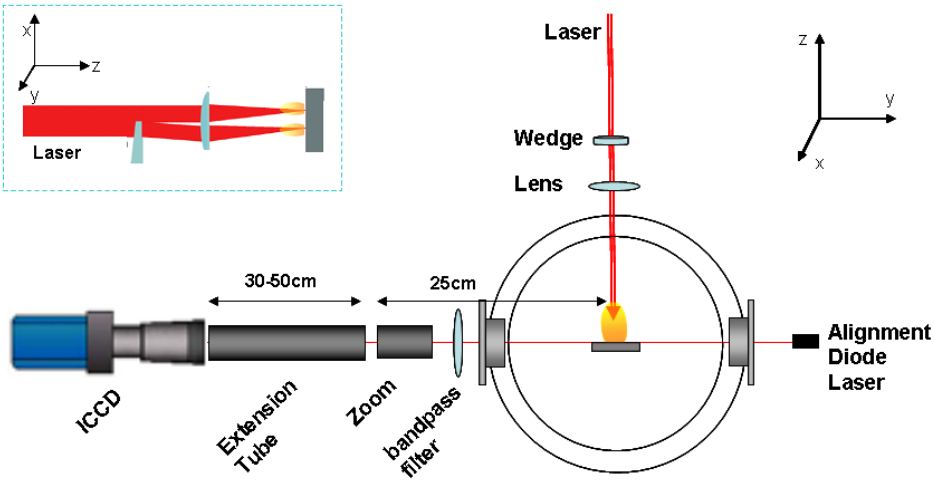

Figure 3.2.5: *Schematic of the experimental set-up for fast imaging of LPPs.*

CCD chip by a fibre optic coupler.

The fast imaging setup is shown schematically in figure 3.2.5 along with the main dimensions. As evident in fig 3.2.5, a Pentax zoom lens is used in conjunction with ICCD camera, to obtain a higher spatial resolution. Since the zoom lens could not be placed inside the vacuum chamber, the closest achievable distance from the zoom lens to the plasma (*object distance*) was $\simeq 250mm$. In order to achieve high magnifications ($\simeq 2X$) an extension tube of ($500mm$ long) was used to increase the distance between the zoom lens and the camera entrance aperture [3].

To calibrate the magnification of the optical system a ruler was inserted in the plane orthogonal to the forward plasma expansion direction. The zoom lens was then adjusted until the image of the ruler was focused on the CCD chip, observing the image on to the computer. Using the image of the ruler and knowing the physical size of each pixel it was possible to

[3] Without the zoom lens, the optical system would demagnify the image of the plasma.

determine the magnification of the system: for the images presented here a magnification of $1.62X$ was determined.

Between the imaging lens system and the vacuum chamber narrow bandpass filters where inserted in order to obtain high spectral resolution. This permitted the isolation of a particular transition or band of close lying transition in a neutral atom or ion. Only radiation emitted from atom transitions, with a wavelength within the bandwidth of the filter, reached the detector and so the spatial evolution of individual atoms or ions (in a particular excitation state) could be tracked over time. In the experiments, two narrow bandpass filters were used to select isolated line emission from neutral Al atoms and singly charged Al ions. The first filter was centred at $390nm$ with FWHM of $10nm$, with a transmission efficiency $\sim 40\%$. The second filter was centered at $460nm$ with FWHM of $10nm$ having a transmission efficiency of $\sim 60\%$. To observe the entire bulk plasma radiation emission a broadband short pass interference filter was employed. It transmits all radiation with wavelengths between $300nm$ and $950nm$, in order to protect the ICCD from any scattered laser radiation. A picture of the experimental set-up for fast imaging is shown in figure 3.2.6.

3.2.4 The Optical Spectroscopy system

Fast gated emission imaging is a simple and effective way to determine the whole plume spatial distribution and to extract its expansion velocity; however it cannot be used to determine other important plasma parameters such as electron temperature and density. One tool which can yield this information is the optical spectroscopy. In this work, the Emission Imaging Spectroscopy System was based on a spectroscopic technique introduced by

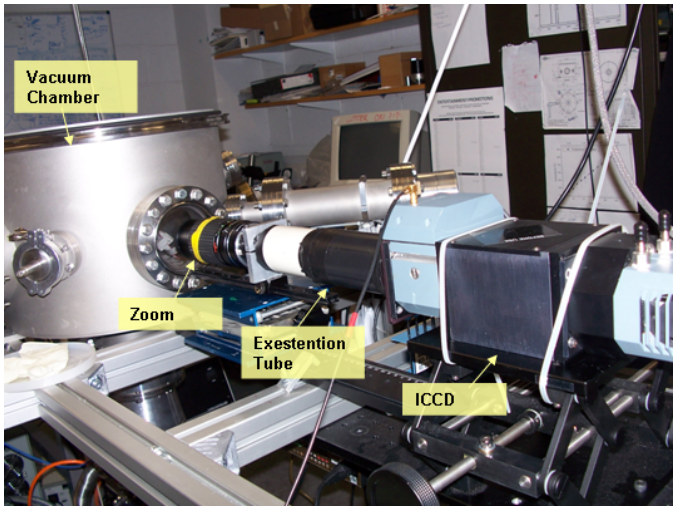

Figure 3.2.6: *Picture of the fast imaging set-up.*

Siegel et al. in [75]. The emitting plasma is imaged on the entrance slit of a Czerny-Turner spectrograph; at its output the spectrograph produces a one dimensional spatial and spectral image of the plume, in which the vertical axis corresponds to the expansion direction z and the horizontal axis refers to the wavelength λ of the emission. At the output of the spectrograph, in the image plane, a gateble ICCD is located. In this way, it is possible to obtain contemporary the spectral and spatial information of the plume propagation; while the temporal evolution is obtained by gating the ICCD camera [75].

In the set-up used, the optical spectrometer was a $500is$ Chromex spectrograph which was coupled to the Andor ICCD described in previous section. The spectrograph consists of a Czerny-Turner mount with toroidal focusing mirrors which enables aberration-corrected flat field imaging. It operates with a $1200grooves/mm$ diffraction grating, with a blaze wavelength of $400nm$ (the wavelength range of the grating is between $180nm - 900nm$),

providing a resolution FWHM of $0.07nm$ (limited by the spatial resolution of the ICCD). The aperture ratio of the spectrograph is $f/8$ where f is the focal length of $0.5m$. The Reciprocal linear dispersion is of $1.6nm/mm$. The slit width can be varied between $10\mu m - 2mm$. The wavelength accuracy is $\sim 0.15nm$. The instrument function of the spectrograph was previously determined by Kavanagh [21] using a narrow emission line ($441nm$) from a cadmium lamp. Using a slit width of $60\mu m$ (the slit width used in this work), an instrument function of $0.22nm$ was determined. The evaluation of the instrument function is important, as it affects the broadening (see section 1.11.2) of the gaussian part of the detected lines. The calculated magnification for the experiments described here was $1.6X$. Measurements were performed with two different experimental set-ups: in configuration a.), which is shown in figure 3.2.7, a relay lens imaging system was employed to create an image of the colliding plasmas at the entrance slit of the spectrograph; the relay system is composed of a $f = 15cm$ focal length achromatic plano-convex lens, L_1, located inside the vacuum chamber, and an achromatic plano-convex lens L_2 with $f = 10cm$ positioned in front of the entrance slit of the spectrograph. Each spectrum corresponds to the spectral distribution of a horizontal slice of the colliding plasma system, consisting of the two seed plasmas and the interaction region between them. By translating the slit, by means of a micrometric stage moving a table on which the spectrometer is mounted, in increments of $500\mu m$ in the direction normal to the target surface (i.e. along the forward expansion axis of the plasma), different slices of the seeds and the stagnation layer were imaged into the spectrograph, at different distance from the target. Each increment corresponded to a real distance of $0.83mm$ in the object plane. In this way

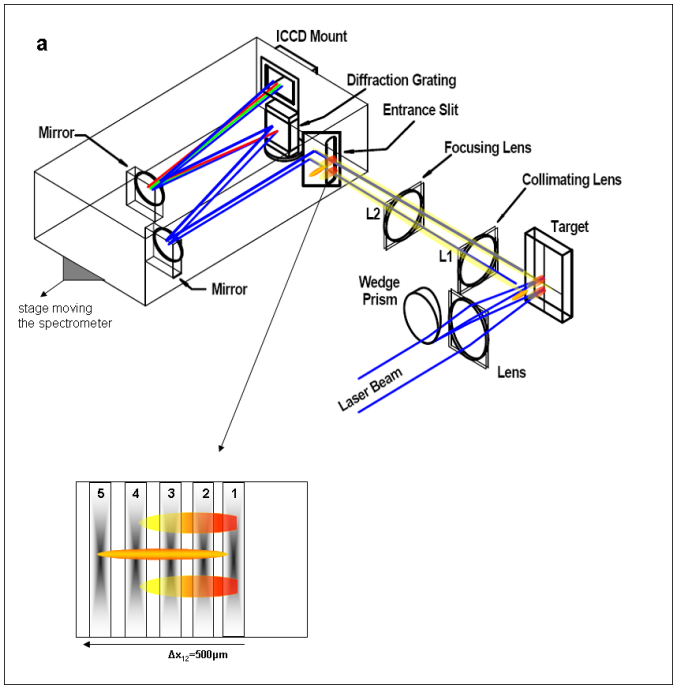

Figure 3.2.7: *Schematic diagram of the optical spectroscopy system without the use of the Dove prism, showing the main optical components, used to image the plasma light onto the entrance slit.*

an accurate spatial resolution of both seeds and stagnation layer expansion was obtained.

In configuration b.), shown in figure 3.2.8, the inclusion of a Dove prism, placed between the two lenses at 45° to the horizontal plane, served to rotate the image of the colliding plasmas, so that the stagnation layer was vertically aligned along the slit of the spectrometer. This offered spatial resolution along the overall extension of the stagnation layer. The same measurements were carried out for the seeds: by means of the micrometric stage, which was able to adjust the position of the spectrograph, the slit

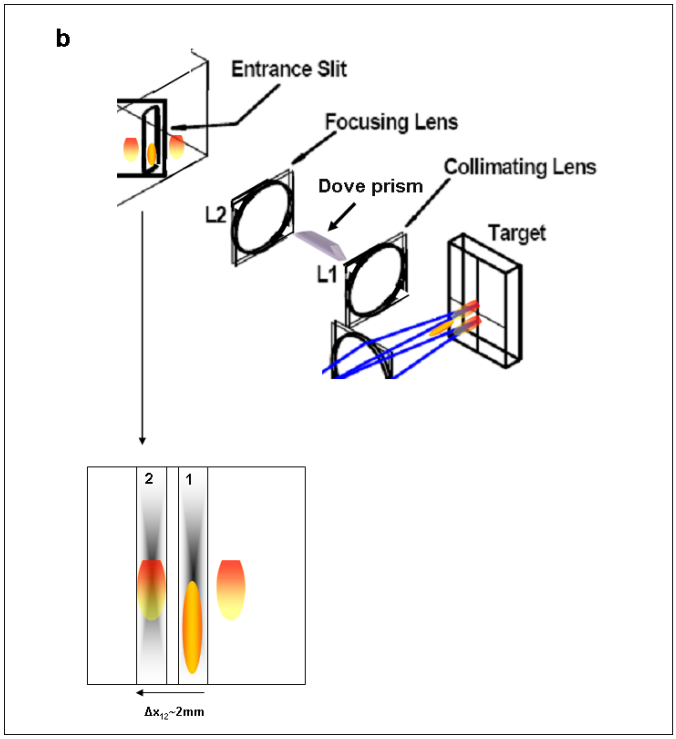

Figure 3.2.8: *Schematic diagram of the optical spectroscopy system with the use of the Dove prism; with the main optical components, in order to image the plasma light at the entrance slit.*

was moved until it was centered on the image of a seed. To center the seed on the slit, the spectrograph must be moved at least $2000\mu m$, since the real distance between the seed and the stagnation layer is $1.3mm$.

The temporal evolution was obtained for both set-ups, by increasing the delay of the gate of the ICCD camera with respect to the laser pulse. A photograph of this experimental set-up is shown in figure 3.2.9.

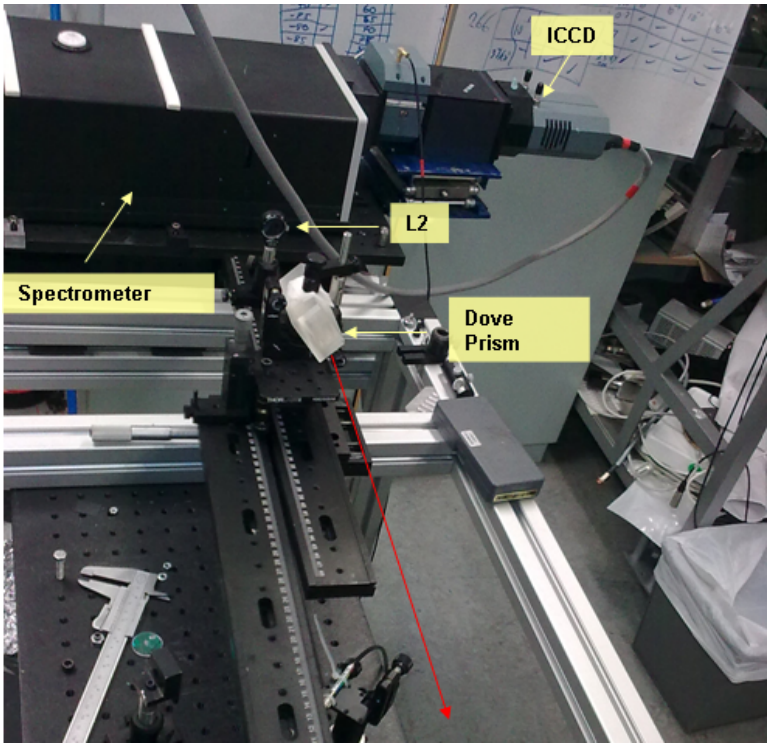

Figure 3.2.9: *Picture of the optical spectroscopy set-up, when the dove prism was located between L_1 and L_2; the orange arrow indicates the direction of the incoming plasma radiation.*

3.2.5 The Timing system

The Surelite Laser system was synchronised to the ICCD detector using two Stanford DG-535 delay generators with a maximum temporal jitter of 1 ns. One of the delay generators constitutes the master oscillator: it generates a reference $+5V$ TTL signal T_0 at $10Hz$ of $10\mu s$ width, which is used to trigger the flashlamps of the pump laser. The second output of the delay generator provides a second similar TTL pulse $180\mu s$ after T_0 (this is the optimal time delay between the laser flashlamp and the triggering of the Pockels cell to

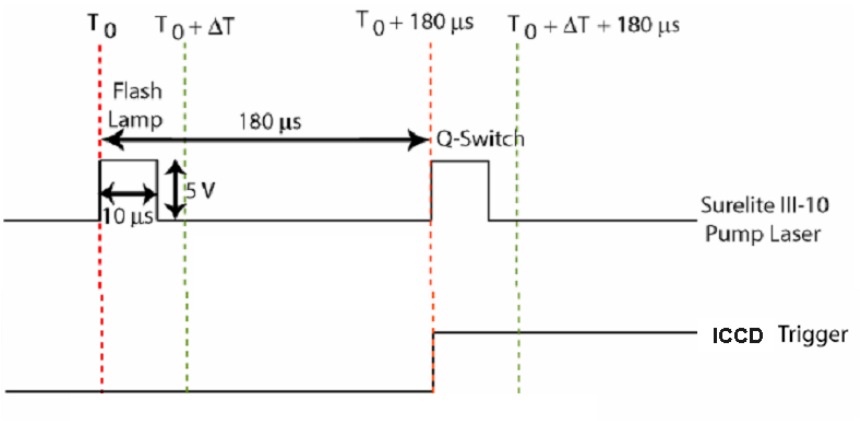

Figure 3.2.10: *Timing Diagram.*

produce a stable high-energy output from the Surelite laser). This output is sent through an AND box and connected to the laser Q-switch. The other input into the AND box comes from the output from the computer which generated a TTL signal for the duration that the ICCD exposure. Only when both inputs into the AND box are positive will, a TTL signal be sent to the laser Q-switch, resulting in a single laser pulse. A copy of this TTL pulse provides the trigger for the gating of the ICCD. Using this this technique the laser can be operated in single shot mode, whilst ensuring the flashlamps triggered at $10Hz$. This fact is important as it stabilises the temperature of the laser rods and hence the laser output. A copy of the T_0 pulse from the master oscillator of the first delay generator is used as external trigger for the second Standford thereby synchronsing the two delay generators. The gate-width of the camera MCP intensifier ($3ns$) was in this way temporally synchronized to the Pockels cell of the laser system. From the Andor Software both ICCD and Chromex Spectrometer can be controlled [39]. The scheme of the timing described above is reported in

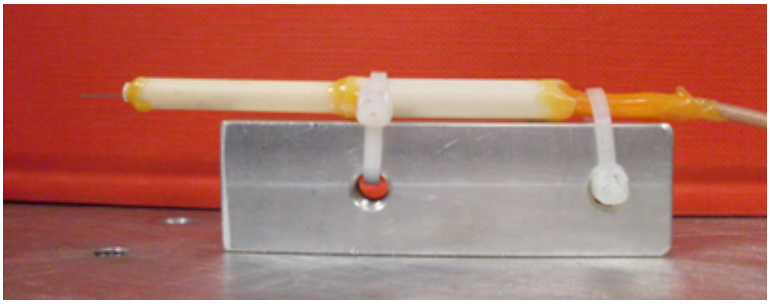

Figure 3.2.11: *Picture showing the homemade LP.*

figure 3.2.10.

3.2.6 The Langmuir Probe

The Langmuir Probe used for the experiments was homemade and designed for this purpose at DCU. It consist of a tungsten ($1-4mm$ long) cylindrical thin tip, with a diameter of $0.5mm$, connected to a long coaxial cable. The tip protrudes from an alumina sheath of $60mm$ length and $5mm$ diameter which covers the coaxial cable. A picture of the Langmuir Probe is showed in figure 3.2.11. It was powered with a HP power supply of $60V$ maximum voltage and $10A$ full scale current. The signal was read out with a BNC feedthrough, through an electric circuit identical to that described in section 2.2.6 of chapter 2, then visualized by means of an oscilloscope. The probe was placed between the two seeds at different distance from the target and, by biasing it from $V = -60V$ to $V = +60V$, the $I-V$ curves, as described in previous chapter, were constructed. TOF signals were also recorded without biasing the probe, in order to limit the perturbation of the stagnation layer, at several distances from the target. For comparative purposes the same measurements were performed on a single plasma generated with a laser

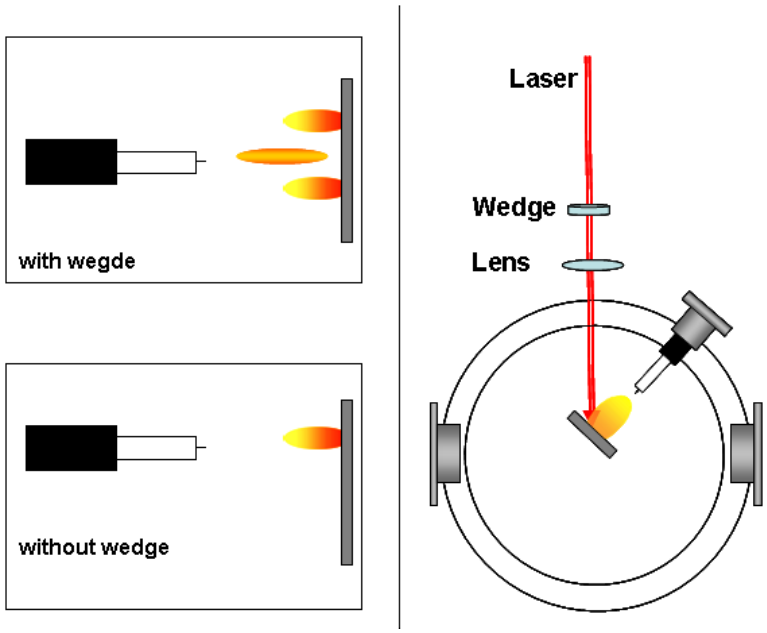

Figure 3.2.12: *Sketch showing the LP measurement set-up*

energies of $E = 300mJ$ and of $E = 600mJ$, by removing the wedge prism from the laser beam line. The probe was placed on the plume expansion axis, to make further comparisons with the stagnation layer signals generated at the same laser energy ($300mJ$ for each seed). A schematic representation of the LP positioning is shown in figure 3.2.12. Since the on axis position could intercept the laser pulse, the target was rotated by 45° with respect to the initial target position described for the imaging experiment.

3.3 Experimental Results

Fast imaging and emission spectroscopy in the visible range, revealed detailed information of the spectral dynamics of the atomic species (neutral atoms and ions) in the seeds and the colliding region. The spectral range

employed proved very versatile to investigate optically the interaction of the plumes, thanks to the high temporal and spatial resolution. The spectral range studied permitted the easy detection of emission lines originating from the atomic transitions of the plasma species and, by applying the theories described in 1.11.2, to characterize both seeds and stagnation layer in terms of electron density and electron temperature. On the other hand, the LP measurements permitted the investigation of the electron and ion dynamics of the stagnation layer, by recording the plasma current signals.

The grating spectrometer was centered on two different wavelength regions: the first at $400nm$, in which we detected two Al^0 (neutral atoms), centered at $\lambda_1 = 394.4nm$ and $\lambda_2 = 396.15nm$. The second region, obtained by centering the grating at $460nm$ allowed the detection of singly and double ionized Al ions. In this region four lines were detected, namely $\lambda_1 = 447.997nm$, $\lambda_2 = 451.256nm$, $\lambda_3 = 452.894nm$ and $\lambda_4 = 466.306nm$. The first three lines refer to double ionized ions $AlIII$ and the last one to singly ionized ions $AlII$. The corresponding atomic transitions are listed in table 3.1 and were identified thanks to on-line databases [68].

Table 3.1: *Detected Emission Lines*

Atomic Species	λ_0 [nm]	Transition Levels
Al^0	394.4	$3s^2 4s \ {}^2S_{1/2} - 3s^2 3p \ {}^2P_{1/2}$
Al^0	396.15	$3s^2 4s \ {}^2S_{1/2} - 3s^2 3p \ {}^2P_{3/2}$
Al^+	466.30	$3s4p \ {}^1P_1 - 3p^2 \ {}^1D_2$
Al^{++}	447.99	$2p^6 5g \ {}^2G_{9/2} - 2p^6 4f \ {}^2F_{7/2}$
Al^{++}	451.25	$2p^6 4d \ {}^2D_{3/2} - 2p^6 4p \ {}^2P_{1/2}$
Al^{++}	452.89	$2p^6 4d \ {}^2D_{3/2} - 2p^6 4p \ {}^2P_{3/2}$

After recording the time resolved spectra, by applying the theories reported in 1.11.2 and by assuming LTE (described in section 1.5), the electron density n_e, and the electron temperature T_e can be determined. On this purpose Stark analysis was used: n_e was calculated by equation (1.11.14), by evaluating the Lorentzian FHWM of the spectral lines. T_e was evaluated using equation 1.11.18, i.e. with Line intensity Ratios from two different charge states. Due to opacity, we could not evaluate n_e and T_e at the early stage of the seed formation (in the first $40 - 50ns$), since here plasma radiation processes are dominated by self-absorption. It was observed that the stagnation layer starts to form between $30 - 40ns$ after the peak of the laser pulse, so no information on T_e or n_e is available before this time.

The experimental data were analysed by means of a Matlab code developed on this purpose. The code fits the spectral lines with a Voigt profile (see equation (1.11.16)), from which the Lorentzian FHWM is extracted. By using the Matlab *Optimset* tool we were able to analyze more than 40 spectra acquired at different stages of the plume expansion in a single loop. For each time resolved spectrum, n_e (which can be evaluated from any emission line) is then used to evaluate T_e, since equation 1.11.18 has an explicit dependence on n_e. In this case, it is clear that T_e can only be obtained from the ion emission spectra. Better fits were obtained by evaluating n_e from the Al^0 emission lines (in particular from $\lambda_1 = 396.15nm$); in this case the ICCD counts were more than the ones obtained for the ionic species; this leads to smaller statistical errors in the fitting routine, and hence to lower standard deviations on the lorentzian FHWM evaluation [4].

[4] T_e must still be evaluated from Al^+ emission spectra, since the two Al^0 emission lines listed in table 3.1 refers both to the ground state, so that Line Ratio from the same ionization stage (eq. (1.11.17)) cannot be applied as $E_{b2} - E_{b1} = 0$.

Spectra were recorded every $10ns$ for both imaging and spectroscopy with an ICCD gate of $3 \pm 1ns$. At later expansion stages, when the intensity of the emission began to decrease, the gate width of the camera was increased from $3ns$ to $20 - 30ns$ (or/and the camera gain), or the number of shots was increased to 5 or 10 to allow sufficient flux to be detected in order to correctly observe the plasma dynamics. This procedure was applied only for spectroscopy and not for imaging, where only single shot images were recorded.

3.3.1 Time and Spectral Resolved Emission Imaging

In this section the spectrally resolved fast imaging of colliding plasmas is reported. Specifically, in figure 3.3.1 the fast imaging of broadband, neutrals and singly ionized atoms is shown, respectively.

The images presented in figure 3.3.1 were obtained by recording time integrated spectra (acquired with a ICCD time exposure of $10\mu s$), so both of the seeds and the stagnation layer were visible. The first colliding particles are those coming from the lateral expansion of the single plumes, rather than those originating from the forward expansion of the seed plasmas. Inside the interaction region, their kinetic energy is then converted into excitation energy, which determine the formation and the subsequent emission of the stagnation layer, which appears as a bright strip of light. It is clear that the excitation energy has to be high as the upper and lower levels of the selected transitions, in the case of the ionic transition related to $\lambda = 466.3nm$ the upper levels between $E_1 = 10.6eV$ and $E_2 = 13.25eV$, respectively, above the ground state.

Figures 3.3.1 show also that the neutral atom distribution is quite differ-

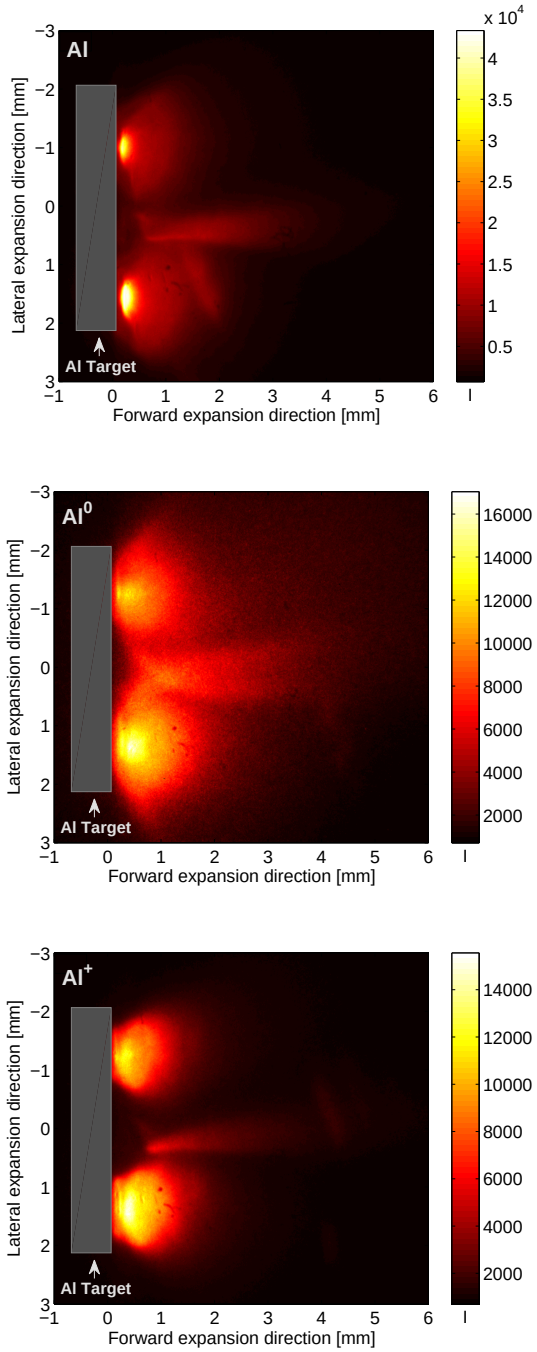

Figure 3.3.1: *Time Integrated images of Broadband, Neutrals and Ions, respectively.*

ent from the ions one: in particular, the ions show a more forward peaked distribution, whereas the neutrals show a broader distribution. The Broadband image shows all light coming from both seeds and stagnation layer (all atomic species), hence a lager number of ICCD counts are obtained. The dynamics observed here is very similar to that obtained by other authors, as shown in figure 1.10.1. The forward peaked shape of the ions is due to the self generated electric field inside the plasma (i.e. the ambipolar potential), which has been already introduced in chapter 1 and experimentally observed in chapter 2[5].

The expansion can be better followed by studying the time resolved images. For this purpose a broadband spectral image sequence for different expansion times, is presented in figure 3.3.2. Six images, showing the more interesting stages of the collision front evolution are reported. At $t = 30ns$ it can be observed that the first collision between the seed plasma particles occurs closer to the lower seed. At $t = 50nsec$ the stagnation layer is definitively formed, as it is evident by the increase of emission from the central region. At $t = 100nsec$ it further evolves and becomes broader. Contemporary, emission from the seed strongly decreases. At $t = 170ns$ the seeds are no longer visible, while the stagnation layer is still evolving. Emission from the stagnation layer is detected for several hundred nanoseconds, as evident in the image recorded at $300ns$ (although the intensity does decrease). The interaction layer has a maximum extension of $3mm$ along the expansion axis and of maximum $1mm$ along the vertical axis. It is also observed that emission from the stagnation layer becomes more uniformly distributed after $t \sim 200ns$. Although the layer is still visible until $t = 400ns$ (not reported

[5]The influence of the electric field must be included when numerical simulations, reported in chapter 5, able to reproduce the experimental data are used.

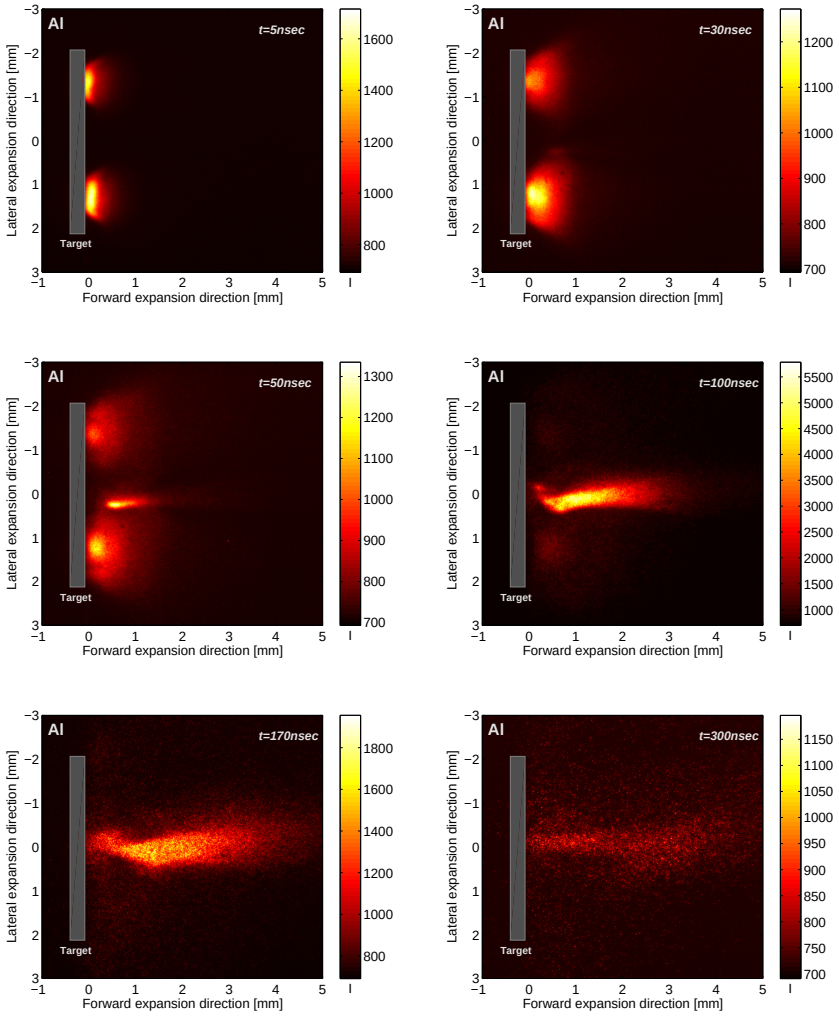

Figure 3.3.2: *Time resolved images of broadband emission at different delay times:* $t = 5ns$, $30ns$, $t = 50ns$, $t = 100ns$, $t = 170ns$, $t = 300ns$. *The ICCD gate was increased to* $15ns$ *at* $t = 170ns$ *and* $t = 300ns$, *in order to increase the camera counts.*

here), by this stage the emission is almost at background levels. Similar time resolved images were observed for neutral atoms and ions. However, ion emission decays quicker, as one would expect at $t = 150ns$ the stagnation layer distribution is like that reported for broadband at $t = 300nsec$, and also more forward peaked, as showed in figures 3.3.1.

As previously mentioned, at $t = 30ns$ the first plasma species collide closer to the lower seed. This means that particles from the upper seed travel with higher velocity, even if this seed appears to be less intense. This can be explained by the fact that the upper plume, formed with a slightly lower laser energy, carries a lower inertia, hence resulting in a lighter plume whose particles evolve more rapidly.

The velocity of the first colliding particles can be calculated easly: at $30ns$, the distance d between one seed at $x = 0mm$ and the center of the tight early stagnation layer is $d = 1.166mm$, hence the velocity[6] is $v = d/t = 3.9 \cdot 10^5 m/s$. This value is in agreement with the mean velocity values obtained in chapter 2, for the fast and ultrafast plasma particles composing the coronal part of the plume, which escape first after the ablation process.

3.3.2 Time resolved seed and stagnation layer characterization

In this section the characterization of the seed plasma and the stagnation layer in terms of electron density and plasma temperature will be presented, where the measurements were carried out with the Dove prism (hence by

[6] d is the hypotenuse of the triangle of sides $l_1 = 0.3mm$ and $l_2 = 0.6mm$, calculated respectively from the coordinates of the seed at $x = 0mm$ centered in the vertical axis at $y = 1.3mm$, and from the position of the tight stagnation layer whose center coordinates in mm are $(x, y) = (0.6, 0.3)$.

using the experimental set-up reported in 3.2.8).

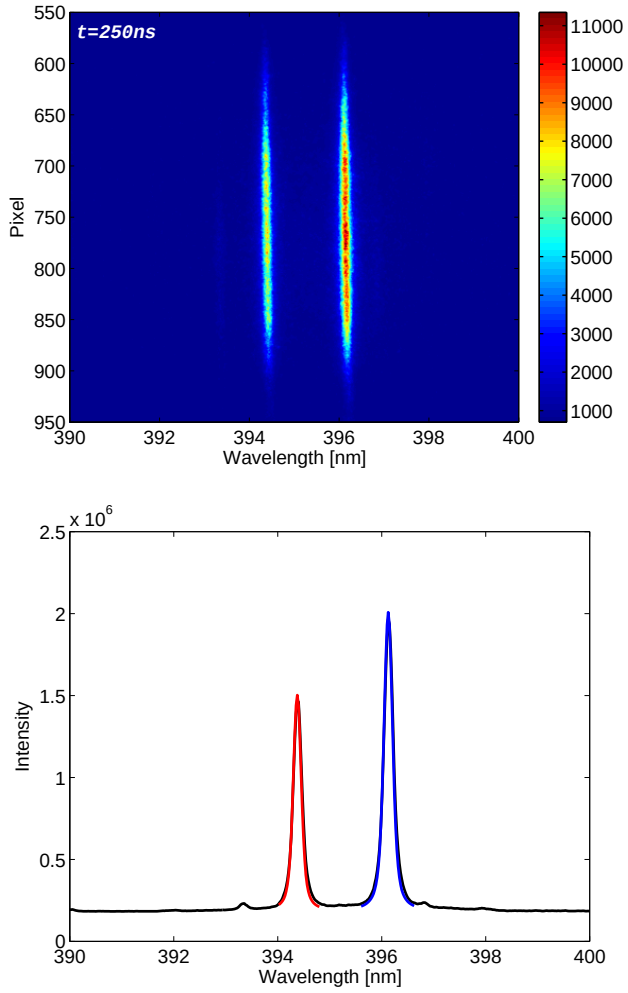

Figure 3.3.3: *Time resolved spectrum obtained at* $250ns$*, with the slit aligned to the seed expansion axis in a wavelength region centered at* $390nm$ *(up) and corresponding spectrum obtained by fully binning the pixel lines (down). The same procedure was applied when the spectrograph slit was centered at the stagnation layer.*

Figure 3.3.3 shows a time resolved spectrum, acquired with the slit centered on the seed plasma (left) at $t = 250ns$. By fully binning the CCD counts along the vertical axis of the spectrum shown in the upper figure the spectra shown below is obtained. The fitted Voigt profiles were obtained with the Matlab code and are shown for both emission lines. As one can observe from this figure, the code generates good fits to the experimental lines. The background noise affecting the spectrum is semi-automatically subtracted by the code, by selecting a spectral region with no lines with the same range as that of the line to be fitted. Spectra like that shown in figure 3.3.3, were recorded every $10ns$ and processed in a similar manner, thus revealing the time resolved density for both the seed and the stagnation. The densities profiles are shown in figure 3.3.4. Density values are available for times expansions upon $t \geq 80ns$, for the physical reasons explained in section 3.3, i.e due to the influence of self-absorption, that distorts and attenuates the emitted spectral lines and hence conventional stark analysis is not applicable.

Figure 3.3.4, aids in the understand of both seed and stagnation evolution dynamics: the seed density is decreasing adiabatically, as observed also for the single plume studied in chapter 2, and decreases towards zero at $t = 500ns$.

The stagnation layer however shows a larger density than the seed plasma between $t = 200ns$ and $t = 600ns$: thereafter it decreases with a longer delay time if compared to the seed electron density. The stagnation layer has thus a slower dynamic, as expected, and the density *stagantes* for approximately $200ns$, from $t = 300ns - 500ns$. At expansion stages upon $t = 600ns$, both densities decrease to zero.

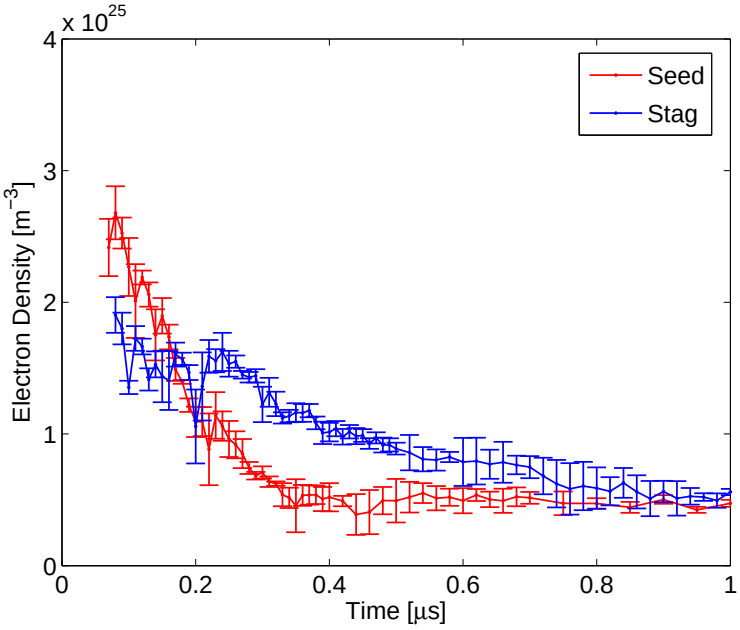

Figure 3.3.4: *Electron Density profiles vs time for the seed and for the stagnation layer.*

In figure 3.3.5, the time resolved electron temperature for the seed T_e^{seed} and for the stagnation layer T_e^{stag} is reported. Here one observes a bigger temperature for the stagnation layer, until $t = 200ns$, which then decreases to lower values at $t = 500ns$, where both temperatures becomes comparable. In the first $200ns$ the conversion of the ordered kinetic energy of the colliding seed particles into disordered thermal energy at the collision front leads to higher temperatures for the stagnation layer. Subsequently, a rapid decrease of T_e^{stag} is observed, corresponding to the region where n_e^{stag} is higher. This phenomena can be explained as follows: because of the high number of collisions, mainly consisting of binary (inelastic) and ionization collisions (see section 1.4.1), electrons may *loose* most of their energy. These processes, due

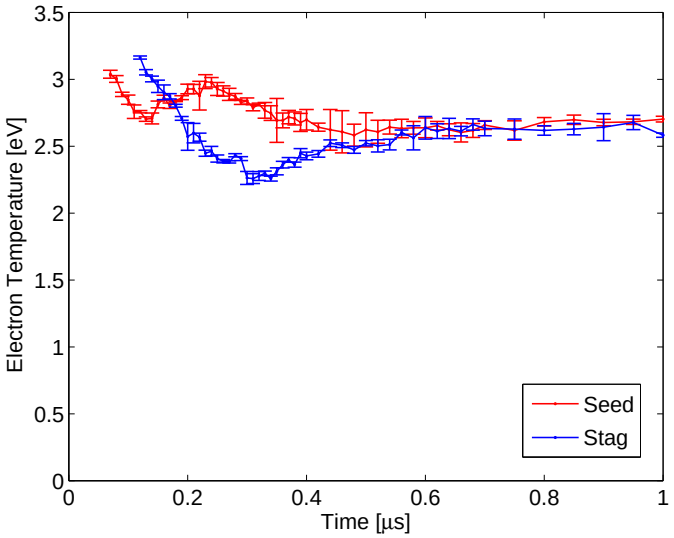

Figure 3.3.5: *Electron Temperature profiles vs time for the seed and for the stagnation layer.*

to the high n_e^{stag}, can dominate on the energy gained from the conversion of their kinetic energy into thermal energy, hence leading to lower T_e. Between $t = 300ns$ and $t = 500ns$, T_e^{stag} increases once again; this is probably due to recombination effects, as studied also in section 2.3.2 for the single plume expansion.

The seed appears to evolves like a two electron temperature plasma, and later on undergoing to free-isothermal expansion, after $400ns$.

Both temperatures do not decrease consistently to zero at late expansion stages, i.e after $t = 600ns$. The most probably reason for this unexpected behaviour is the model used to obtain T_e. Equation 1.11.18, from which T_e is evaluated, assumes that the plasma is in LTE. However, at these later expansion times this assumption is no longer valid. A different theoretical

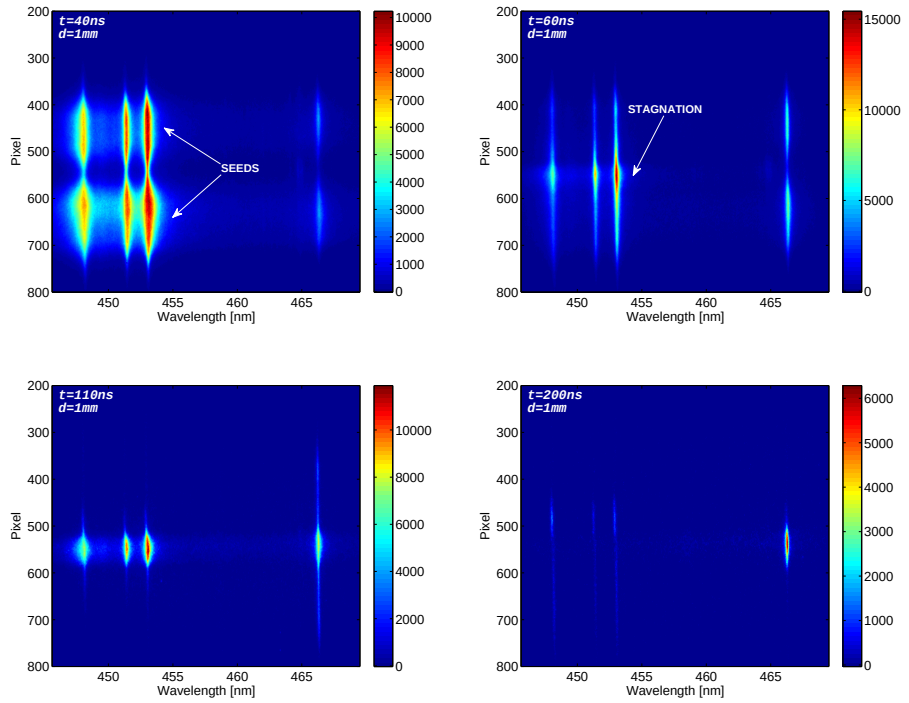

Figure 3.3.6: *Time resolved spectra obtained at* $t = 40ns$*,* $t = 60ns$*,* $t = 110ns$ *and* $t = 200ns$*.*

model, like the CRE model (see section 1.5) should be used to extract the temperatures values, however this is beyond the scope of the current thesis.

3.3.3 Time and spatial stagnation layer characterization

In this section the stagnation layer was temporal and spatial characterized by using the experimental set-up shown in figure 3.2.7; the interaction region was hence imaged on the slit, at different distances from the target, as explained in detail in section 3.3.

In figure 3.3.6 four time resolved spectra are reported, with the spectrograph positioned $1mm$ from the target surface. In this case, by removing

the Dove prism, contemporary both the seed plasmas and the stagnation layer can be imagined in one frame.

At $t = 40ns$, only the seed evolution is observed, between $500 - 600$ pixels for the upper seed and between $700 - 800$ pixel for the lower one. The stagnation layer forms between the two seeds located pixel at $520 - 580$, and becomes more pronounced at $t = 60ns$. In this region the pixels are binned vertically in order to obtain the electron density using the method described in previous section. An important peculiarity that can be observed from the time resolved spectra is the evolution of the different charge states: at $t = 60ns$ the spectrum gives out three important pieces of information:

- the radiation emitted from the seeds begins to consistently decrease;
- double ionized atoms, associated to the first three emission lines, stagnate earlier, due to the higher expansion velocities with respect to the singly ionized atoms (associated with $\lambda = 466.3nm$).

For Al^{+}, the stagnation layer hence forms at later expansion stages on a time scale on the order of $t = 110ns$. The spectrum reported at $200ns$ then shows how the stagnation layer formed by Al^{++} ions decays and the stagnation layer formed by Al^{+} ions is still clearly visible, compared to the other emission lines. This evidence is of paramount importance for the comprehension of the plasma dynamics: it reveals that the splitting of the different charge states into the plasma studied in detail in chapter 2. The highest one populate the front of the plume.

In figure 3.3.7 we finally report the electron density evolution of the stagnation layer versus time and versus distance from the target surface. For expansion phases up to $t = 500ns$, spectra were acquired every $20ns$, $50ns$ or $100ns$. The electron density values obtained at different times and

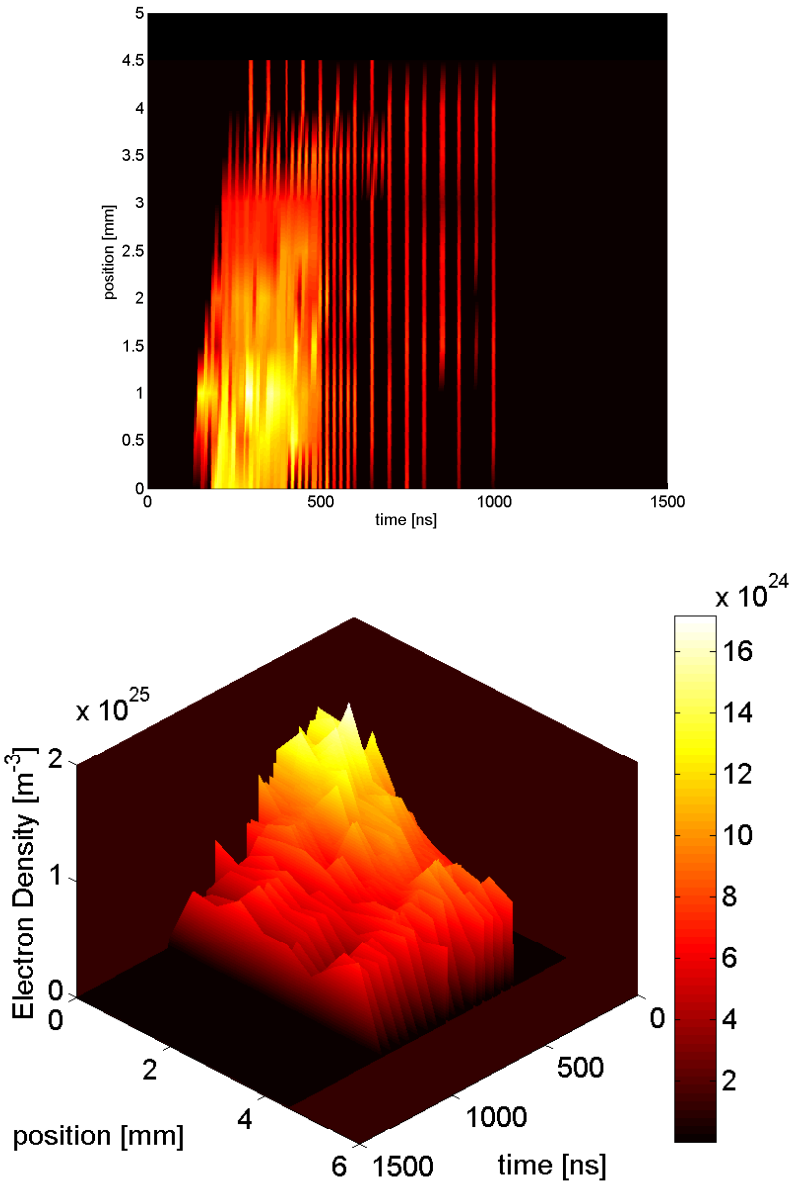

Figure 3.3.7: *Stagnation Layer Electron Density vs. time and vs. distance from the target, shown in 2D (top) and 3D (bottom); the mesh was obtained through an interpolation Matlab routine.*

distances were interpolated by using a Matlab routine. Figure 3.3.7 shows when the stagnation layer density assumes its maximum value: it is on the order of $n_e = 1.7 \cdot 10^{25} m^{-3}$ at $d = 1mm \pm 0.25mm$ at $t \sim 300ns$. The maximum density value, and its trend versus time, is in agreement with the n_e value determined in the previous section by means of the experimental set-up including the Dove prism. Also in this case, the density stagnates for about $200ns$, between $t = 300ns$ and $t = 500ns$, then starting to consistently decrease after $t = 500ns$, at $2 - 2.5mm$ from the target. At $d = 4mm$, the density abruptly decreases more than one order of magnitude with respect to its maximum value. Spectra recorded at distances up to $d = 4.5mm$ were not analyzed due to the low number of ICCD counts. Plasma emission was still observed up to $d = 6mm$ from the target.

With this experimental configuration, since both seeds and stagnation layer are followed simultaneously, when the stagnation layer starts to form and the seed plasmas are still expanding, the spectra must be analyzed carefully, to avoid contamination of emission from the seeds in the emission spectra of the stagnation layer (some overlapping emission regions along the vertical axis can exist). This only occurs for brief time expansion windows: seed line emission is not anymore significant for time expansion[7] upon $t = 100ns$.

[7] also in this case of 3.2.8, the stagnation layer must be centered on the slit with care, to avoid detection of radiation emanating from the lateral expansion of the seed plasmas.

3.3.4 Investigation of the stagnation layer by means of a Langmuir Probe

As mentioned in section 3.2.6, the collection of the LP signals at the stagnation layer was performed at several distances from the target, with biased and unbiased probes. The same measurements were then repeated on a single plume created with a laser energy of $600mJ$, by removing the wedge prism from the laser beam line, as shown in figure 3.2.12. Since the data analysis is still in progress, we herby report only the TOF signals recorded respectively for the double and for the single plume expansion when the probe was placed at $d = 15mm$ and $d = 30mm$.

In figure 3.3.8 the time of flight signals, when the probe was located on axis at $d = 15mm$ and $d = 30mm$, from the target, are reported. Both current signals for the double plume configuration and for the single plume configuration are shown. It is evident that the signals recorded at the stagnation front have an amplitude consistently larger and a longer duration with respect to the TOF signal recorded for the single plume. These trends hence show the contribution of the stagnation layer to the collected current signals. For the ions the stagnation contribution is even lager, either in time and intensity; for the electron the contribution of the stagnation layer is more evident in the temporal duration. On this purpose it should be noted that a current plateau in the electron signal is observed at $d = 15mm$ for the double plume configuration, between $1\mu s - 3\mu s$ (this effect is less evident at $d = 30mm$ as the probe is too distant from the stagnation layer region). This signal plateau is a signature of the electrons stagnation, and is in agreement with the results obtained with optical spectroscopy, where it is observed that n_e is maintained roughly constant for several hundred ns.

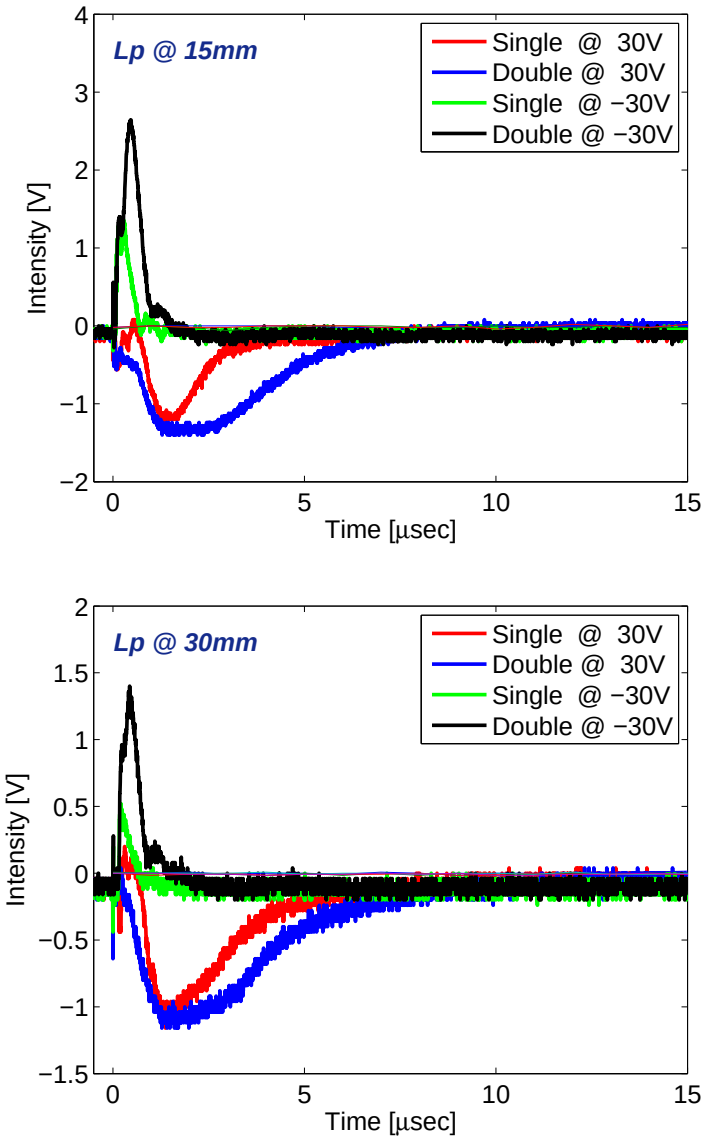

Figure 3.3.8: *TOF signal at the stagnation layer and of a single expanding plasma plume when the probe was biased with* $+30V$ *and* $-30V$ *and placed at different distances from the target, respectively* $d = 15mm$ *and* $d = 30mm$.

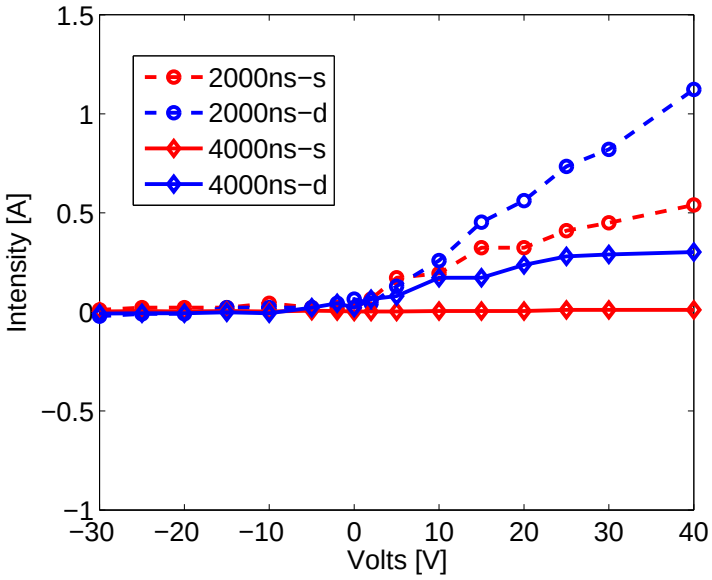

Figure 3.3.9: *I-V curves construction when the probe was located at* $d = 5mm$ *from the target at* $t = 2000ns$ *and* $t = 4000ns$.

The same dynamics becomes more evident by calculating the different $I - V$ curves trends, as shown in figure 3.3.9. Here $I - V$'s for the single plume and for the double plume at two different times, ($t = 2000ns$ and $t = 4000ns$) are reported.

The $I-V$ trends at $t = 2000ns$ for the double plume configuration show a much longer current contribution, similar to the trends observed for the single plume at earlier time expansion. At $t = 2000ns$, the curve for the single plume shows a lower electron saturation current, meaning that the plasma is approaching at the final stage of its expansion. At $t = 4000ns$ expansion stops, but the double plume still shows a current contribution, as observed also with the TOF signals.

These trends confirm that the stagnation layer is effectively a third

plasma, whose dynamics persist for longer times, as compared to the single plume. Further investigations are required, to further understand the underlining dynamics, namely by analyzing the $I - V$ curves reported above and extracting the electron density and temperature as performed in chapter 2 for the single plume expansion.

3.4 Conclusions

We reported in this chapter the preliminary data analysis from the measurements performed on colliding laser produced plasmas. Either the stagnation layer and the seed plasma have been characterized in terms of their respective electron densities and temperatures.

Their values were compared with those ones obtained by other authors on Al colliding plasmas, with a flat target configuration and with comparable laser energies. Differences with the literature can be explained by the different distances D between the two seeds [39, 76].

The stagnation layer was characterized with two different experimental configurations: both the set-ups gave comparable time resolved n_e values and evolution trends for the stagnation layer.

From the imaging it was observed that the stagnation layer begins to form at $t = 30ns$, thus determining that fast particles with velocity on the order of $v = d/t = 3.9 \cdot 10^5 m/s$ are the first to collide. These particles most likely consist of fast escaping electrons followed by highly charged ions, which at the stagnation are prone to recombination effects, hence forming the uniform stagnation layer. Earlier stagnation of higher charge states was also observed from the spectra reported in figure 3.3.6.

Already by Hough et al. [53] it was observed that electrons stagnate

$10ns$ earlier with respect to the higher charged ions. They deduced that the earlier stagnation of electrons at the mid-plane collision front induces a significant *screening* effect, which permits to the ions (especially the highly charged ones) to approach each other quite closely, leading to a tight ion stagnation layer. This effect was more pronounced at the early stages, when n_e reaches quite high values.

From the arguments discussed above it appears that the plume interaction at low laser energy could be useful in the study of ES. The stagnation layer must be considered as a third plasma, with a more uniform particles distribution respect than a single plasma. Electrons stagnate for some hundred of ns, having between $200 - 300ns$ a much higher density as compared to a single plume. Contemporary, they have lower temperatures, on the order of $2 - 2.3eV$ whereas the single plume has, at comparable times, electron temperatures on the order of $2.8 - 3eV$. These condition would indicate a high influence of ES, as it scales with the ratio of n_e/T_e.

Chapter 4

Investigation of thin foils colliding plasmas

In this chapter initial results obtained on the characterization of colliding plasmas produced by the laser ablation of thin Al targets, are reported.

4.1 Introduction

Studies of plasmas produced by the laser ablation of thin foils are mostly devoted to proton acceleration [10]. On this purpose femtosecond lasers are usually employed in order to produce high-energy ions (from the MeV to the GeV scale) [77, 78]. These studies are devoted to the development and construction of more compact and powerful accelerators, succeeding conventional ones.

In a still higher laser energy regime, colliding plasmas produced from thin foils are devoted to astrophysical and ICF applications [46, 79], as reported in section 1.10. In a low laser energy regime, colliding plasmas generated

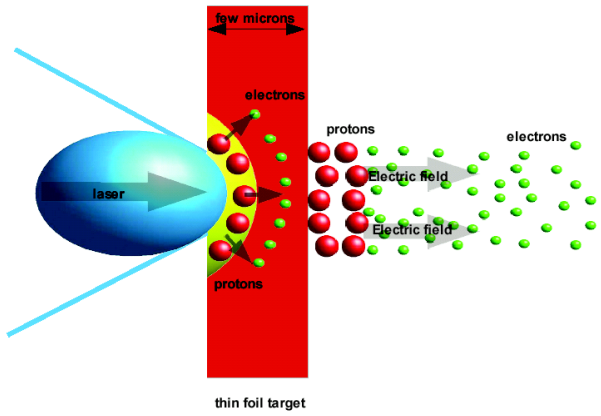

Figure 4.1.1: *Acceleration dynamics occuring from the interaction of a thin foil with a high intensity laser: electrons emerge at the rear side of the foil inducing a large electrostatic charge field, which in turn accelerates protons moving perpendicular to the target surface.*

from thin foils are, for the most part, unexplored. Only few studies, in $80 - 90's$ of the last century by employing poor diagnostic tools have been performed [79].

$2\mu m$ Al foils

4.2 Experimental set-up

The experimental set-up used for the characterization of the thin Al foil colliding plasmas, was similar to that described in the previous chapter. The laser system, the diagnostic tools and the analysis method is hence not repeated here, as it was described in detail in chapter 3.

The main differences where obviously the target thickness (which was of $2\mu m$) and target mount. In this case the thin foil was held by a target

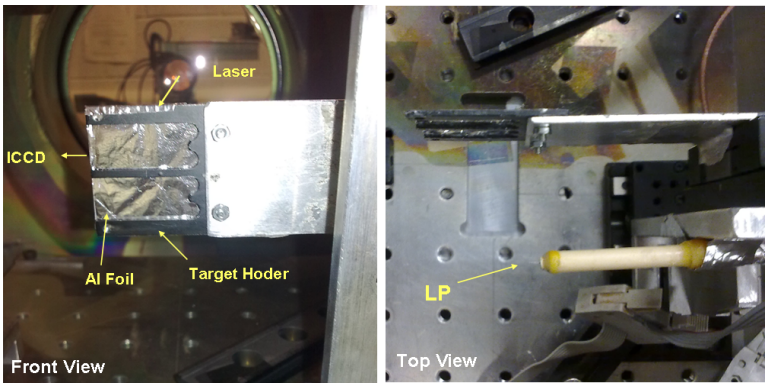

Figure 4.2.1: *Target holder set-up constructed for the thin foils measurements, front view (left) and top view (right).*

holder as shown in figure 4.2: it has a *comb* form, clearly visible looking at the left figure. The target was stretched between two identical comb-holders, then attached to the main motorized holder (described in chapter 3). The particular form of the holder was chosen in order to achieve an "open" side of the target, allowing unobstructed imaging and spectroscopy measurements.

The laser splitting tool for the formation of the seed plasmas is that one described in section 3.2.2.

Fast time resolved imaging was performed in a similar manner as described in section 3.2.3, with only the optical gate of the ICCD differing (in this case it was of the order of $20ns - 40ns$). The increased gate width was required to insure sufficient CCD counts, as radiation emitted from the plasma was, as expected, significantly lower for the thin foil targets, if compared to the thick targets. Time resolved spectroscopy was employed using the Dove prism, (the set-up shown in figure 3.2.8), and spectra were recorded in the same wavelength regions as reported in the previous chapter. In both

time resolved imaging and spectroscopy the number of spectra acquired was limited, as after a single shot the target is perforate, and the target surface must be moved at least of $1mm$ to generated a subsequent plasma. For this reason spectra were acquired in time increments of $30 - 50ns$.

The LP was placed at the rear side of the foil, at $45mm$ from the target surface, as shown in figure 4.2; single TOF signals were collected at fixed voltages.

4.3 Characterization of plasmas produced by thin foils

Preliminary results obtained with our main diagnostic tools, i.e time resolved Imaging, Optical Spectroscopy and Langmuir Probe measurements, are presented in this section.

In figure 4.3.1 two time integrated images (broadband and singly charged ions) obtained from the collision of the two seed plasmas generated from the thin Al foils, are reported. In the broadband images it can be observed that the main plasma still expands at the front side of the target: at the rear side, less intense but still significant emission is observed. However, looking at the time integrated image of the ions, a non consistent presence of backward plasma was detected.

This particular dynamic can be followed in more detail by observing the time resolved spectra, as reported in figure 4.3.2. Here the broadband images show that a back expanding plasma is significant at later times: it appears to have a much slower dynamic, comparable in time to the stagnation layer expansion.

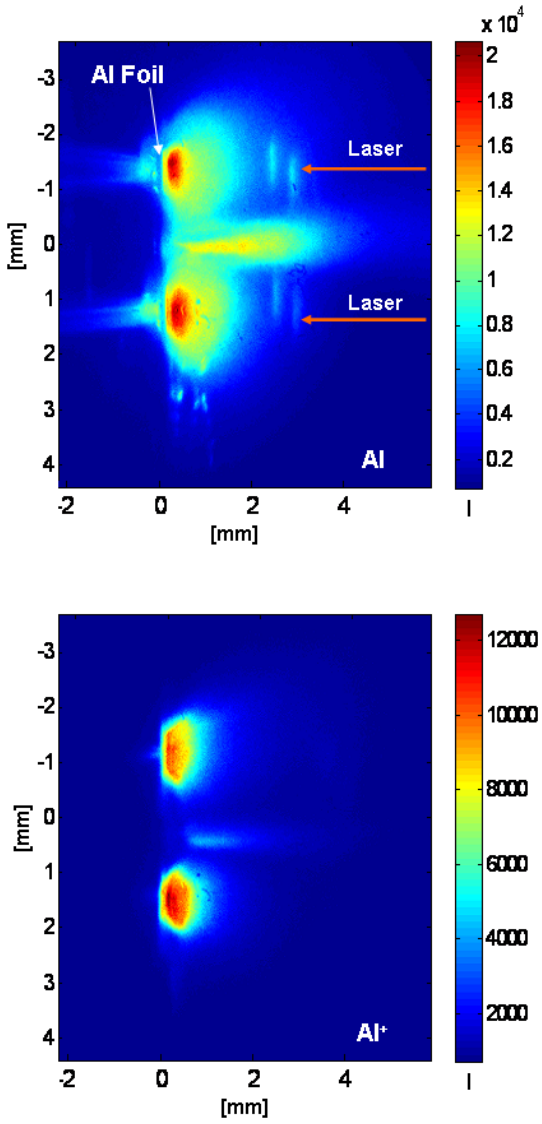

Figure 4.3.1: *Time integrated images of colliding plasmas: broadband imaging (top), ion imaging (down)* .

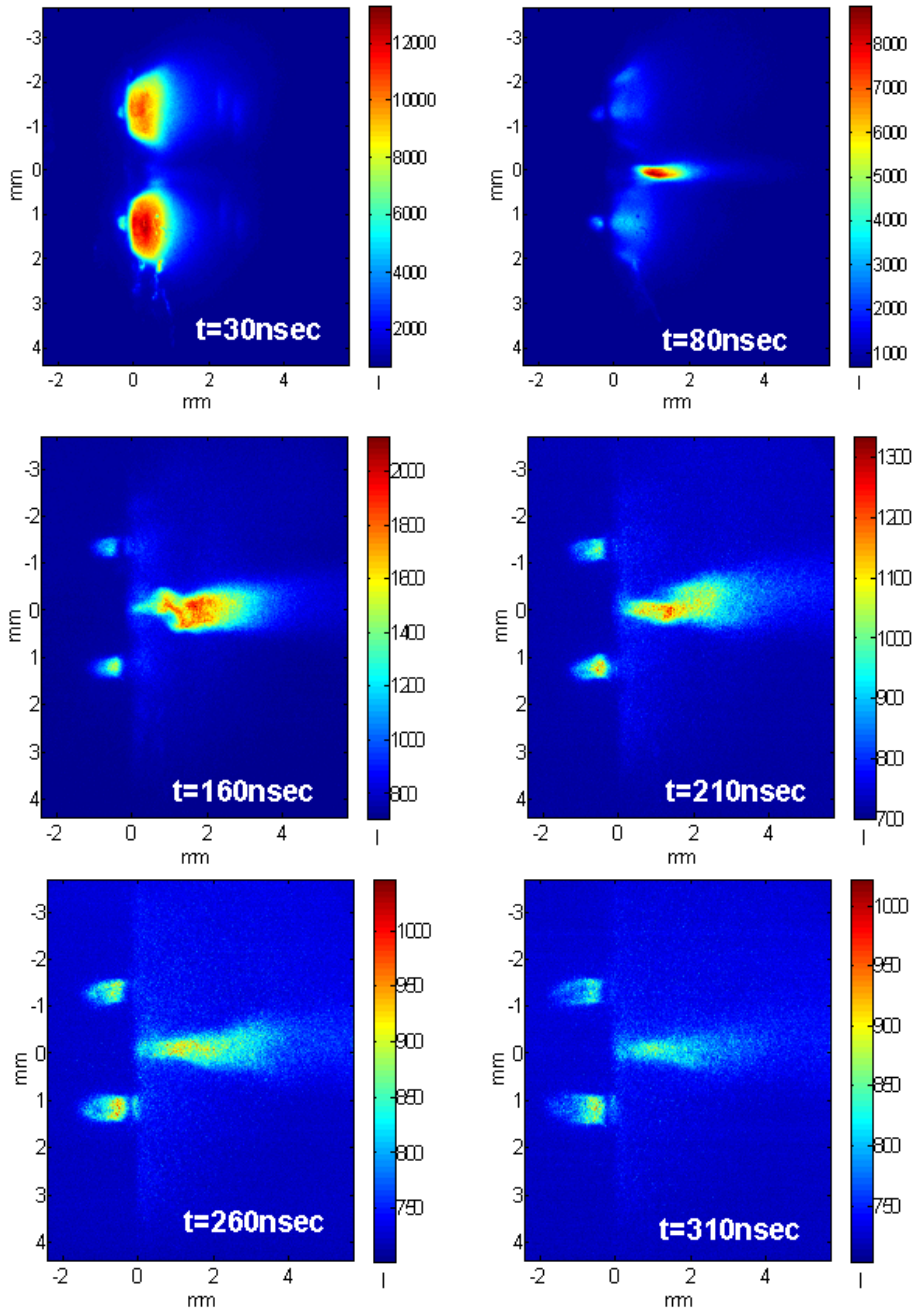

Figure 4.3.2: *Time resolved broadband images at* $t = 30ns$, $t = 80ns$, $t = 160ns$, $t = 210ns$, $t = 260ns$ *and* $t = 310ns$.

At $t = 30ns$ the stagnation layer begins to form (a light halo is visible between the seeds), the backward plasma starts to be generated from both seeds but it is more tightly confined than the forward expanding seeds. At $t = 80ns$, the stagnation layer emits strongly while the emitted radiation from the seed plasmas abruptly decreases. At this time the back-plasma is still visible, but seems to decay with the seed expansion. At later times, such as at $t = 160ns$, the stagnation layer is clearly evident, and emission of radiation is still observed from the backward plasma, while seeds expansion have almost totally disappeared. Thereafter the backward plasma evolves slowly in time together with the stagnation layer, which is visible until $t \sim 510ms$ (not shown here). From the images presented in figure 4.3.1 one can deduce that the singly charged ions composing the seeds are mostly forward peaked, and the backward plasma component is mainly composed of neutral atoms and electrons. This was also confirmed by optical spectroscopy and LP measurements.

Two spectra, obtained for the neutral atoms and for ion emission wavelength regions are reported in figure 4.3.3. These spectra were obtained for a single expanding plasma plume with a laser energy of $E = 300mJ$. The two spectra clearly show that in the doublet Al^0 emission region the lines also present on the rear side of the target (where the back plasma expands). In the singly and doubly charged ion wavelength emission region, however, no lines are observed at the rear side of the target, except perhaps, very close to the target surface.

From the doublet Al^0 spectrum we can evaluated the electron density, again using equation 1.11.14. The lorentzian FHWM was evaluated by fitting the emission line centered at $\lambda = 396.15nm$, by means of the Matlab

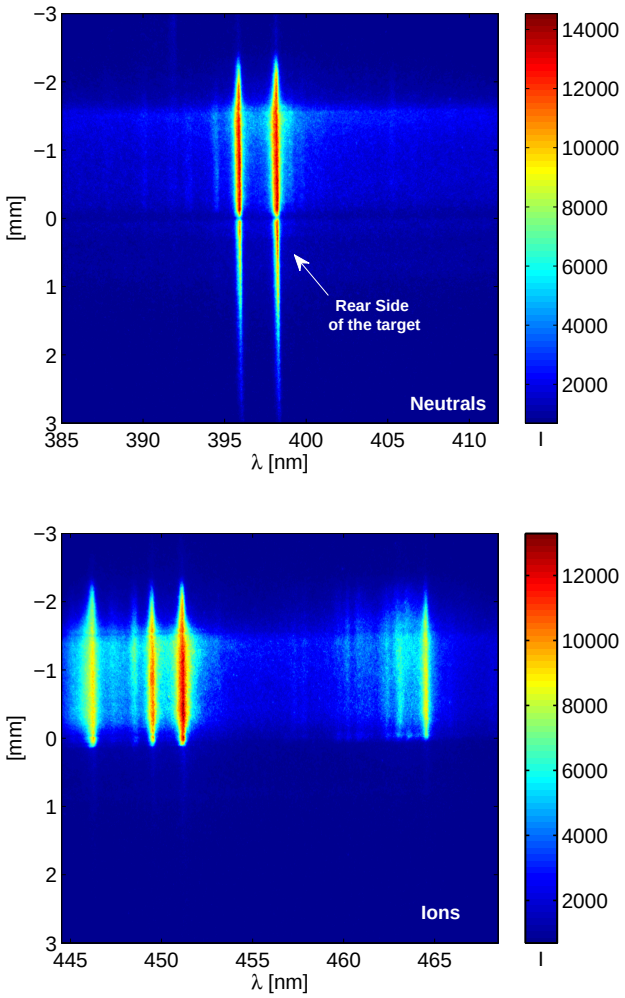

Figure 4.3.3: *Spectra obtained on a single plume with a laser energy of* $300mJ$*, in two different wavelength regions: line emission for* Al^0 *atoms (top) and for* Al^+*,* Al^{++} *(bottom); the relative atomic transitions are listed in table 3.1.*

code described in section 3.3. For the backward plasma a mean density value of $n_e = 5 \pm 0.02 \cdot 10^{24} m^{-3}$ was obtained, by fully binning the pixel lines at the rear side of the target. For the forward expanding plasma a mean density of $n_e = 1 \pm 0.07 \cdot 10^{25} m^{-3}$ was obtained, double that of the backward plasma. Temperature evaluation was more difficult to be obtained, as expected, because the ion emission at the rear side of the target is quite close to the target surface, where each spectrum is severely affected by self-absorption. T_e was however evaluated for the front part of the plume: its value of $T_e = 2.5 \pm 0.08 eV$ was obtained by using equation 1.11.18, and it is comparable to the mean values obtained in the previous chapter for the seed plasmas in case of bulk Al targets.

The *back-electron* dynamics, was further investigated by biasing the LP placed on the rear side of the target, with $V = +30V$. The TOF signal is reported figure 4.3.4, together with a second signal obtained when the probe was biased with $V = -30V$. As seen in this figure, by biasing the probe with a positive voltage, the electron signals are revealed, with currents on the order of a few mAs. The ion signal is quite low when compared to the electron TOF signal. Looking at the electron signal, the main peak is located at $22 \mu s$[1]. Since the probe is located at $d = 50mm$ from the target surface, a mean velocity of $2.27 \cdot 10^3 m/s$ for the back-flowing electrons is obtained. This value is in agreement with the slow dynamic observed for the back-plasma through the time resolved imaging.

To avoid potential light reflections from the foil misleading the results, some spectra were acquired by using the configurations shown in figure 4.3.5. By covering the front plume, emission from the rear side of the target was

[1] omitting the analysis of the fast peaks

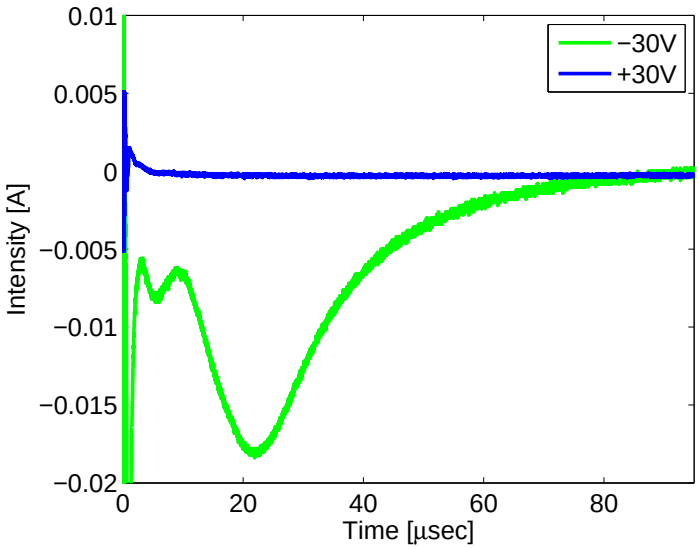

Figure 4.3.4: *TOF signal acquired from the rear side of the foil, when the probe was located at* $50mm$ *from the target.*

still observed. Moreover, by firing the laser on the target holder we did not observed line emission from the rear side of the target. These measurements, combined with the LP data, add greater confidence that the spectra and images presented and analysed in this chapter were indeed due to the backward expanding plasma, and not an artifact of the challenging experimental configuration required for these studies.

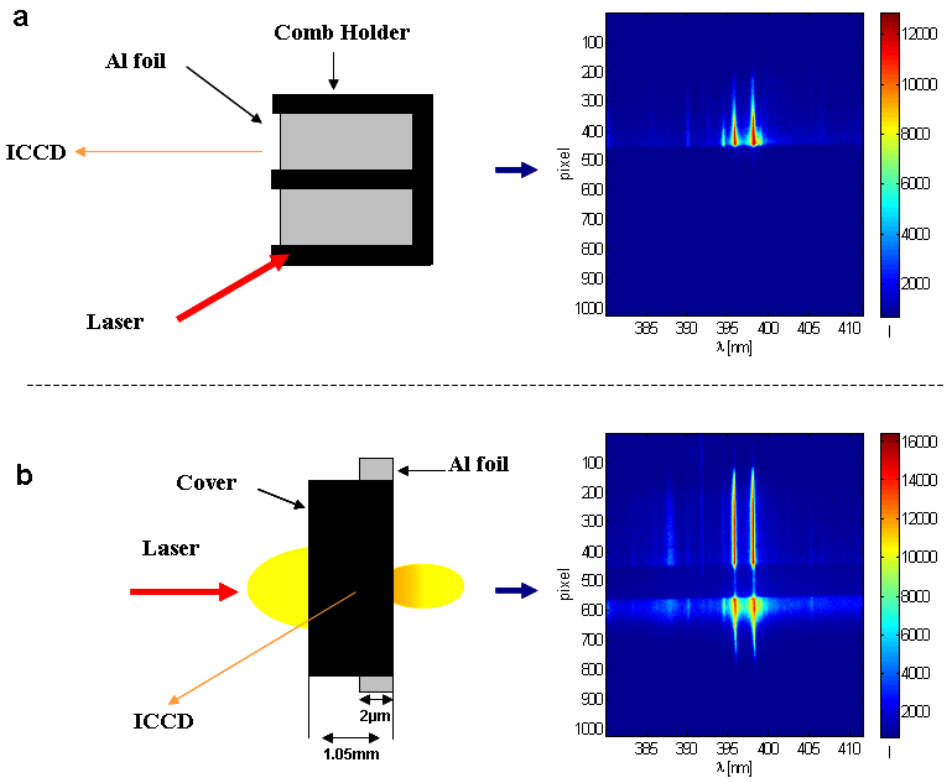

Figure 4.3.5: *Schematic diagram of the configurations used to investigate the contribution of reflections to the spectra presented previously. In (a) a plasma was formed on the target holder (rather than on the Al foil) and in (b) a mechanical block was employed to obscure the front plasma. The related spectra shows no back-plasma by firing on the holder, and by placing the cover on the front plasma to avoid reflections plasma emission from the rear side of the foil is still observed (identical to when no cover is used).*

4.4 Conclusions

Measurements reported in this chapter permitted to characterize the plasma dynamics produced from thin Al targets in the low laser energy domain.

Time resolved imaging permits the detection of the expansion of both the stagnation layer and the backward plasma. Most of the plasma propagates in the forward direction, however, it appears that in this laser irradiance regime the intensity is not sufficient to produced the more widely studied thin foil-laser interaction, shown in figure 4.1.1. This is not completely unexpected as the energy transferred to the plasma, differs greatly with respect to the case of femtosecond lasers. A back-flowing plasma with a very slow dynamics (comparable in time to that of the stagnation layer) is observed. It is mainly composed of neutral atoms and electrons, that blow off from the target after the foil explosion.

This was also confirmed by the LP measurements, as the main bunch of electrons reach the probe at a velocity of $v = 2.27 \cdot 10^3 m/s$. This velocity is one order of magnitude lower than the typical LPP velocities obtained at the same laser fluence on forward expanding plasmas. Despite the fact that the back plasma has a slow dynamics, the back-plasma is also less dense than the forward-flowing one.

The results presented here are just a preliminary analysis of the wealth of information collected for this target configuration, it is still conceivable that the expansion processes studied in this chapter could find some future applications in the investigation of ES.

Chapter 5

Modelling of an Al plasma expanding in vacuum

In this chapter the numerical code used to simulate the bulk plasma propagation of the Al plume will be described. The numerical results will be then compared with experimental data.

5.1 Introduction

As mentioned in chapter 1, the Anisimov analytical model solves the Eulers gas dynamical equations (1.8.7) in order to reproduce the plasma core expansion. The basic hypothesis of the model are that the plasma flow expands selfsimilarly, adiabatically and isoentropically in vacuum. One of the main advantages of Anisimov's approach is that numerical results can be directly compared to the experimental data, such as plasma density and plasma temperature. It is clear that the use of an analytical model presents some limits, that can be overcome by using a kinetic approach, i.e solving

the Vlasov equation.

However, as observed also by other authors [80, 37, 38] the Anisimov's model well describes the real plume expansion if the initial simulation conditions are setted properly, relating them strictly to the real experimental conditions (initial plasma temperature, crater depth etc.) [5].

On this purpose we implemented the model in a Matlab® code using the $ODE45$ routine based on the Runge-Kutta method, obtaining the time-varying plasma density distribution, in the $1D$, $2D$ and $3D$ space coordinates. Two additional input parameters were introduced to the model, including the effect of the accelerating Coulomb field and the difference between the ion and the electron temperatures. These improvements permitted us to successfully compare the numerical results with the Langmuir probe measurements realized on the Al expanding plasma reported in chapter 2.

5.2 The Anisimov Model

The Anisimov model provide to a special analytical solution of the equations 1.8.7 assuming a non constant temperature of the bulk plasma during its expansion.

On this purpose, let us consider the coordinates of a fluid particle r_i $(i = x, y, z)$, that can be described in the form 5.2.1:

$$r_i(t) = \sum F_{ik}(t) r_k(0) \tag{5.2.1}$$

where $r_i(0)$ are the initial coordinates.

Equation (5.2.1) describes the motion of r_i moving from $(x(0), y(0), z(0))$ at $t = 0$ to $(x(t), y(t), z(t))$ at a fixed time t (see fig.5.2.1).

The matrix F_{ik} describes the expansion and the rotation of the particle,

but in the Anisimov model the rotation of the particles is ignored so that the matrix is reduced to the diagonal form 5.2.2 [36]:

$$F_{ik}(t) = \begin{pmatrix} X(t)/X_0 & 0 & 0 \\ 0 & Y(t)/Y_0 & 0 \\ 0 & 0 & Z(t)/Z_0 \end{pmatrix} \tag{5.2.2}$$

where X_0, Y_0, Z_0 are the initial values of $X(t), Y(t), Z(t)$. The initial coordinated X_0, Y_0 and Z_0 are determined by the radius laser spot R_0 (see figure 5.2.1) and the z-axis represents the expansion direction normal to the target surface.

Z_0 is approximated to $v_s\tau_l = 0.01 \cdot T/A$, where v_s is the sound velocity and τ_L is the laser pulse length, T the initial plasma temperature in eV and A the atomic mass number. that is supposed much more smaller than the time expansion t_0. The time of expansion is determined by $t_0 = R_0/\sqrt{\beta}$ where β describes the velocity of the plume by means of the important relation:

$$\beta = (5\gamma - 3)\frac{E}{M} \tag{5.2.3}$$

Substituting the (5.2.1) in the (1.8.7) we obtain a set of ordinary differential equations for the elements of matrix (5.2.2). The transformation can be carried out only for some particulary densities and pressures profiles which special solutions are described by the equations 5.2.4, existing thanks

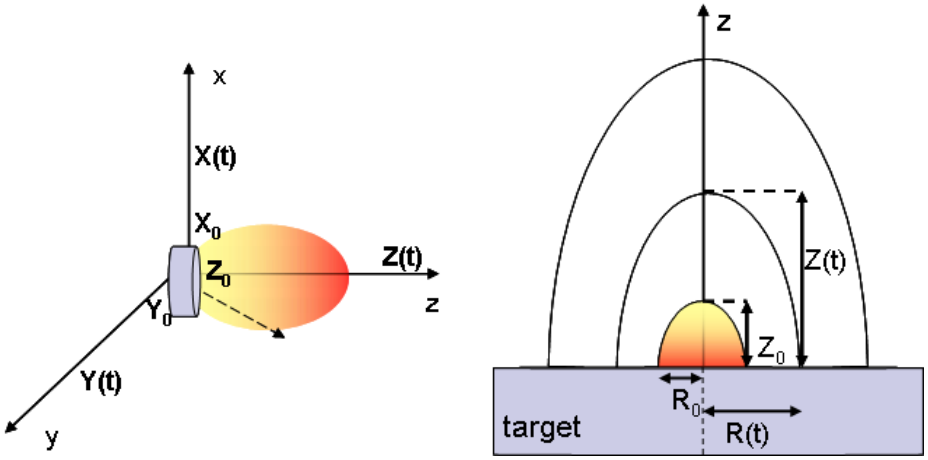

Figure 5.2.1: *Later and frontal view of the plasma plume expansion*

to the Lie group transformation theory [36]:

$$\begin{aligned}
\rho(x,y,x,t) &= \frac{M}{I_1 X(t)Y(t)Z(t)}\left(1-\frac{x^2}{X(t)^2}-\frac{y^2}{Y(t)^2}-\frac{z^2}{Z(t)^2}\right)^{\frac{1}{\gamma-1}} \\
P(x,y,x,t) &= \frac{E}{I_2 X(t)Y(t)Z(t)}\left(\frac{X_0Y_0Z_0}{XYZ}\right)^{\gamma-1} \\
&\quad \times\left(1-\frac{x^2}{X(t)^2}-\frac{y^2}{Y(t)^2}-\frac{z^2}{Z(t)^2}\right)^{\frac{1}{\gamma-1}}
\end{aligned} \tag{5.2.4}$$

where M is the plume mass and E is the plume energy given respectively by the formulas:

$$M = \int_V = \rho(x,y,z)dV) \tag{5.2.5}$$

$$E = \frac{1}{\gamma-1}\int_V p(x,y,z,0)dV \tag{5.2.6}$$

The expressions for I_1 and I_2 can be described by the equations 5.2.7

$$I_1(\gamma) = 2\pi \int_0^1 s^2(1-s^2)^{\frac{1}{\gamma-1}} ds \tag{5.2.7}$$

$$I_2(\gamma) = \frac{2\pi}{\gamma-1} \int_0^1 s^2(1-s^2)^{\frac{1}{\gamma-1}} ds \tag{5.2.8}$$

ρ and P are constant at the ellipsoidal surfaces $\frac{x^2}{X(t)^2} + \frac{y^2}{Y(t)^2} + \frac{z^2}{Z(t)^2}$. The temperature that can be simulated by the formula 5.2.9 [81]:

$$T(x,y,x,t) = \beta \frac{\gamma-1}{2\gamma} \frac{M}{k_B} \left[\frac{X_0 Y_0 Z_0}{X(t)Y(t)Z(t)}\right]^{\gamma-1} \left(1 - \frac{x^2}{X(t)^2} - \frac{y^2}{Y(t)^2} - \frac{z^2}{Z(t)^2}\right) \tag{5.2.9}$$

Equations (5.2.4) and (5.2.9) describe the plume expansion with a **sharp external edge**. This is a consequence of the assumed entropy conservation which leads to $T \infty \rho^{\gamma-1}$. Thus at the front, **the plume density, the temperature and the velocity tend to zero**. This is in contrast to the assumptions of an isothermal model where the velocity differs from zero and edges generates density and pressure tails.

Another important theoretical assumption of the model is that the kinetic energy of the vapor flow near the target surface is supposed to be much smaller than the vapor flow thermal energy. This last hypothesis determines that $\dot{X(0)} = \dot{Y(0)} = \dot{Z(0)} = 0$. The initial energy of the plasma plume can in this case be determined by equation 5.2.10:

$$E = E_\alpha - M\Delta H_v \tag{5.2.10}$$

where $E_\alpha = I_\alpha \tau_L$ is the absorbed laser light and ΔH_v s the enthalpy of vaporization.

The final assumption of a axial symmetry leads to $X(t) = Y(t)$, so that the expansion can be described only by the set of coordinates $[X(t), Z(t), \dot{X(t)}, \dot{Z(t)}]$, (see fig. 5.2.1).

Introducing a set of dimensionless variables:

$$\tau = \frac{t}{t_0};\ \xi(\tau) = \frac{X(t)}{R_0};\ \ \eta(\tau) = \frac{Y(t)}{R_0};\ \sigma(\tau) = \frac{Z(t)}{R_0}. \tag{5.2.11}$$

The equations of motion of the plasma front become:

$$\xi\ddot{\xi} = \eta\ddot{\eta} = \left[\frac{\sigma}{\xi^2\eta}\right]^{\gamma-1} \tag{5.2.12}$$

Initial conditions are:

$\xi(0) = 1;\ \eta(0) = \sigma;\ \dot{\xi}(0) = \dot{\eta}(0) = 0.$

$\xi(\tau)$, $\eta(\tau)$ are both linear function of τ when $\tau \to \infty$. This last condition determines that the expansion becomes inertial as the pressure gradient tends to zero. The sharp edges of the pressure and density profiles at the front at which the density is equal to zero, means that the temperature at the edge approaches zero as well.

Equations (5.2.12) have been solved numerically using a fourth order calculation Runge-Kutta Nystrm method by using a Matlab® code developed in collaboration with Mascali et al. as reported in [2].

The model is considered to be a good approximation for the description of monoatomic plumes produced at low laser energies expanding in vacuum. However, the evolution of the plasma is considered without no distinction between the plasma charged particles, i.e ions and electrons. In order to overcome this limit, we improved the model by including additional simulation parameters.

5.3 Code improvements

As we studied in section 1.8, the core plume dynamic is strongly influenced by Coulomb electric field E'. To take into account such effect, in the theo-

retical plasma expansion, we added to the our numerical code the Coulomb velocity term v_c given be equation 1.8.3.

Such contribution was obtained by adding v_c to equation 5.2.12 as follows [6]:

$$\xi_{shifted} = \xi + v_c = \xi + \sqrt{\frac{2 < z > eV_p}{M}} \frac{R_0}{t_0} \tag{5.3.1}$$

The Coulomb accelerating potential can be roughly estimated by the electron temperature, according to the formula $V_p = ck_BT_e$ where the constant lies usually in the range $1 \div 4$ [22]. From thermodynamics considerations Kelly calculated the velocity of the adiabatic expansion, which is related to the electron temperature by the equation [82]:

$$v_\gamma = \sqrt{\frac{\gamma k_B T_e}{M_i}} \Longrightarrow T_e = \frac{M_i v_\gamma}{\gamma k_B} \tag{5.3.2}$$

Therefore, assuming a value of γ and once known v_γ we can extrapolate from the above equation the initial electron temperature T_e. We can numerically determine the expansion velocity by means of equations 5.2.12 (their solution, in fact, do not depend on the initial temperature); anyway, it must be depurated by the Coulomb drift term. Conversely the v_c term plays a role in determining the ion temperature, according to the following scheme [6]: first electrons-ions collisions heat the ions thus equalizing T_i and T_e. Then the Coulomb and adiabatic components of the expansion velocity give to the ions a high translational energy (which approximately corresponds to the high electrons velocity). Due to the the high collisional rate, ions share the ordered, forward peaked energy changing it into disordered, thermal energy. The ion temperature will consequently be of the same order of magnitude of the expansion velocity:

$$\frac{3}{2} k_B T_i \approx \frac{1}{2} M v_{exp}^2 \tag{5.3.3}$$

where v_{exp} denotes the total expansion velocity. By taking into account equations 5.3.2 and 5.3.4 the ion to electron temperature ratio will be:

$$\frac{k_B T_i}{kT_e} = \frac{1}{3}\left[\sqrt{\gamma} + \sqrt{2 < z >}\right]^2 \tag{5.3.4}$$

To some extent, this relation can be seen also as the temperature ratio dependence on a given charge state inside a single plume. It predicts not only that the ion temperature is consistently higher than the electron one, but also that the ratio grows with the charge state, that is in perfect agreement with experimental data [59]. Using equation 5.3.4 the Anisimov model has been further improved by introducing the discrepancy between the ion and electron temperature. Two γ factors have been also introduced, one for electrons (γ_e) and the other one for ions (γ_i) [5, 6]. This assumption is valid for monoatomic low temperature plasmas, for which the adiabatic index lies in the range of 1.1 to 1.4 [38]. Because of excitation and recombination processes, the plasma degrees of freedom can be reduced; hence a γ value lying in the range indicated above is more appropriate than $\gamma = 5/3$. Also cluster formation can affect the γ value; this effect is is discussed in detail in [83]. Thanks to these "tricks", the model became effectively a two-fluid-like approach.

5.4 Multi dimensional Al plume simulations and comparison with experimental data

The Anisimov model permits to calculate the $2D$ and $3D$ plasma density distribution vs. time: because of the $X - Y$ symmetry, bidimensional and threedimensional density mapping can be easly numerically simulated. On this purpose, in figure 5.4.1 the $3D$ Al plume is reported for four different

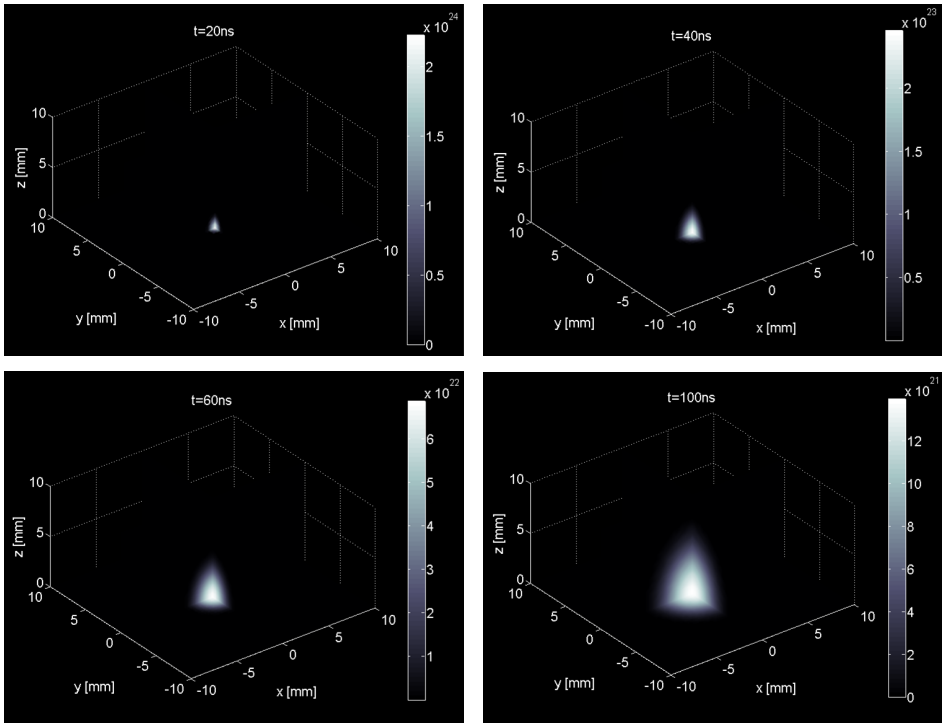

Figure 5.4.1: *3D simulation of the Al plume in terms of density at different expansion stages:* $t_1 = 20ns$, $t_2 = 40ns$, $t_3 = 60ns$ *and* $t_4 = 100ns$.

expansion times, namely $t_1 = 20ns$ to $t_2 = 40ns$, $t_3 = 60ns$ and $t_4 = 100ns$.

As we can observe from the figure the plume rapidly expands in volume and the density rapidly decreases of several order of magnitudes after $100ns$. Here the plume expansion was simulated by a *mesh routine* that interpoles the density value in each numerical cell with the nearest cell at the isosurfaces. Figures 5.4.1 show the plume propagation overall the x, y, x plane, however $2D$ simulations vs. times result more useful to be better interpret the plume expansion in terms of density and temperature distribution, as we shown in figure 1.8.6 [5].

In a similar way, by using equation 5.2.9, the $3D$ temperature can be

simulated. Results are reported in figure 5.4.2.

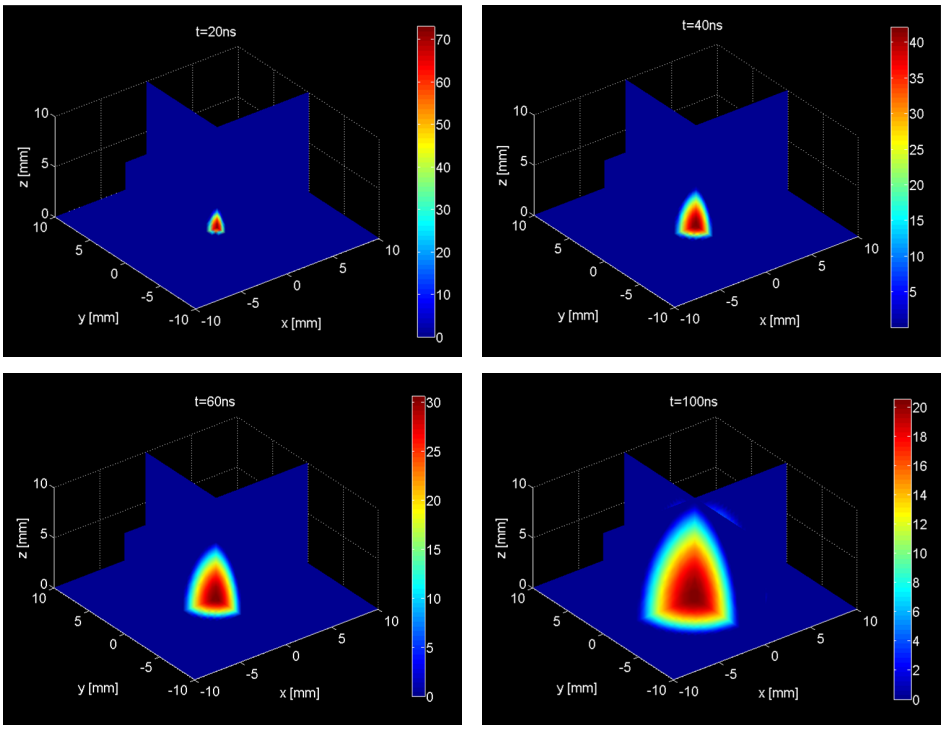

Figure 5.4.2: *3D simulation of the Al plume in terms of temperature at different expansion stages:* $t_1 = 20ns$, $t_2 = 40ns$, $t_3 = 60ns$ *and* $t_4 = 100ns$.

Also the temperature trends show the adiabatically decrease of the temperature values vs. time, that helps us to understand why with different diagnostic tools, different plasma parameters are obtained. On this purpose, in figure 5.4.3, the $2D$ simulated temperature for an Al plume is reported at the fixed time expansion $t = 120nsec$. T_{th} trend rapidly decreases spatially at a fixed time, giving a temperature on the order of $T_e = 16eV$ for the core plasma and of $T_e = 3 - 4eV$ for the coronal plasma.

Results reported in these pages can be compared with experimental results collected in chapters 2 and 3.

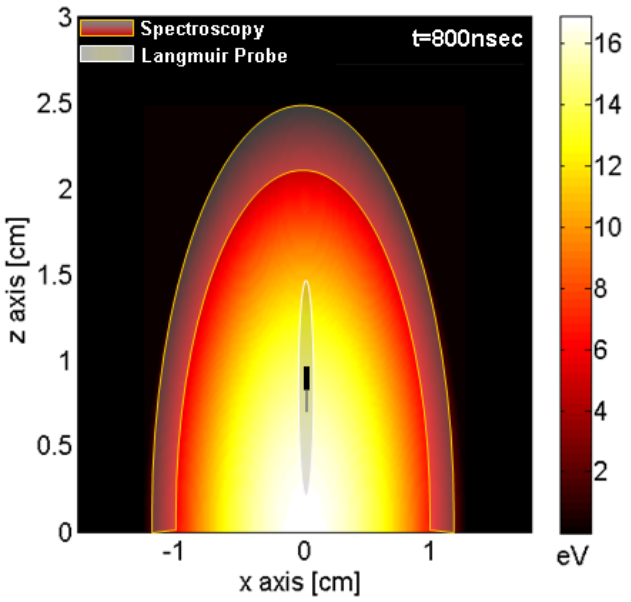

Figure 5.4.3: *2D simulation of the Al plume in terms of plasma density at a fixed time expansion; the area in which the probe is located indicates the experimental region where LP measurements were made; the area of the coronal plasma was instead investigated experimentally by time resolved spectroscopy.*

The plasma shape can be compared with CCD images obtained with the single seed; it is correctly reproduced by the simulations, being semi-ellipsoidal during all the expansion time. Spectroscopy measurements give $n_e = 2 \cdot 10^{25} m^{-3}$ at $t = 100ns$, that is higher than the simulated one at the same instant, which can be estimated from figure 5.4.1 to be equal to $1.2 \cdot 10^{22} m^{-3}$. On the other hand, measurements with the LP give $n_i = 1 \cdot 10^{19} m^{-3}$ at $t = 100ns$ and at $4.5mm$ far away from the target surface. At the same instant and in the corresponding position, the simula-

tions give a density around $\rho = 1 \cdot 10^{20} m^{-3}$. About the temperature at the same expansion stages, spectroscopy gives $T_e = 2.5eV$, while the LP gives $T_e = 10 \div 18eV$, which are lower or higher than the simulated one depending on which spatial part is considered in figure 5.4.2 for the simulated plume at $100ns$. Differences between the experimental temperatures evaluated with the two different experimental techniques can be explained by figure 5.4.3: the LP collects the charge of the plasma core, hence measuring temperatures on the order of $10 - 20eVs$, while spectroscopy in the visible region refers to the investigation of the coronal plasma, hence measuring temperatures on the order of few eVs as reported in chapter 3. Differences on the electron density are more difficult to explain; the simulated density is closer to the spectroscopy measurements at the earlier stage of the plume expansion whereas it is closer to the density coming out from LP measurements at later expansion stages. These discrepancies maybe due to the different theoretical assumptions made for data analysis with the two different techniques: spectroscopy is more reliable as long as LTE is valid, while the LP theory fails in case of a strong collisional plasma.

In order to make a more precise comparison between experimentally collected data and the simulated ones, we performed $1D$ calculations, reproducing a virtual probe located at given distances from the target surfaces (see figure 5.4.3). TOF signals can be reconstructed, and then directly compared with the experimental ones. This method was applied in [5], where n_e and T_e obtained experimentally by means of LP measurements from a Ta plasma were compared to the simulated ρ and T_{th}. By introducing the Coulomb shift term it is moreover possible to simulate the different charge states of the plasma plume. This work was performed in [4] for an Ag plasma,

were the different charge states were weighted in the plasma composition by means of IEA spectra that permitted us to estimate the percentage, in terms number of plasma particles, for each charge state z_i and hence to simulate the correspondant TOF signals $I(z_i)$. The ion signal obtained from the convolution of all total time of flights signals $\sum_i I(z_i) = I_i$ was then compared successfully to the experimental TOF signal of the Ag plasma. Similar approach was used to simulate the expansion of the Al plume in terms of plasma parameters and current signals obtained in chapter 2 and reported in [6]. Once fixed the position of the virtual detector, the ion or electron current I_i and I_e can be simulated by the formulas 5.4.1, by applying the Koopmann theory described in section 1.11.1:

$$I_i^S = e(v_\gamma + v_c + v_{th})\rho_{th}A_p \tag{5.4.1}$$

$$I_e^S = e(v_{th})\frac{\rho_{th}}{z}A_p exp\left[\frac{e(V_p - V)}{k_B T_e}\right] \tag{5.4.2}$$

where v_γ, v_c and $v_{th} = \sqrt{(k_B T_e)/(2\pi m_e)}$, are respectively the flow, the coulomb and the thermal velocity. A_p is the probe area seen by the plasma, V_p is the plasma potential and V the potential applied to the probe. Note that for the simulation of the total current signal $I_i + I_e$, z assumes the value of the mean charge state of the plume $< z >$, that for the simulation of the Al plasma was supposed to be $< z >= 4$, because of the high laser fluence. Equation 5.4.1 is valid as long as the virtual probe operates in the ion saturation current regime, otherwise the electron contribution to the current must be included by means of 5.4.2. The comparison between the experimental data and the simulation results are reported in figure 5.4.4 Calculations are able to reproduce only the plasma core signal, provided that the initial simulation parameters reported in table 5.4 are used. They reasonably pre-

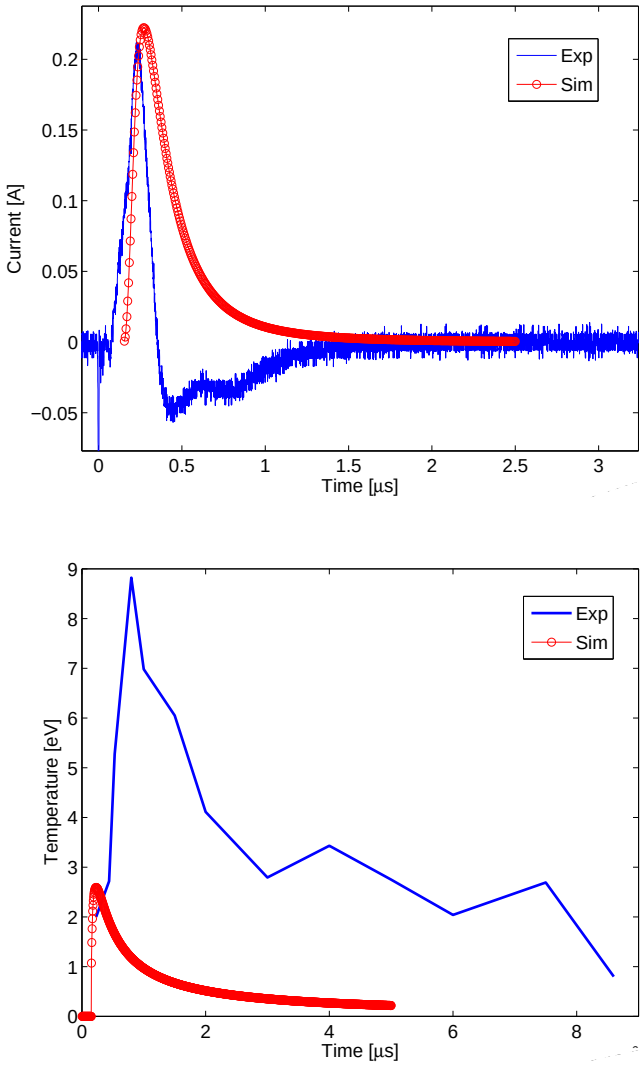

Figure 5.4.4: *Up - Langmuir probe signal detected at* 14.5*mm from the target compared with the simulated one. Down - Measured electron temperatures as function of the time in comparison with simulated one at the same position*

Table 5.1: Simulation Parameters related to the experimental conditions.

E	$30mJ$
Crater depth	$9\mu m$
Crater diameter	$100\mu m$
Laser Fluence	$2000J/cm^2$
Electron Temperature	$80eV$
Plasma Potential	$21V$
Constant c	2.9

dict the width and the centroid position of the detected signal, but not the tail, where a strong contribution from negative charges seems to be present. Hot electrons produced by the recombination mechanisms maybe the cause of this strong tail depletion as discussed in chapter 2. The fast peaks of the real signal eventually present at the early stage of the plume expansion (especially when the probe is located closer to the target surface), cannot be simulated with the Anisimov model as discussed in detail in chapter 2. This is a further confirmation of their different nature: they do not obey to fluidodynamics because their formation mechanism is strongly different with respect to the remaining part of the plasma.

5.5 Preliminary calculations of Nuclear Reaction Rates

The improvements introduced in the Anisimov model permitted us to better reproduce the adiabatic dynamics of the core plasma taking into account the *Coulomb acceleration* term and the discrepancy between the ion and the

electron temperature (including two different γ expansion values [6, 5]); in this way the model became effectively a two-fluid-like approach ($T_i \neq T_e$). To have a reliable model which correctly reproduce the trends of density and temperature it is of primary importance for future reaction rate measurements. Since the ES is not directly measurable, only by comparing the experimental fusion rates with the expected, simulated numbers (with and without screening) will be possible to determine how large is the ES influence. Strictly speaking, we deem that it is not possible to extract exact values of ES from a single measurement at a given fluence. More properly, the experiment will consist is a series of measurements at different fluences (scaling from low to high values), comparing them with calculations, and finally extracting the ES comparing the trend of fusions numbers with the expected ones without the ES: the ES will come from a sort of "excitation function", providing a reliable result. On this purpose we realized some preliminary numerical calculations in order to evaluate the ES effect and the nuclear reaction rates in LPP (they are reported in [7]). We used the Anisimov model to determine the initial conditions of the plasma plume in terms of density and temperature by using equations (5.2.4) and (5.2.9). The electron screening was calculated according to the well-known Debye-Huckel formula [84]:

$$U_e = exp\left(\frac{Z_1 Z_2 e^2}{k_B T \lambda_D}\right) \tag{5.5.1}$$

where Z_1 and Z_2 are the integral nuclear charges of the interacting particles. For the above reported calculations, an updated version of the numerical code permitted us to evaluate the $3D$ ES. A virtual CD_2 target was used for the simulations.

In figure 5.5.1 the $3D$ evolution of ES is shown. We observe that the

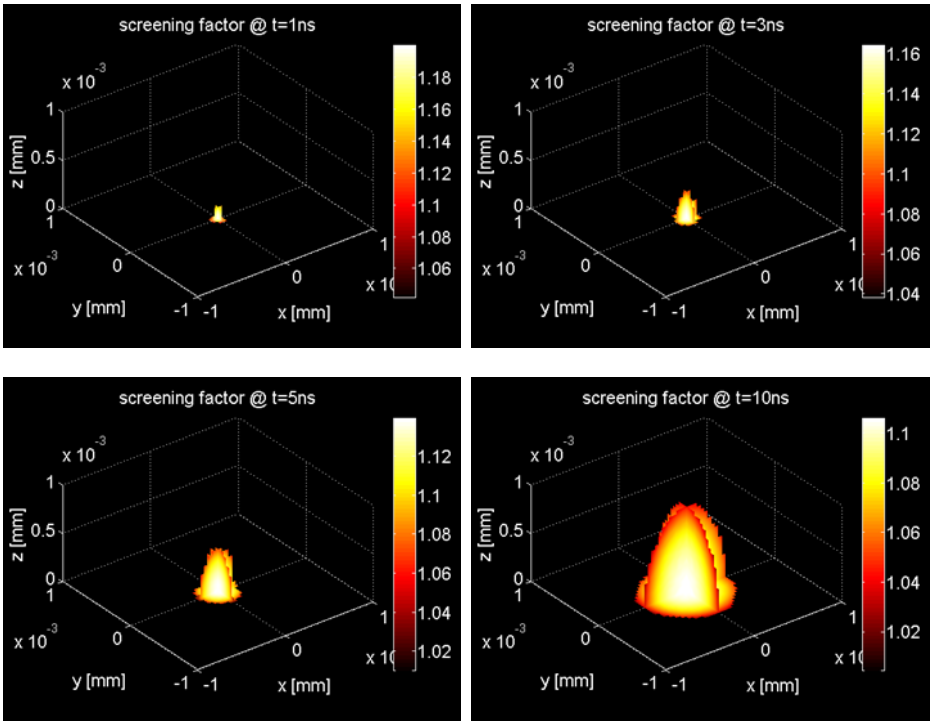

Figure 5.5.1: *3D calculation of the screening at different times after the laser shot[7].*

screening factor smoothly varies either in time and along the spatial coordinates; this occurs because the ratio between the plasma density ρ and the plasma temperature T remains almost unvaried, although ρ and T rapidly drop during the adiabatic plasma expansion. The fusion reaction rate was determined by applying the Gamow theory, using equation [1]:

$$R = \frac{1}{2} N < \sigma v > \int_0^\infty \rho(t) dt \tag{5.5.2}$$

where N is the total number of particles, $\rho(t)$ the plasma density, and $< \sigma v >$ is the reactivity, i.e the effectiveness of a fusion fuel given by the

formula [1].

$$< \sigma v >= \left(\frac{8}{\pi\mu}\right)^{\frac{1}{2}} \left(\frac{1}{kT_i}\right)^{\frac{3}{2}} \int_0^{\infty} \sigma(E) E \cdot exp\left(-\frac{E}{kT} - \frac{b}{\sqrt{E}}\right) dE \quad (5.5.3)$$

where T_i is the ion temperature, $\sigma(E)$ is obtained by the Gamow theory taking in account the tunnel effect of the nuclear coulomb barrier [1]:

$$\sigma(E) = \frac{1}{E} \cdot exp\left(-2\sqrt{\frac{E_G}{E}}\right) S(E) \quad (5.5.4)$$

$E_G = \sqrt{0.989 Z_1 Z_2 \mu} MeV$ is the *Gamow energy* and $S(E)$ is the astrophysical factor [1]. Note the R dependency from ρ and T_i, and the ES dependency from n_e and T_e, as discussed above.

Fusion reaction rates calculations are reported in figure 5.5.2. They were evaluated with and without the influence of ES. The figure 5.5.2 reveals that if the laser is operated in the repetition rate mode ($10Hz$), after 24 hours the accumulated number of fusion is increased of a factor 1.2 by the electron screening. Note that almost the totality of the fusion events takes place in the first $2 - 3ns$ after each laser pulse.

5.6 Conclusions

The above proposed model is able to correctly reproduce the dynamics of a plasma dominated by collisions and in local thermal equilibrium. Hydrodynamics fails in the case of strong non-linearities, or when high electric field are present in the first instants of plume expansion. If the initial conditions are set properly, the Anisimov model well reproduced the plume

[1] A projectile with energy $E < E_C$, with E_C Coulumb energy has a certain probability to tunnel the potential barrier

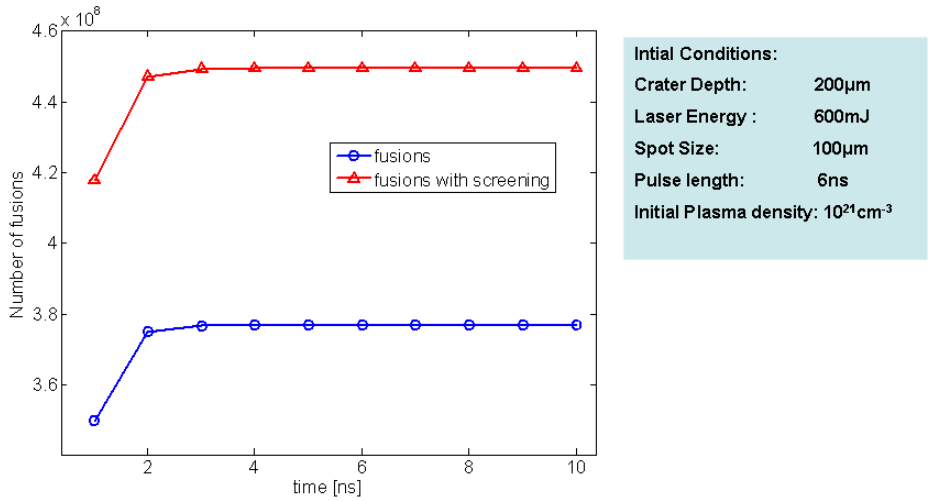

Figure 5.5.2: Cumulated number of fusions after 24h of operations in laser repetition rate (10 Hz) mode versus the time after each laser shot.

dynamic. It is also important to emphasize that the theoretical temperature 5.2.9 was defined by Anisimov as the "plasma temperature". By our improvements the model became effectively a two-fluid-like approach. Another consideration about the plasma temperature must be done; we know that the adiabatic expansion undergo at a certain time of the plume propagation into free streaming. The free streaming is not taken into account in the Anisimov model. Hence a more detailed analysis is needed in order to investigate where and when the adiabatic expansion stops, with the following influence on the plasma temperature evolution. This can be done by comparing the theoretical temperature with the experimental temperatures values, by fixing the virtual probe position at the same position of the real detector. If, in first approximation, no correspondence is found between the experimental and numerical temperature, the virtual probe must be located

closer to the target surface, at a different position respect to the real one. When the position in which a good agreement between the real temperature and the simulated temperature is found, this position can be considered as the distance from the target surface were the adiabatic expansion stops and the free flight begins. This method was applied to a Ta plasma and is discussed in detail in [5] where the adiabatic expansion was found to end at $4.5mm$ from the target.

Summing up, the simulations reproduced quite well the plasma dynamics, at least in terms of order of magnitude for electron density and temperature. They served also to adequately calculate the expected fusion rates and the contribution of the ES. It resulted that with the parameters experimentally used in our apparatus, ES may play a role in determining the total number of fusions, being its weight on the order of 20%.

Chapter 6

Conclusions and Perspectives

6.1 The nanosecond laser energy regime: interface between two different plume dynamics

In this work the temporal dynamics of LPP in the ns range pulse length have been largely investigated through numerical simulations and different diagnostics techniques. The employed power intensity is somehow at an intermediate level between the low intensity, ns laser ablation domain (up to $10^9 \div 10^{11}\ W/cm^2$) and the operations at extreme intensities with fs lasers ($10^{18} \div 10^{20}\ W/cm^2$).

We observed non linear and single particle effects (i.e. not describable by any fluids model): at fluence regimes of $2 \cdot 10^3\ J/cm^2$ we experimentally observed the appearance of a new mechanisms, leading to the formation of non-neutral plasma regions which induce a large potential drop, causing very strong electric fields; the theoretical approach evidenced the possible formation of DL - double layers, or even multiplicity of non-neutral layers. These fast bunches evidenced non-classical dynamics; we were able to de-

scribe them by a simple electrostatic model with some approximation, i.e. as a sum of charged expanding layers self interacting each other. Preliminary simulations have shown that the layers' acceleration is more due to the self-coulomb interaction among the positive layers rather than to the attractive force due to the escaping fast electrons. About this last point, we observed fast electrons emitted with velocities up to $10^5 m/s$, followed by accelerated ion bunches presumably formed of different charge states travelling with energies up to $4-5\ keVs$. Their expansion dynamics expired within $100ns$, and can be summarized schematically as reported in figure 2.4.1. The electric field which develops during the expansion of electron and ion bunches is very high: by fitting the acceleration of the various layers with the numerical model developed in section 2.3.3, it results of the order of $E_{DL} = 3 \cdot 10^7\ V/m$ in the first $20ns$, then rapidly decreasing to zero within $100ns$. Considerations about the source of the instabilities which produces this fragmentation mechanism are connected to the so called Two-Electron-Temperature (TET) plasma. Analysis of the two temperatures T_{hot}/T_{cold} vs time indicates that rarefaction shock waves may be originated, that formally is a DL. There are not enough data to definitely say whether or not the shock was really formed, or if the fragmentation is due more to the fast expansion of the initially accelerated electrons; the particles which get energy directly from the laser and go away from the target surface in a time comparable to the laser pulse duration, in fact, may leave a background positive medium which finally explodes producing the observed multiplicity of layers, as confirmed by the model reported in section 2.3.3. Additional investigations will be needed to clarify this complex mechanism: a) how it is definitively generated, b) what influence it has on the possible employment of such plasmas

for astrophysical studies. According to the preliminary calculations reported in section 5.5, concerning the fusion reaction rate and the role played by the ES, plasma instabilities should be damped. Otherwise, the contribution to the total number of fusions due to not-handled nonlinearities cannot be correctly evaluated, and we would be not sure of the correct determination of the screening contribution to the total rate.

We also characterized the bulk plasma propagation. Another electric field was found out, which additionally regulates the velocity of the core into the vacuum. This field is formally similar to the one generated inside the sheath established between a plasma and an absorbing wall (also called "plasma potential") like a metallic vessel. The absorbing wall is, in the case of LPP, the vacuum. The electric field with maximum value of $E_{bulk} = 1.4 \cdot 10^7 V/m$ arises in order to accelerate the ions and decelerate the electrons, as a consequence of the different mobility of these two species. This was the field component introduced into the fluid equations in chapter 5 to adequately fit the experimental data (coulomb acceleration term).

Measurements on colliding plasmas permitted us to characterize the stagnation layer in terms of electron density and electron temperature. Data analysis confirmed that the electron density of the stagnation layer has a slower expansion dynamics with respect to the single plume. This could result very useful to study the ES, since electron populations with high density, but very low temperature are required. Some measurements were already done with colliding plasmas by using thin Al foils, reported in chapter 4: the peculiarities of the laser fluence regime influenced the formation mechanism of the plasma; the main plasma is still forwardly peaked, but a slow and less dense plasma was formed on the target's back-side. The backward flowing

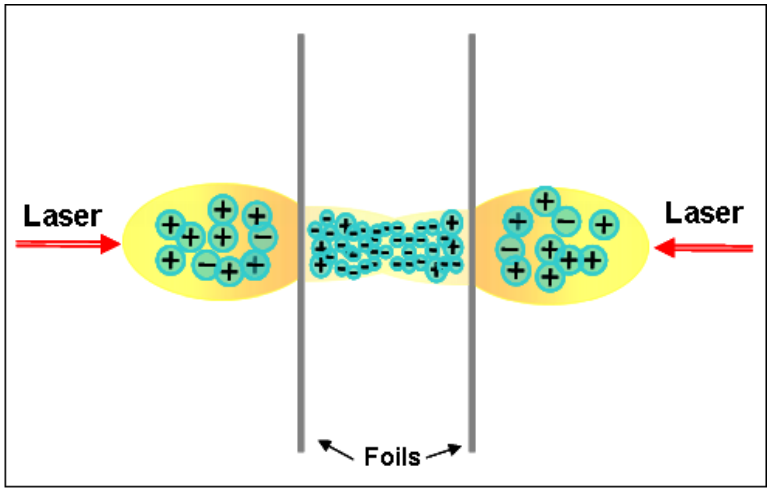

Figure 6.1.1: *Possible scheme of Backward Plumes Collision in order to study the Nuclear Screening.*

plasma can be interpreted like a blow-off of neutral atoms and electron, having a similar dynamic to the stagnation layer one. This could lead also to a possible ES study during the collision of the two backward plasmas plumes, as shown in figure 6.1. In our fluence regime we should be able to reproduce a cloud enriched of cold electrons, which stagnates for very long times. It is in fact expected that, due to the slow electron dynamics ($v \sim 10^3 m/s$), collision will occur at later times, allowing the electron adiabatic cooling before the plumes interaction.

The expansion dynamics of the plasma cloud was successfully described by analytical, fluids-dynamical models at very low intensities by including effects of self-generated electric fields (Coulomb term in the Anisimov model) to successfully describe the behavior of the plasma core and to perform some preliminary fusion reaction rates measurements. The calculated screening factor is very similar to the stellar ones [1] and the collected data

put in evidence that an experiment with a deuterated target, and 4π detectors for fusion products like neutrons, is possible and physically meaningful; the strong temporal concentration of the significative events will help to adequately trigger the acquisition system, improving the experimental precision. The forecasted experiment will give the opportunity to calculate the electron screening in a stellar-like environment, to test the validity of the classical Debye-Huckel theory and finally to evaluate the astrophysical factor at energy domains of the order of hundreds of eV, never explored up to now by nuclear astrophysics [7].

References

[1] E. Rolphs. *Cauldrons in Cosmos*. Universty of Chicago Press, 1998.

[2] D. Mascali, S. Tudisco, A. Bonanno, N. Gambino, S. Ivanovski, A. Anzalone, S. Gammino, R. Miracoli, and F. Musumeci. Colliding laser-produced plasmas: a new tool for nuclear astrophysics studies. *Rad. Eff. and Def. in Solids*, 165(6), 2010.

[3] N. Gambino, A. Anzalone, A. Bonanno, S. Gammino, D. Mascali, F. Musumeci, D. Leanza, R. Grasso, L. Neri, S. Privitera, A. Scordino, A. Spitaleri, and S. Tudisco. Studies of astrophysical plasmas in laboratory by laser ablation. Internal, LNS-INFN, 2009.

[4] N. Gambino, D. Mascali, R. Miracoli, S. Gammino, D. Margarone, F. Musumeci, S. Tudisco, and L. Torrisi. Comparison between time of flight measurements and numerical simulations for laser generated plasmas. *Rad. Eff. Def. in Solids*, 165(6), 2010.

[5] N. Gambino, D. Mascali, R. Miracoli, S. Gammino, D. Margarone, and L. Torrisi. Comparison between langmuir probe measurements and hydrodynamic simulations for laser generated plasmas. *Submittet to J. Appl. Phys.*

[6] S. Tudisco, D. Mascali, N. Gambino, A. Anzalone, S. Gammino, F. Musumeci, A. Scordino, and A. Spitaleri. Determination of the self generated electric field in a laser produced plasma at high fluence. *Nucl. Instrum. A*, *In press.*

[7] D. Mascali, N. Gambino, S. Tudisco, A. Anzalone, A. Bonanno, S. Gammino, and F. Musumeci. Calculation of fusion rates at extremely low energies in laser plasmas. *Proceedings IAU Symposium, 2-6 September 2010.*, *In press.*

[8] T.P Hughes. *Plasmas and Lasers Light.* Adam Hilger, 1975.

[9] M. P. Kalashnikov, P. V. Nickles, Th. Schlegel, M. Schnuerer, F. Billhardt, I. W. Sandner Will, and N. N. Demchenko. Dynamics of laser-plasma interaction at 10^{18} w/cm^2. *Phys. Rev. Lett.*, 73(2):260–263, 1994.

[10] T. Tajima and J. M. Dawson. Laser electron accelerator. *Phys. Rev. Lett.*, 43(4):267–270, 1979.

[11] H. Alfvén. Existence of electromagnetic-hydrodynamic waves. *Nature*, 150:405–406, 1942.

[12] I. Langmuir. Oscillations in ionized gases. *Proc. Nat. Acad. Sci. U.S*, 14:628, 1928.

[13] I. B. Bernstein. Waves in a plasma in a magnetic field. *Phys. Rev. Lett.*, 109(1):10–21, 1958.

[14] F. Chen. *Introduction to Plasma Physics and Controlled Fusion.* Springer, 1984.

[15] J. D. Callen. Draft material for "fundamentals of plasma physics" book. *http://homepages.cae.wisc.edu/ callen/*.

[16] D. Mascali. *A new approach to the study of the ECR heating and particle dynamics in the plasma of electron cyclotron resonance ion sources*. PhD thesis, Universit degli studi di Catania-Dipartimento di Fisica ed Astronomia, 2010.

[17] I. Langmuir. *The Collected Works of Irving Langmuir*, volume 5. C. G. Suits, 1961.

[18] T. Fujimoto. *Plasma Spectroscopy*, volume 44 of *Springer Series on Atomic, Optical, and Plasma Physics*. Springer Berlin Heidelberg, 2008.

[19] R. Geller. *Electron Cyclotron Resonance Ion Sources and ECR Plasmas*. PA: Inst. Phys., Philadelphia, 1996.

[20] P. Yeates. *A Spectroscopic and Diagnostics Study of Laser Plasma Generation and Evolution under Multi-variable Target Conditioning*. PhD thesis, National Centre for Plasma Science and Technology-Dublin City University, 2006.

[21] K. D. Kavanagh. *Imaging and Spectroscopy of Laser-Produced Colliding Plasmas*. PhD thesis, National Centre for Plasma Science and Technology-Dublin City University, 2006.

[22] S. Eliezer and H. Hora. Double layers in laser produced plasmas. Physics report (review section of physics letters), Departement of Theoretical Physics, University of New South Wales, Kensington, Australia, 1988.

[23] D. Colombant and G. F. Tonon. X-ray-emission in laser-produced plasmas. *J. Appl. Phys.*, 44(8):3524–3537, 1973.

[24] R. Singh and J. Narayan. Pulsed-laser evaporation technique for deposition of thin films: Physics and theoretical model. *Phys. Rev. B*, 41(13):8843–8859, 1990.

[25] R. Kelly and R.W. Dreyfus. On the effect of knudsen-layer formation on studies of vaporization, sputtering, and desorption. *Surf. Science*, 198:263–276, 1988.

[26] B. Wu and Y. C. Shin. Absorption coefficient of aluminum near the critical point and the consequences on high-power nanosecond laser ablation. *Appl. Phys. Letters*, 89.

[27] R. Kelly. Gas dynamics of the pulsed emission of a perfect gas with applications to laser sputtering and to nozzle expansion. *Phys. Rev. A*, 46(2):860–874, 1992.

[28] L. Torrisi, S. Gammino, L. And, and L. Làska. Tantalum ions produced by 1064 nm pulsed laser irradiation. *J. Appl. Phys.*, 91(7), 2002.

[29] G. Hairapetian and R. L. Stenzel. Observation of a stationary, current-free double layer in a plasma. *Phys. Rev. Lett.*, 65(2):175–178, 1990.

[30] M. A. Raadu. The physics of double layers and their role in astrophysics. *Physics Reports*, 178(2):25–97, 1989.

[31] E. Ahedo and M. Martínez Sánchez. Theory of a stationary current-free double layer in a collisionless plasma. *Phys. Rev. Lett.*, 103(13):135002, 2009.

[32] M. A. Lieberman, C. Charles, and R. W. Boswell. A theory for formation of a low pressure, current-free double layer. *J. of Physics D: Appl. Phys.*, 39(15), 2006.

[33] H. Hora. *Laser Plasma Physics: Forces and the Nonlinearity Principle.* SPIE-International Publisher for Optical Engineering, 2000.

[34] N. M. Bulgakova, A. V. Bulgakov, and F. O. Bobrenok. Double layer effects in laser-ablation plasma plumes. *Phys. Rev. E*, 62(4):5624–5635, 2000.

[35] Ya. B. Zel'dovich and Yu. P. Raizer. *Physics of shock waves and high-temperature hydrodynamics phenomena.* Courier Dover Publications, 2002.

[36] S. Anisimov. Gas dynamics and film profiles in pulsed-laser deposition of materials. *Phys. Rev. B*, 48(16):12076–12081, 1993.

[37] B. Thestrup, B. Toftmann, J. Schou, B. Doggett, and J. G. Lunney. Ion dynamics in laser ablation plumes from selected metals at 355nm. *Appl. Surf. Science*, 197-198:175–180, 2002.

[38] T.N. Hansen, J. Schou, and J.G. Lunney. Langmuir probe study of plasma expansion in pulsed laser ablation. *Appl. Phys. A*, 69:601604, 1999.

[39] P. Hough. *Laser, optical and electrical diagnostics of colliding laser produced plasmas.* PhD thesis, National Centre for Plasma Science and Technology-Dublin City University, 2010.

[40] A.K. Sharma and R.K. Thareja. Plume dynamics of laser-produced aluminum plasma in ambient nitrogen. *App. Surf. Science*, 243, 2005.

[41] D. B. Geohegan. *Pulsed Laser Deposition of Thin Films.* Wiley, New York, 1994.

[42] D. B. Geohegan and A. A. Puretzky. Dynamics of laser ablation plume penetration through low pressure background gases. *Appl. Phys. Lett.*, 67(2), 1995.

[43] S. S. Harilal, C. V. Bindhu, M. S. Tillack, F. Najmabadi, and A. C. Gaeris. Internal structure and expansion dynamics of laser ablation plumes into ambient gases. *J. Appl. Phys.*, 93(5), 2003.

[44] R. F. Wood, K. R. Chen, J. N. Leboeuf, A. A. Puretzky, and D. B. Geohegan. Dynamics of plume propagation and splitting during pulsed-laser ablation. *Phys. Rev. Lett.*, 79(8):1571–1574, 1997.

[45] P. T. Rumsby, J. W. M. Paul, and M. M. Masoud. Interactions between two colliding laser produced plasmas. *Plasma Physics*, 16:969, 1974.

[46] N. C. Woolsey, C. Courtois, and R. O. Dendy. Laboratory plasma astrophysics simulation experiments using lasers. *Plasma Phys. Control. Fusion*, 46(12B):B397, 2004.

[47] C. D. Gregory, J. Howe, B. Loupias, S. Myers, M. M. Notley, Y. Sakawa, A. Oya, R. Kodama, M. Koenig, and N. C. Woolsey. Astrophysical jet experiments with colliding laser-produced plasmas. *The Astrophysical Journal*, 676(1):420, 2008.

[48] A. S. Wan, T. W. Barbee, R. Cauble, P. Celliers, L. B. Da Silva, J. C. Moreno, P. W. Rambo, G. F. Stone, J. E. Trebes, and F. Weber. Electron density measurement of a colliding plasma using soft-x-ray laser interferometry. *Phys. Rev. E*, 55(5):6293–6296, 1997.

[49] V.I. Babushok, Jr. F.C. DeLucia, J.L. Gottfried, C.A. Munson, and A.W. Miziolek. Double pulse laser ablation and plasma: Laser induced

breakdown spectroscopy signal enhancement. *Spectrochimica Acta Part B: Atomic Spectroscopy*, 61(9):999–1014, 2006.

[50] A. Murphy, J. S. Hirsch, D. Kilbane, E. T. Kennedy, M. A. Khater, J-P. Mosnier, A. Neogi, G. OSullivan, C. L. S. Lewis, S. Topping, R. Clarke, E. Divall, P. Foster, C. Hooker, A. Langley, D. Neely, P. Dunne, and J. T. Costello. *Proceedings of the Society of Photo-Optical Instrumentation Engineers (SPIE)*, pages 1196–1203, 2003.

[51] P. Hough, C. McLoughin, T. J. Kelly, P. Hayden, S. S. Harilal, J. P. Mosnier, and J. T. Costello. Time resolved nomarski interferometery of laser produced plasma plumes. *Appl. Surf. Science*, 255:51675171, 2009.

[52] P. W. Rambo and J. Denavit. Interpenetration and ion separation in colliding plasmas. *Physics of Plasmas*, 12(1):4050–4060, 1994.

[53] P. Hough, C. McLoughin, T. J. Kelly, P. Hayden, S. S. Harilal, J. P. Mosnier, and J. T. Costello. Electron and ion stagnation at the collision front between two laser produced plasmas. *J. of Physics D: Appl. Phys.*, 42(5), 2009.

[54] S.L. Ivanovski, A. Bonanno, S. Tudisco, N. Gambino, and D. Mascali. Plasma astrophysics and laser experiments: hydrodynamical simulation of colliding plasmas. *Rad. Eff. and Def. in Solids*, 165(6), 2010.

[55] D. Margarone, L. Torrisi, A. Borrielli, and F. Caridi. Silver plasma by pulsed laser ablation. *Plasma Sources Sci. Technol.*, 17(3), 2008.

[56] E. V. Moskovets. Mass-reflectron as an ion energy analyzer. *Appl. Phys. B*, 54:556–561, 1992.

[57] P. Hayden, A. Cummings, N. Murphy, G. OSullivan, P. Sheridan, J. White, and P. Dunne. 13.5nm extreme ultraviolet emission from tin based laser produced plasma sources. *J. Appl. Phys.*, 99(16), 2006.

[58] K. Oguri, Y. Okano, T. Nishikawa, and H. Nakano. Dynamical study of femtosecond-laser-ablated liquid-aluminum nanoparticles using spatiotemporally resolved x-ray-absorption fine-structure spectroscopy. *Phys. Rev. Lett.*, 99(16), 2007.

[59] L. Torrisi, D. Mascali, R. Miracoli, S. Gammino, N. Gambino, L. Giuffrida, and D. Margarone. Measurements of electron energy distribution in tantalum laser-generated plasma. *J. Appl. Phys.*, 2010(107), 2010.

[60] H. M. Mott and I. Langmuir. The theory of collectors in gaseous discharges. *Phys. Rev.*, 28(4):727–763, 1926.

[61] J. E. Allen. Probe theory - the orbital motion approach. *Physica Scripta*, 45(5), 1992.

[62] I. H. Hutchinson. *Principles of plasma diagnostics*. Cambridge University Press, 2005.

[63] D. Koopman. Langmuir probe and microwave measurements of the properties of streaming plasmas generated by focused laser pulses. *Phys. Fluids*, 14, 1971.

[64] B. Doggett, C. Budtz-Joergensen, J.G. Lunney, P. Sheerin, and M.M. Turner. Behaviour of a planar langmuir probe in a laser ablation plasma. *Appl. Surf. Science*, 247(1-4):134 – 138, 2005. Proceedings of the European Materials Research Society 2004 - Symposium N.

[65] D. Mascali, L. Torrisi, S. Gammino, D. Margarone, F. Maimone, R. Miracoli, and N. Gambino. Langmuir probe characterization of laser generated plasma. *Acta Technica CSAV*, 53, 2008.

[66] H. R. Griem. *Plasma Spectroscopy.* Cambridge University Press, New York, 1997.

[67] U. Fantz. Basic of plasma spectroscopy. *Plasma Source Sci. Technol.*, 15:S137S147, 2006.

[68] http://physics.nist.gov.

[69] H. Sobral, M. Villagran-Muniz, and F. Bredice. Energy balance in laser ablation of metal targets. *J. Appl. Phys.*, 98, 2005.

[70] Y.F. Lu M.H. Hong. Plasma diagnostics at early stage of laser ablation. *Appl. Phys. A.*, 69:S605S608, 1999.

[71] N. Gambino, D. Mascali, S. Tudisco, A. Anzalone, S. Gammino, R. Grasso, R. Miracoli, F. Musumeci, L. Neri, S. Privitera, and A. Spitaleri. Investigation of laser generated plasmas expanding in vacuum and in a background gas by means of time-of-flight measurements. *Proceeding of 37th EPS Conference on Plasma Physics, Dublin, Ireland.*, 2010.

[72] D. Mascali et al. In preparation.

[73] B. Doggett and J.G. Lunney. Langmuir probe characterization of laser ablation plasmas. *J. Appl. Phys.*, 105, 2009. Proceedings of the European Materials Research Society 2004 - Symposium N.

[74] S. Amoruso, B. Toftmann, and J. Schou. Thermalization of a uv laser ablation plume in a background gas: From a directed to a diffusionlike flow. *Phys. Rev. E*, 69, 2004.

[75] J. Siegel, G. Epurescu, A. Perea, F. J. Gordillo-Vzquez, J. Gonzalo, and C. N. Afonso. Temporally and spectrally resolved imaging of laser-induced plasmas. *Optics Letters*, 29:2228–2230, 2004.

[76] J. Dardis. *Interactions of intense optical and extreme-ultraviolet lasers with atoms and solids*. PhD thesis, National Centre for Plasma Science and Technology-Dublin City University, 2009.

[77] M. Hegelich, S. Karsch, G. Pretzler, D. Habs, K. Witte, W. Guenther, M. Allen, A. Blazevic, J. Fuchs, J. C. Gauthier, M. Geissel, P. Audebert, T. Cowan, and M. Roth. Mev ion jets from short-pulse-laser interaction with thin foils. *Phys. Rev. Lett.*, 89(8), 2002.

[78] M. Borghesi, J. Fuchs, S. V. Bulanov, A. J. MacKinnon, P. K. Patel, and M. Roth. Fast ion generation by high-intensity laser irradiation of solid targets and applications. *Fus. Sci. and Tech.*, 49, 2006.

[79] C. Chenais-Popovics, O. Rancu, P. Renaudin, H. Kawagoshi, J. C. Gauthier, M. Dirksmller, I. Uschmann, T. Missalla, E. Frster, O. Renner, E. Krousky, H. Ppin, O. Larroche, and O. Peyrusse. Experimental and numerical analysis of a plasma collision by x-ray spectroscopy and imaging. *Journal of Quantitative Spectroscopy and Radiative Transfer*, 54, 1995.

[80] B. Toftmann, J. Schou, and J.G. Lunney. Dynamics of the plume produced by nanosecond ultraviolet laser ablation of metals. *Phys. Rev. B*, 67, 2003.

[81] S. Anisimov. An analytical model for threedimensional laser plume expansion into vacuum in hydrodynamic regime. *Appl. Surf. Science*, 98, 1996.

[82] Gas-dynamic effects in the laser-pulse sputtering of aln: is there evidence for phase explosion? *Appl. Surf. Science*, 133(4).

[83] S. Anisimov and B. S. Luy'yanchuk. Selected problems of laser ablation theory. *Phys. Uspekhi*, 45:293–324, 2002.

[84] E. Salpeter. Electrons screening and thermonuclear reactions. *Aust. J. Phys.*, 7, 1954.